

## ABSTRACT

PAPA, CHRISTOPHER MICHAEL. Excited State Dynamics at Interfaces between Lead Sulfide or Lead Halide Nanomaterials and Organic Molecules (Under the direction of Prof. Felix N. Castellano).

The recent discovery that semiconductor nanomaterials can sensitize triplet states in surface-appended molecular chromophores has implications in diverse fields spanning nonlinear optics, solar energy conversion, and medicine. However, numerous fundamental questions linger in understanding how charge carriers and entire electronic excited states migrate across interfaces between the semiconductor nanomaterials and the molecular chromophores. The first research project in this dissertation focused on the transient absorption spectroscopy of PbS nanocrystals (NCs) with size-controlled band-edge exciton energies ranging from 1.15 to 1.54 eV as the semiconductor nanomaterial. Following post-synthetic modification with a carboxylic acid-functionalized derivative of 6,13-bis(triisopropylsilylethynyl)-pentacene (TPn), selective excitation of the PbS NCs at 743 nm leads to a step-wise triplet sensitization mechanism, which is conserved across all NC sizes. The rate constant for the delayed formation of the TPn triplet excited state was found to increase with increasing PbS conduction band energy, in accordance with Marcus theory. This study delivered evidence of an indirect triplet sensitization process, which inconsistent with a concerted Dexter-like energy transfer process.

To better elucidate the role of surface-trapped carriers in the indirect triplet sensitization process, the second research project in this dissertation utilized PbS-CdS core-shell NCs derived from the multiple sizes of PbS NC *via* cation exchange. By combining 1.54 eV PbS cores with various CdS shell thicknesses and surface-appended TPn molecules, insights were gained into the impact of shells on TPn triplet generation. It

was determined that indirect triplet sensitization of TPn by surface-trapped states on PbS NCs, while viable, is less efficient than tunneling through CdS from a PbS-CdS NC with a passivated PbS surface.

Continuing with the theme of energy transfer across the interface between semiconductor nanomaterials and molecular chromophores, lead halide perovskite nanoplatelets were paired with a functionalized derivative of 4-(1-piperidinyl)naphthalene-1,8-dicarboximide (PNI). Successful synthesis of the PNI surfactant and unexpectedly high tolerance of PNI association by the nanoplatelet surfaces provided a test bed for solution-phase photophysical investigation. Time-resolved photoluminescence data from the obtained nanomaterial-surfactant assemblies provided the strongest evidence to date of dipolar Förster resonance energy transfer (FRET) from colloidal perovskite nanoplatelets to molecular chromophores.

© Copyright 2020 by Christopher Papa

All Rights Reserved

Excited State Dynamics at Interfaces between Lead Sulfide or Lead Halide  
Nanomaterials and Organic Molecules.

by  
Christopher Michael Papa

A dissertation submitted to the Graduate Faculty of  
North Carolina State University  
in partial fulfillment of the  
requirements for the degree of  
Doctor of Philosophy

Chemistry

Raleigh, North Carolina  
2020

APPROVED BY:

---

Felix N. Castellano  
Committee Chair

---

Jerry L. Whitten

---

David A. Shultz

---

James D. Martin

## **DEDICATION**

*To Kyla.*

## BIOGRAPHY

Christopher M. Papa was born to Alyce J. Papa and William C. Papa in Cincinnati, Ohio on March 28<sup>th</sup>, 1988. He is the proud older brother of Anthony J. Papa. He grew up in Wyoming, Ohio and attended Wyoming High School, where he first discovered his love for Chemistry. After attending the Georgia Institute of Technology in Atlanta, Georgia, he transferred to the University of Cincinnati, where he met his wife, Kyla M. Vonderhaar. He earned a Bachelor of Science in Chemistry from the University of Cincinnati in 2012, also obtaining a Certificate in Italian Language and Culture. During his time there, he joined the research group of the late Professor William B. Connick, synthesizing a library of platinum(II) complexes with pincer ligands and studying their photophysical and electrochemical properties. Matriculating to the Department of Chemistry at the University of Wisconsin, Madison, he performed electrodeposition and electrochemical characterization of binary and ternary niobium- and tantalum-containing oxide thin films under the direction of Professor Kyoung-Shin Choi. When Kyla was relocated to High Point, North Carolina, Christopher completed his Master of Science in Chemistry in December 2014 and joined the Department of Chemistry at North Carolina State University in August 2015. It was there that he undertook research with the guidance of Professor Felix N. Castellano, who granted him the freedom to explore the nuances of semiconductor nanomaterial photophysics with time-resolved spectroscopic methods.

## ACKNOWLEDGMENTS

I would like to start by thanking Phil. As an older graduate student who had valued – at least to some extent – my marriage more than my academic career, I was worried I came across as damaged goods in the eyes of potential advisors. Whether that was true or not, you certainly never treated me that way and were always understanding of my hour-long commute to campus. More importantly, you facilitated my growth as a scientist not by micro managing or even holding my hand, but instead by giving me freedom to make mistakes and learn. You supplemented that development by trusting my existing knowledge and willingness to stay abreast of the literature while providing timely guidance on the photophysics that were more unfamiliar to me. I've appreciated working in the group environment that you've fostered over the years, and I take slight pride in often being the only grad student who gets your 80's pop culture references. I am eternally grateful that I got to work with you.

I would like to thank my Committee Members. Since I had mostly succeeded in traditional Inorganic Chemistry, Professor Jerry Whitten was the first person to make me feel like I was actually good at Physical Chemistry. Professor Dave Shultz had his students helping me with some EPR experiments my first summer in the Department, and fielded more than a few off-the-wall questions from me (and sometimes Phil, too!) over the years. Professor Jim Martin was stimulating to talk to and very generous with his time in my first Fall Semester, so I was quite excited when he volunteered to complete my committee at my preliminary exam. I would also like to thank my GSR Professor Brendan O'Connor for serving at both my preliminary exam and my final defense. I must also thank the rest of the Chemistry Department faculty at NC State, particularly those in

both the Inorganic and Physical Divisions, who have been invaluable in my time as a student.

I would like to thank all the Castellano Group members, past and present, for their mentorship, technical advice, friendship, and more. I would especially like to thank Dr. Cédric Mongin for successfully teaching me how to make useful semiconductor nanocrystals on my very first day in the lab and Dr. Sofia Garakyaraghi for teaching me the finer points of ultrafast spectroscopy. I also particularly need to thank Daniel Yonemoto for providing a sounding board, co-founding the “Nano Empire”, and being a great roommate and “partner-in-crime” at GRC and ACS meetings. I want to thank everyone who was involved in the creation or maintenance of Thursday Beers or Music Mondays. I think I can list all of you from memory, but the thought of leaving off anybody is giving me crippling anxiety and I have to get this thing out to my committee eventually. If you think these thanks are directed at you, they are.

I would like to thank my family. I thank Dr. Corey Misenheimer for letting me kill time in his office when I first arrived on campus at NCSU. I thank my grandparents Alba and Bill for having Kyla and me up to the lake any time. I also thank Bill for being the original researcher in the family, and Alba for always reminding me that she’s a chemist, too, unlike all of these engineers. I have to thank my brother Anthony for always humoring my dream of a Papa brothers science podcast and for understanding when I can’t come skiing because I need this 77 K phosphorescence data *this weekend*. Lastly, I’d like to thank my parents for their unending support for the last 32+ years. There were certainly times where it did not look like this was going to ever happen. And with different parents, it is quite possible that it would not have. Additionally, I have to give

my parents a second shout-out because they are the only people I can guarantee will read this section (Hi, Mom!).

Finally, I would like to thank my wife Kyla. More than anyone else in the world, you've been traveling this road alongside me. I am sure a lot of my complaints about my work were bizarre or just extremely abstract. I know it was frustrating to know a text from me saying "I'm about to leave" meant "I'll be home in 1-2 hours, depending how distracted I get." I am indescribably grateful for the nights you spent letting me endlessly practice presentations with a mouse-shaped laser pointer. Your support of me has been the single most crucial ingredient to any success that I've achieved in the last decade. I look forward to our next great adventure!

## TABLE OF CONTENTS

LIST OF TABLES.....	ix
LIST OF FIGURES AND SCHEMES.....	x
CHAPTER 1: Selected Fundamentals of the Photophysics and Spectroscopy of Semiconductor Nanomaterials.....	1
1.1 Photophysical Processes.....	1
1.1.1 Light Absorption.....	1
1.1.2 Light Emission (Photoluminescence).....	2
1.1.3 Non-Radiative Processes.....	5
1.1.4 Photoinduced Electron Transfer.....	7
1.1.5 Direct Energy Transfer Mechanisms.....	9
1.2 Photophysical Processes in Semiconductor Nanomaterials.....	10
1.2.1 Semiconductor Nanomaterials.....	10
1.2.2 Photosensitization from Semiconductor Nanomaterials.....	12
1.3 Spectroscopic Instrumentation and Techniques.....	14
1.3.1 Electronic Absorption Spectroscopy (UV-vis).....	14
1.3.2 Steady-State Photoluminescence Spectroscopy.....	16
1.3.3 Time-Resolved Photoluminescence Spectroscopy.....	18
1.3.4 Transient Absorption Spectroscopy.....	20
1.4 References.....	25
CHAPTER 2: TIPS-Pentacene Triplet Exciton Generation on PbS Quantum Dots Results from Indirect Sensitization.....	28
2.1 Abstract.....	28
2.2 Introduction.....	28
2.3 Experimental.....	30
2.3.1 Nanomaterial synthesis and characterization.....	30
2.3.2 Time-resolved spectroscopic methods.....	33
2.4 Results and Discussion.....	35
2.5 Conclusions.....	43
2.6 Acknowledgments.....	44
2.7 References.....	45
2.8 Supplementary Information.....	49
CHAPTER 3: CdS Shells Inhibit Surface-Trap Involvement in Triplet Energy Transfer Mechanisms from PbS Nanocrystals.....	67
3.1 Abstract.....	67
3.2 Introduction.....	67
3.3 Results and Discussion.....	70
3.3.1 Optical Properties of PbS-CdS Core-Shell NCs.....	70
3.3.2 TPn Triplet Sensitization by PbS-CdS NCs.....	73
3.3.3 Attenuation of the Transient Dipole-Induced Absorption Shift.....	75
3.3.4 Rate Constants for TPn Triplet Formation.....	76
3.3.5 Efficiencies of TPn Triplet Sensitization.....	78
3.4 Conclusions.....	80
3.5 Experimental Methods.....	80

3.5.1 Quantum Dot Syntheses .....	80
3.5.2 Ligand Exchange with TPn .....	80
3.5.3 Static Spectroscopy.....	81
3.5.4 Electron Microscopy.....	81
3.5.5 Ultrafast Transient Absorption Spectroscopy.....	82
3.5.6 Nanosecond Transient Absorption Spectroscopy.....	82
3.5.7 Extracting Time Constants from Transient Absorption Difference Spectra .....	83
3.6 Acknowledgments .....	84
3.7 References .....	85
3.8 Supporting Information .....	90
<b>CHAPTER 4: Förster Resonance Energy Transfer from Colloidal Perovskite Nanoplatelets .....</b>	
4.1 Abstract .....	101
4.2 Introduction .....	101
4.3 Experimental Section .....	103
4.3.1 Abbreviations & Materials .....	103
4.3.2 Synthetic Methods .....	104
4.3.3 Characterization and Spectroscopy .....	108
4.4 Results and Discussion.....	110
4.4.1 Synthesis and Characterization of Colloidal Perovskite Nanoplatelets .....	110
4.4.2 Synthesis of PNI Surfactants .....	113
4.4.3 Self-Assembly of Colloidal Perovskite Nanoplatelets with PNI Surfactants .....	115
4.4.4 Photoluminescence Quenching by PNI Surfactants .....	119
4.5 Conclusions .....	123
4.6 Acknowledgments .....	123
4.7 References .....	124
4.8 Supporting Information .....	126
4.8.1 Details on Fitting Nanoplatelet Photoluminescence Decays.....	126
4.8.2 Supplemental Figures .....	128

## LIST OF TABLES

<b>Table S2.1</b> Decay constants obtained from fitting kinetic traces at single wavelengths of TA data for PbS-TPn nanocrystal-molecule hybrid materials suspended in toluene following pulsed excitation at 743 nm (0.15 $\mu$ J/pulse, 100 fs fwhm).....	55
<b>Table S2.2</b> Decay constants obtained from fitting kinetic traces ( $\lambda_{\text{probe}} = 534$ nm) displayed in Fig. S2.10 to biexponential functions. Data is from TA kinetics of PbS-TPn nanocrystal-molecule hybrid materials suspended in toluene following pulsed excitation at 743 nm (1.0 mJ/pulse, 5 ns fwhm).....	57
<b>Table S2.3</b> Raw time constants and per-TPn-adjusted rate constants obtained by modeling ultrafast TA spectra for PbS-TPn materials. Corresponding basis spectra are displayed in Figure 2.3. For accurate lifetimes for the relaxation of $^3\text{TPn}$ , see Table S2.2. ....	58
<b>Table 3.1</b> Raw time constants and per-TPn-adjusted rate constants obtained by modeling ultrafast TA spectra for PbS-CdS-TPn and PbS-805-TPn materials. Corresponding basis spectra are displayed in Figures 3.5a-d. The third time constant is “infinite” over the 6.2 ns delay stage of the ultrafast TA experiment. For accurate lifetimes for the relaxation of $^3\text{TPn}$ , see Table S3.1.....	78
<b>Table S3.1</b> Decay constants obtained from fitting monoexponential functions to TA kinetics of PbS-CdS-TPn core-shell nanocrystal-molecule hybrid materials suspended in toluene following pulsed excitation at 744 nm (1.0 mJ/pulse, 5 ns fwhm). Kinetic traces ( $\lambda_{\text{probe}} = 534$ nm) are displayed in Fig. S3.6.....	95
<b>Table 4.1</b> TCSPC Fitting Parameters and Energy Transfer Rate Constants.....	121

## LIST OF FIGURES AND SCHEMES

<b>Figure 1.1</b> A qualitative potential energy diagram showing the effects of (a) minimal and (b) large excited state distortion (Q) on the shape, structure, and broadness of emission bands (insets).....	4
<b>Figure 1.2</b> Generalized Jablonski diagram featuring example photophysical processes. Non-radiative transitions are dashed while radiative transitions are solid. ....	5
<b>Figure 1.3</b> Schematic illustration of photoinduced electron transfer processes, showing (a) oxidative quenching and (b) reductive quenching of the photoexcited species.....	8
<b>Figure 1.4</b> Schematic illustration of direct energy transfer processes, showing (a) Dexter energy transfer and (b) FRET. ....	10
<b>Figure 1.5</b> Illustration of (a) electronic energy states of a semiconductor in the transition from discrete molecules to nano-sized crystals and bulk crystals. Blue shading denotes ground state electron occupation. Experimental (b) electronic absorption (solid) and photoluminescence (dashed) spectra of PbS semiconductor nanocrystals showing quantum confinement and size tunability. Figure 1.5a was adapted from ref. 19. <sup>19</sup> .....	12
<b>Figure 1.6</b> Composition-based wavelength ranges of absorption (closed) and emission (open) for reported near-infrared-emitting nanomaterials prepared by solution-based methodologies. ....	13
<b>Figure 1.7</b> Schematic diagram of a spectrofluorometer based on a continuous Xe light source, two Czerny-Turner monochromators, and a detector for sample emission. ....	17
<b>Figure 1.8</b> The principle of TCSPC is illustrated by (top) the laser (green) and photoluminescence (red) waveforms, the detection of individual photons (middle) adding counts to time bins, and the constructed histogram (bottom) after many laser pulses. Figure was adapted from ref. 13. <sup>13</sup> .....	19
<b>Figure 1.9</b> Simplified schematic diagram of a nanosecond transient absorption spectrometer.....	21
<b>Figure 1.10</b> Simplified schematic diagram of an ultrafast transient absorption spectrometer.....	22
<b>Figure 2.1</b> (a) Illustration of PbS nanocrystal first exciton and TPn-centered energy levels. (b) Electronic absorption (solid lines) and emission spectra (dashed lines) for PbS NCs ranging in diameter from $3.3 \pm 0.6$ nm (top, red) to $2.2 \pm 0.3$ nm (bottom, violet). (c) Electronic absorption spectra (top) in toluene of PbS-1075 nanocrystals before and after ligand exchange by TPn with free TPn shown, and photoluminescence spectra in toluene (bottom) of PbS-1075 and PbS-1075-TPn. The depression in the photoluminescence near 1150 nm results from toluene absorption. ....	36
<b>Figure 2.2</b> Ultrafast TA difference spectra of PbS-805 (a) and PbS-805-TPn (b) suspensions in toluene following 743 nm pulsed laser excitation (0.15	

<p><math>\mu\text{J}/\text{pulse}</math>, 100 fs fwhm). Time delays range from 1.0 ps (red) to 6.0 ns (blue). Ultrafast TA kinetics (c) probed at 534 nm (closed circles) and different PbS first exciton bleach wavelengths (open circles) for PbS-805-TPn (purple), PbS-970-TPn (blue), PbS-1000-TPn (green), and PbS-1075-TPn (red) suspensions in toluene following 743 nm pulsed laser excitation (0.15 <math>\mu\text{J}/\text{pulse}</math>, 100 fs fwhm).</p>	38
<p><b>Figure 2.3</b> Basis spectra modeled on TA spectra of (a) PbS-1075-TPn, (b) PbS-1000-TPn, (c) PbS-970-TPn, and (d) PbS-805-TPn materials. The ultrafast TA spectra initially resemble the 1st (darkest hues) spectra and eventually come to resemble the 3rd spectra (palest hues) by the end of the 6.2 ns delay stage. The 2nd spectra (intermediate hues) are necessary to accurately model the experimental data. Data from 425 to 775 nm and data from 825 to 1325 nm were fit with matching rate constants. Logarithm of extracted rate constants plotted as a function of thermodynamic driving force (e) and approximate PbS NC diameter (e, inset). Bars in (e) and (e, inset) reflect the standard error calculated from three independent measurements. The solid red line in (e) is a Marcus theory fit to the data intended as a phenomenological guide for the eye.</p>	41
<p><b>Figure S2.1</b> TEM images of PbS NCs with average diameters of (a) <math>3.3 \pm 0.6</math> nm, (b) <math>3.0 \pm 0.5</math> nm, (c) <math>2.9 \pm 0.5</math> nm, and (d) <math>2.2 \pm 0.3</math> nm.</p>	49
<p><b>Figure S2.2</b> Electronic absorption spectra of PbS-1000 (red), PbS-970 (green), PbS-805 (purple) with their corresponding PbS-TPn hybrid materials (black lines, matching y-axis offset indicates matching NC size).</p>	49
<p><b>Figure S2.3</b> TEM images of (a) PbS-1075-TPn, (b) PbS-1000-TPn, (c) PbS-970-TPn, (d) PbS-805-TPn.</p>	50
<p><b>Figure S2.4</b> Ultrafast TA difference spectra of a solution of TPn in toluene following 743 nm pulsed laser excitation (0.80 <math>\mu\text{J}/\text{pulse}</math>, 100 fs fwhm). The non-time-resolved spectral feature centered around 743 nm is scattered excitation.</p>	50
<p><b>Figure S2.5</b> Ultrafast TA difference spectra of PbS nanocrystal suspensions in toluene following 743 nm pulsed laser excitation (0.15 <math>\mu\text{J}/\text{pulse}</math>, 100 fs fwhm). The spectra correspond to PbS-805 in the (a) visible and (b) near-IR spectral regions, PbS-970 in the (c) visible and (d) NIR, PbS-1000 in the (e) visible and (f) NIR, and PbS-1075 in the (g) visible and (h) NIR. Time delays range from 1.0 ps (red) to 6.0 ns (blue).</p>	51
<p><b>Figure S2.6</b> Comparison of normalized, ultrafast (0.15 <math>\mu\text{J}/\text{pulse}</math>, 100 fs fwhm, 743 nm) TA difference spectra (colored) and normalized, nanosecond (1.0 mJ/pulse, 5 ns fwhm, 743 nm) TA difference spectra (black) of PbS nanocrystal suspensions in toluene following pulsed laser excitation. The spectra correspond to (a) PbS-805, (b) PbS-970, (c) PbS-1000, and (d) PbS-1075. Time delays are prompt for the nanosecond TA spectra and 6.2 ns for the ultrafast TA spectra.</p>	52

<b>Figure S2.7</b> Nanosecond TA kinetics of (a) PbS-805, (b) PbS-970, (c) PbS-1000, and (d) PbS-1075 in toluene following pulsed excitation at 743 nm (1.0 mJ/pulse, 5 ns fwhm). The decays of the PbS NC induced absorption observed at 550 nm and the X1 bleaches at 710, 890, 920 and 1010 nm can be fit by biexponential functions (black lines) with time constants of $0.22 \pm 0.07$ and $1.8 \pm 0.2$ $\mu$ s.....	53
<b>Figure S2.8</b> Ultrafast TA difference spectra of PbS-TPn nanocrystal-molecule hybrid materials suspended in toluene following 743 nm pulsed laser excitation (0.15 $\mu$ J/pulse, 100 fs fwhm). The spectra correspond to PbS-805-TPn in the (a) visible and (b) near-IR spectral regions, PbS-970-TPn in the (c) visible and (d) NIR, PbS-1000-TPn in the (e) visible and (f) NIR, and PbS-1075-TPn in the (g) visible and (h) NIR. Time delays range from 1.0 ps (red) to 6.0 ns (blue). .....	54
<b>Figure S2.9</b> Comparison of normalized, ultrafast (0.15 $\mu$ J/pulse, 100 fs fwhm, 743 nm) TA difference spectra (colored) and normalized, nanosecond (1.0 mJ/pulse, 5 ns fwhm, 743 nm) TA difference spectra (black) of PbS-TPn hybrid material suspensions in toluene following pulsed laser excitation. The spectra correspond to (a) PbS-805-TPn, (b) PbS-970-TPn, (c) PbS-1000-TPn, and (d) PbS-1075-TPn. Time delays are 6.2 ns for the ultrafast TA spectra and 100 ns for the nanosecond TA spectra. ....	56
<b>Figure S2.10</b> Nanosecond TA kinetics of PbS-TPn nanocrystal-molecule hybrid materials suspended in toluene following pulsed excitation at 743 nm (1.0 mJ/pulse, 5 ns fwhm). The decays of the <sup>3</sup> TPn feature observed at 534 nm are fit by biexponential functions (black lines) with time constants given in Table S2.2. PbS-970-TPn TA kinetics omitted for clarity. ....	57
<b>Figure S2.11</b> Rate constants from temperature-dependent nanosecond TA kinetics of PbS-TPn nanocrystal-molecule hybrid materials suspended in toluene following pulsed excitation at 743 nm (1.0 mJ/pulse, 5 ns fwhm). The logarithm of the rate constants determined by mathematical fitting of the <sup>3</sup> TPn decay observed at 534 nm is compared to the inverse of the temperature at which the decay was recorded. ....	58
<b>Figure S2.12</b> Experimental PbS-1075-TPn ultrafast TA spectra (black) probed in the visible region of the electromagnetic spectrum compared to the fit modeled by linear decomposition (red). Three DADS were necessary to reproduce the changes in the spectra. Time constants for first-order interconversion between the DADS were found to be 12.3 ps and 5 ns as described in Table S2.3. ....	59
<b>Figure S2.13</b> Experimental PbS-1075-TPn ultrafast TA spectra (black) probed in the near-infrared region of the electromagnetic spectrum compared to the fit modeled by linear decomposition (red). Three DADS were necessary to reproduce the changes in the spectra. Time constants for first-order interconversion between the DADS were found to be 12.3 ps and 5 ns as described in Table S2.3. ....	60

<b>Figure S2.14</b> Experimental PbS-1000-TPn ultrafast TA spectra (black) probed in the visible region of the electromagnetic spectrum compared to the fit modeled by linear decomposition (red). Three DADS were necessary to reproduce the changes in the spectra. Time constants for first-order interconversion between the DADS were found to be 6.8 ps and 1.1 ns as described in Table S2.3.....	61
<b>Figure S2.15</b> Experimental PbS-1000-TPn ultrafast TA spectra (black) probed in the near-infrared region of the electromagnetic spectrum compared to the fit modeled by linear decomposition (red). Three DADS were necessary to reproduce the changes in the spectra. Time constants for first-order interconversion between the DADS were found to be 6.8 ps and 1.1 ns as described in Table S2.3. ....	62
<b>Figure S2.16</b> Experimental PbS-970-TPn ultrafast TA spectra (black) probed in the visible region of the electromagnetic spectrum compared to the fit modeled by linear decomposition (red). Three DADS were necessary to reproduce the changes in the spectra. Time constants for first-order interconversion between the DADS were found to be 4.0 ps and 1.8 ns as described in Table S2.3. ....	63
<b>Figure S2.17</b> Experimental PbS-970-TPn ultrafast TA spectra (black) probed in the near-infrared region of the electromagnetic spectrum compared to the fit modeled by linear decomposition (red). Three DADS were necessary to reproduce the changes in the spectra. Time constants for first-order interconversion between the DADS were found to be 4.0 ps and 1.8 ns as described in Table S2.3. ....	64
<b>Figure S2.18</b> Experimental PbS-805-TPn ultrafast TA spectra (black) probed in the visible region of the electromagnetic spectrum compared to the fit modeled by linear decomposition (red). Three DADS were necessary to reproduce the changes in the spectra. Time constants for first-order interconversion between the DADS were found to be 3 ps and 0.39 ns as described in Table S2.3. This sample was absorbance matched at excitation to the PbS-TPn materials.....	65
<b>Figure S2.19</b> Atomically precise space-filling models of rock salt PbS cuboctahedra possessing vertex-to-vertex distances of 2.17, 2.55, 3.00, and 3.40 nm. ....	66
<b>Figure 3.1</b> (a) Schematic illustration of PbS core first exciton and TPn-centered energy levels separated by CdS shells of varying thickness. (b) Electronic absorption (solid lines) and emission spectra (dashed lines) for PbS NCs ranging in diameter from $3.0 \pm 0.5$ nm (top, orange) to $2.2 \pm 0.3$ nm (bottom, violet). (c) Electronic absorption (solid lines) and emission spectra (dashed lines) for PbS-CdS NCs following cation exchange. Colors are matched to the parent PbS NCs in (b), and 2.2 nm PbS NCs (bottom, violet) were not subjected to cation exchange. ....	69
<b>Figure 3.2</b> Ultrafast TA difference spectra of (a) PbS-805, (b) PbS-945-CdS, (c) PbS-970-CdS, and (d) PbS-1000-CdS nanocrystal suspensions in toluene	

following 744 nm pulsed laser excitation (0.15 $\mu\text{J}/\text{pulse}$ , 100 fs fwhm). Time delays range from 1.0 ps (red) to 6.0 ns (blue). .....	72
<b>Figure 3.3</b> Ultrafast TA difference spectra of (a) PbS-805-TPn, (b) PbS-945-CdS-TPn, (c) PbS-970-CdS-TPn, and (d) PbS-1000-CdS-TPn nanocrystal suspensions in toluene following 744 nm pulsed laser excitation (0.15 $\mu\text{J}/\text{pulse}$ , 100 fs fwhm). Time delays range from 1.0 ps (red) to 6.0 ns (blue).....	73
<b>Figure 3.4</b> Ultrafast TA kinetics monitoring the (a) $^3\text{TPn}$ signal probed at 534 nm and (b) PbS first exciton bleach signal probed at 740 nm for PbS-805-TPn (purple), PbS-945-CdS-TPn (blue), PbS-970-CdS-TPn (green), and PbS-1000-CdS-TPn (orange) suspensions in toluene following 744 nm pulsed laser excitation (0.15 $\mu\text{J}/\text{pulse}$ , 100 fs fwhm). .....	74
<b>Figure 3.5</b> Basis spectra modelled on TA spectra of (a) PbS-805-TPn, (b) PbS-945-CdS-TPn, (c) PbS-970-CdS-TPn, (d) PbS-1000-CdS-TPn materials, and (e) Graphical comparison of relative QY for TTET in PbS-CdS-TPn materials with relative PLQY for the PbS-CdS QD with the same CdS shell thickness. Dashed line included in (e) to show trend for perfect proportional relationship. ....	76
<b>Figure S3.1</b> TEM images of PbS parent NCs with average diameters of (a) $3.0 \pm 0.5$ nm, (b) $2.9 \pm 0.5$ nm, (c) $2.6 \pm 0.4$ nm, and PbS-CdS core-shell NCs with average diameters of (d) $3.0 \pm 0.5$ nm, (e) $2.9 \pm 0.5$ nm, and (f) $2.6 \pm 0.4$ nm. ....	90
<b>Figure S3.2</b> Comparison of normalized, ultrafast (0.15 $\mu\text{J}/\text{pulse}$ , 100 fs fwhm, 744 nm) TA difference spectra (colored) and normalized, nanosecond (1.0 mJ/pulse, 5 ns fwhm, 744 nm) TA difference spectra (black) of PbS-CdS core-shell nanocrystal suspensions in toluene following pulsed laser excitation. The spectra correspond to (a) PbS-805, (b) PbS-945-CdS, (c) PbS-970-CdS, and (d) PbS-1000-CdS. Time delays are prompt for the nanosecond TA spectra and 6.2 ns for the ultrafast TA spectra. ....	91
<b>Figure S3.3</b> Nanosecond TA kinetics of (a) PbS-805, (b) PbS-945-CdS, (c) PbS-970-CdS, and (d) PbS-1000-CdS in toluene following pulsed excitation at 744 nm (1.0 mJ/pulse, 5 ns fwhm). The decays of the PbS first exciton bleach monitored at 720 nm for each species can be fit by exponential functions (black lines) with a time constant of $2.42 \pm 0.07 \mu\text{s}$ .....	92
<b>Figure S3.4</b> Electronic absorption spectra of PbS-1000-CdS (orange, top), PbS-970-CdS (green), PbS-945-CdS (blue), PbS-805 (violet, bottom), and their corresponding PbS-CdS-TPn hybrid materials (black lines, matching y-axis offset indicates matching NC size). ....	93
<b>Figure S3.5</b> Comparison of normalized, ultrafast (0.15 $\mu\text{J}/\text{pulse}$ , 100 fs fwhm) TA difference spectra (colored) and normalized, nanosecond (1.0 mJ/pulse, 5 ns fwhm) TA difference spectra (black) of PbS-CdS-TPn core-shell hybrid material suspensions in toluene following 744 nm pulsed laser excitation. The spectra correspond to (a) PbS-805-TPn, (b) PbS-945-CdS-TPn, (c)	

PbS-970-CdS-TPn, and <b>(d)</b> PbS-1000-CdS-TPn. Time delays are 6.2 ns for the ultrafast TA spectra and 100 ns for the nanosecond TA spectra. ....	94
<b>Figure S3.6</b> Nanosecond TA kinetics of PbS-CdS-TPn core-shell and PbS-805-TPn nanocrystal-molecule hybrid materials suspended in toluene following pulsed excitation at 744 nm (1.0 mJ/pulse, 5 ns fwhm). The decays of the <sup>3</sup> TPn feature observed at 534 nm are fit by monoexponential functions (black lines) with time constants given in Table S3.1. ....	95
<b>Figure S3.7</b> Logarithm of extracted rate constants for <b>(a)</b> hole trapping in the PbS cores, $k_1$ , and <b>(b)</b> the formation of <sup>3</sup> TPn, $k_2$ , plotted as a function of CdS shell thickness. As noted in the text, $k_2$ values were normalized by the number of TPn molecules on the surface. Error bars represent the standard error calculated from three independent measurements. ....	96
<b>Figure S3.8</b> Absorbance-matched emission spectra for <b>(a)</b> PbS-CdS NCs and <b>(b)</b> PbS-CdS-TPn materials suspended in toluene after 744 nm excitation. Quenching efficiencies range from 98% for PbS-1000-CdS-TPn (orange traces) to >99% for PbS-805-TPn (purple traces). ....	96
<b>Figure S3.9</b> Experimental PbS-805-TPn ultrafast TA spectra (black) probed in the visible region of the electromagnetic spectrum compared to the fit modeled by linear decomposition (red). Three DADS were necessary to reproduce the changes in the spectra. Time constants for first-order interconversion between the DADS were found to be 4.0 ps and 0.36 ns as described in the main text. This sample was absorbance matched at excitation to the PbS-CdS-TPn materials. ....	97
<b>Figure S3.10</b> Experimental PbS-945-CdS-TPn ultrafast TA spectra (black) probed in the visible region of the electromagnetic spectrum compared to the fit modeled by linear decomposition (red). Three DADS were necessary to reproduce the changes in the spectra. Time constants for first-order interconversion between the DADS were found to be 17 ps and 3.1 ns as described in the main text. ....	98
<b>Figure S3.11</b> Experimental PbS-970-CdS-TPn ultrafast TA spectra (black) probed in the visible region of the electromagnetic spectrum compared to the fit modeled by linear decomposition (red). Three DADS were necessary to reproduce the changes in the spectra. Time constants for first-order interconversion between the DADS were found to be 48 ps and 2.2 ns as described in the main text. ....	99
<b>Figure S3.12</b> Experimental PbS-1000-CdS-TPn ultrafast TA spectra (black) probed in the visible region of the electromagnetic spectrum compared to the fit modeled by linear decomposition (red). Three DADS were necessary to reproduce the changes in the spectra. Time constants for first-order interconversion between the DADS were found to be 44 ps and 2.5 ns as described in the main text. ....	100

<b>Figure 4.1</b> Ground state electronic absorption spectra for $L_2PbBr_4$ perovskite nanoplatelets synthesized with six different types of surfactant (a) immediately after synthesis and (b) after 24 h in solution. ....	111
<b>Figure 4.2</b> The absorbance (solid) and steady state emission (dashed) spectra of (OA)(BA) $PbBr_4$ nanoplatelets in toluene. Emission spectrum was recorded at 298 K using 320 nm excitation. ....	113
<b>Scheme 4.1</b> Synthetic scheme for PNIHBr. ....	113
<b>Figure 4.3</b> The absorbance (solid) and fluorescence (dashed) spectra of (red) PNInBoc in toluene overlaid on the (OA)(BA) $PbBr_4$ nanoplatelet spectra from Figure 4.2 (black). PNInBoc emission spectrum was recorded at 298 K using 405 nm excitation. ....	115
<b>Figure 4.4</b> Electronic absorption spectra of $L_2PbBr_4$ nanoplatelets with (multi-color, see legend) and without (black) various PNI surfactant loadings, PNInBoc (red), and free PNIHBr (orange) in toluene. The 175% PNI loading corresponds to an excess of the PNI surfactant precursor in the nanoplatelet synthesis (see text). ....	116
<b>Figure 4.5</b> Electronic absorption (solid) and emission (dashed) spectra of (OA)(BA) $PbBr_4$ nanoplatelets (black) as well as nanoplatelet species with 10% (purple), 30% (dark blue), and 50% (light blue) of their OA and BA surfactants replaced by PNI surfactants. Emission spectra were recorded at 298 K using 320 nm excitation. ....	119
<b>Figure 4.6</b> TCSPC PL intensity decays of (OA)(BA) $PbBr_4$ nanoplatelets without (red) and with various PNI surfactant loadings (many colors, see legend) illustrating dynamic quenching likely from FRET. Decays were recorded at 420 nm with a 1 nm slit width and were excited at 400 nm with a 4 MHz repetition rate. ....	120
<b>Figure S4.1</b> TEM images of (OA)(BA) $PbBr_4$ nanoplatelets and (b, inset) FFT of the lattice planes imaged in (b). ....	128
<b>Figure S4.2</b> XRD pattern for (OA)(BA) $PbBr_4$ nanoplatelets where the precise surfactant composition, OA, BA, or a mixture of both, results in changes to the nanoplatelet superlattice stacking distance. ....	128
<b>Figure S4.3</b> TCSPC fluorescence intensity decays of (a) PNInBoc and (b) PNIHBr in toluene. The red traces are monoexponential decay curves fit to the TCSPC data with the residuals displayed above. Samples were excited by a 405 nm diode laser (56.5 ps fwhm) set to a 100 kHz repetition rate. A band-pass filter centered at 500 nm with a 45 nm width was used to select the emission. ....	129
<b>Figure S4.4</b> TEM images of (PNI) $PbBr_4$ nanoplatelets. ....	129
<b>Figure S4.5</b> XRD pattern for (PNI) $PbBr_4$ nanoplatelets where only the reflections due to the Si substrate at $2\theta = 32.95^\circ$ and $33.03^\circ$ and an unassigned reflection at $11.50^\circ$ are visible. The reflection at $2\theta = 11.50^\circ$ also appears for (OA)(BA) $PbBr_4$ nanoplatelets (Figure S4.2). ....	130

<b>Figure S4.6</b> The electronic absorption spectrum (pink) of lead bromide perovskite nanoplatelets synthesized with a 75% excess of the PNIHBr ligand salt precursor compared to a linear combination (gray) of the absorption spectrum of 100% PNI-ligated nanoplatelets and 0.75 times the absorption spectrum of the PNIHBr salt in toluene.....	130
<b>Figure S4.7</b> The electronic absorption spectra (multi-color, see legend) of supernatants after centrifugation of various perovskite-PNI hybrid species.	131
<b>Figure S4.8</b> Hydrodynamic radii distributions for (OA)(BA)PbBr <sub>4</sub> nanoplatelets (a) and (PNI) <sub>2</sub> PbBr <sub>4</sub> nanoplatelets (b) in toluene as determined by DLS.....	131
<b>Figure S4.9</b> TCSPC fluorescence intensity decay from PNI surfactants associated with (PNI) <sub>2</sub> PbBr <sub>4</sub> nanoplatelets in toluene. The red trace is a monoexponential decay curve fit to the TCSPC data with the residuals displayed above. Sample was excited by a 405 nm diode laser (56.5 ps fwhm) set to a 100 kHz repetition rate. A band-pass filter centered at 500 nm with a 45 nm width was used to select the emission. ....	132

# CHAPTER 1: Selected Fundamentals of the Photophysics and Spectroscopy of Semiconductor Nanomaterials

Portions of this chapter have been previously published: *Journal of the American Chemical Society*, **2020**, *142* (25), 10883–10893. DOI: 10.1021/jacs.0c03331

## 1.1 Photophysical Processes

### 1.1.1 Light Absorption

It all starts with the absorption of a photon. This is not uniformly true, because there are other ways to access excited states. A particularly enjoyable example is the oxidation of hydrogen peroxide by bleach to form oxygen in an excited state, along with water and sodium chloride. Excited states can also be generated by application of sufficient voltage. A reader interested in that topic but still wishing to follow this author is directed to the article “Realization of high-efficiency fluorescent organic light-emitting diodes with low driving voltage” by Salehi *et al.*<sup>1</sup> However, within the context of this dissertation, the processes of interest begin with absorption of a quantized amount of light energy, which we call a photon. So what does that entail? In order for a photon to be absorbed by a molecule, the energy of the photon must match the change in energy the molecule will experience. This relationship is described by the Bohr equation ( $h\nu = E_f - E_i$ ) (Eq. 1), where  $E_f$  and  $E_i$  correspond to the energies of the excited state  $\Psi_f$  and the ground state  $\Psi_i$ , respectively.<sup>2</sup>

$$h\nu = E_f - E_i \quad (\text{Eq. 1})$$

One other requirement for light absorption is for the transition between the ground and excited states to have a non-zero probability. The probability of the transition is proportional to the square of the transition moment, which is expressed in the ubiquitous bra-ket notation as  $\langle \Psi_i | \hat{\mu} | \Psi_f \rangle$ , where  $\hat{\mu}$  is the dipole moment operator.<sup>2</sup> Fortunately for

photophysicists and photochemists everywhere, the transition moment is easily simplified. Thanks to the Born-Oppenheimer approximation, the nuclear and electronic wavefunctions can be separated.<sup>3</sup> Once electrons and nuclei can be treated separately, applying Condon's approximation<sup>4</sup> allows the dipole moment operator to be considered independently from the nuclear coordinates. Finally, the old quantum chemistry trick of splitting electronic wavefunctions into orbital functions,  $\phi$ , and spin functions,  $S$ , leads to the following equation (Eq. 2), where  $\theta$  are the nuclear wavefunctions.

$$\langle \Psi_i | \hat{\mu} | \Psi_f \rangle = \langle \Phi_i | \hat{\mu} | \Phi_f \rangle \langle S_i | S_f \rangle \langle \theta_i | \theta_f \rangle \quad (\text{Eq. 2})$$

From Equation 2, the selection rules for electronic transitions are derived. The first integral concerns the electronic transition moment, and further analysis shows proper symmetry and sufficient orbital overlap are required for the transition to be electronically allowed. This integral is also the quantum mechanical basis for the Laporte selection rule often referenced in the context of d-d transitions in canonical transition metal coordination complexes. The second integral is assumed to be 1 for transitions occurring between initial and final states of the same spin multiplicity and 0 for all other transitions. The last integral is the physical basis for the well-known<sup>5</sup> Franck-Condon principle.<sup>2</sup>

### 1.1.2 Light Emission (Photoluminescence)

At its very core, luminescence has been a research topic of extensive scientific interest for centuries. As noted in Cecil Parker's book, *Photoluminescence of Solutions*, topics of light emission phenomena encompass electroluminescence, radioluminescence, chemiluminescence, bioluminescence, triboluminescence, sonoluminescence, and photoluminescence (PL).<sup>6</sup> In each instance, light is emitted from excited states generated by a variety of excitation stimuli. The reaction of bleach and peroxide mentioned earlier is also an example of chemiluminescence, as the excited oxygen molecules will emit light

as they relax to their ground state. If the reader was intrepid enough to venture out and read the article about light-emitting diodes,<sup>1</sup> they certainly witnessed some examples of electroluminescence. The subsection titles so far have hinted that the luminescence of interest herein is photoluminescence, where the excitation stimulus was the absorption of light energy.

As most organic molecules possess closed-shell (spin-singlet) ground states, the study of molecular light emission pathways primarily focuses on the relative populations of the lowest energy singlet ( $S_1$ ) and triplet ( $T_1$ ) excited states.<sup>7</sup> As one would expect from Hund's rules, the lowest triplet excited state is generally lower in energy with respect to the initially populated singlet excited state due to the exchange interaction. Exchange is a quantum-mechanical phenomenon, with no classical analogue, that arises as a consequence of electron indistinguishability and the Pauli exclusion principle. The aligned electron spins of the triplet state provide an energetic stabilization relative to the opposite spins of the singlet state.

Taking the singlet ground state ( $S_0$ ) into consideration, radiative transitions from  $S_1$  will be expected to have a spin integral equal to 1 and therefore be considered "spin-allowed". On the contrary, transitions from  $T_1$  to  $S_0$  are formally "spin-forbidden", but thermodynamics is a clever beast and these transitions do still occur. Spin-allowed photon emission is typically referred to as fluorescence, whereas formally spin-forbidden light emission processes are termed phosphorescence. The "allowed-ness" of the transition does at least determine the rate at which the process occurs, with fluorescence occurring much faster ( $\sim 10^{-7} > \tau > 10^{-10}$  s) than phosphorescence ( $\tau > 10^{-7}$  s).<sup>2</sup>

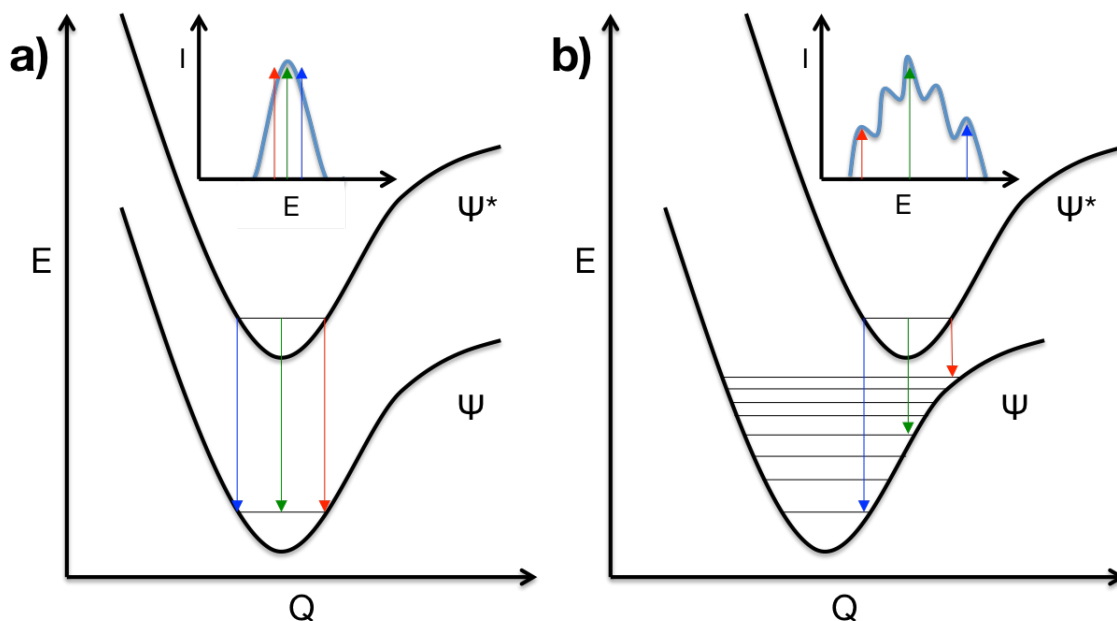


**Figure 1.1** A qualitative potential energy diagram showing the effects of (a) minimal and (b) large excited state distortion (Q) on the shape, structure, and broadness of emission bands (insets).

Experimentally obtained electronic absorption and photoluminescence spectra are rich texts. Information that can be garnered from the photoluminescence spectra include the shape, structure, and broadness of the emission, which yields qualitative information on the nature of the emissive excited state as well as the extent of excited state distortion (Figure 1.1). The breadth of the bands is easily conceptualized by following the radiative transitions denoted by colored arrows from low (Figure 1.1a) to high excited-state distortion (Figure 1.1b). The distribution of intensities rendered in the inset in Figure 1.1b can be explained from concepts first taught in undergraduate-level quantum mechanics. The probability density for the lowest vibrational state ( $v = 0$ ) of a given electronic state is centered within the potential energy well. Meanwhile, the highest probability densities for the higher vibrational levels ( $v \neq 0$ ) of said state are located along the “walls” where the lines denoting the vibrational states cross the curve denoting the electronic state.

### 1.1.3 Non-Radiative Processes

An alternative sub-heading could have been, “Why doesn’t everything glow?” The short answer is that there are a number of paths that excited molecules and materials can take to return to their ground state, and many of them are radiationless. Light absorption usually starts from the lowest vibrational state of the electronic ground state. Due to the Franck-Condon principle, these vertical transitions often arrive in higher vibrational levels of the electronic excited state. The excess vibrational energy is typically dissipated through thermal equilibrium with the surroundings in a process known as vibrational relaxation (Figure 1.2). Vibrational relaxation can be further subdivided into vibrational cooling (VC) and intramolecular vibrational redistribution (IVR). VC involves coupling between the molecule and its solvent environment, while IVR sees energy from the initially populated vibrational mode being dissipated among other vibrational modes in the molecule itself.<sup>2, 8</sup>

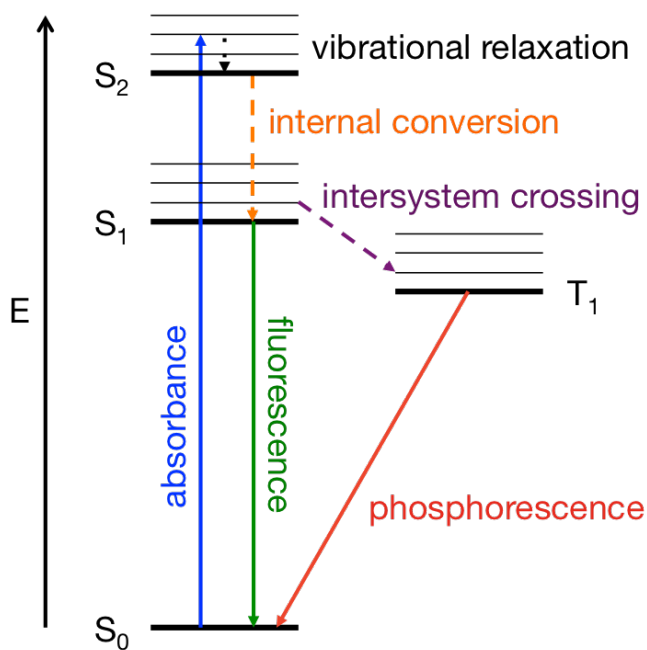


**Figure 1.2** Generalized Jablonski diagram featuring example photophysical processes. Non-radiative transitions are dashed while radiative transitions are solid.

Furthermore, excited molecules can undergo non-radiative transitions between excited states. As shown in Figure 1.2, internal conversion (IC) requires initial and final states of the same spin multiplicity (e.g.  $S_2 \rightarrow S_1$ ) while intersystem crossing (ISC) occurs between states of different spin (e.g.  $S_1 \rightarrow T_1$ ). In fact, in organic molecular photochemistry, the aforementioned lowest triplet excited states are typically accessed by initial spin-allowed population of a singlet excited state, followed by ISC to a lower energy triplet excited state. The dominant process of ISC in molecular photophysics occurs through spin-orbit coupling (SOC). The ISC transition can occur by direct SOC of the lowest singlet to higher vibrational levels of the lowest triplet, or by SOC to an upper triplet excited state, followed by rapid IC to the lowest triplet. Spin-orbit coupling is induced in part by conservation of the total angular momentum of the electrons in the molecule. The two most common manifestations of SOC in molecular photophysics are perturbation by a magnetic field, as seen in the heavy atom effect<sup>5</sup> or the presence of paramagnetic molecules, and El-Sayed's rules.<sup>9</sup> From a molecular design perspective, proximal effects are eschewed in favor of direct integration of functionalities that can directly induce SOC. For El-Sayed considerations, this requires molecules with energetically proximate ( $n,\pi^*$ ) and ( $\pi,\pi^*$ ) excited states. The heavy atom effect entails including atoms of high atomic number ( $Z$ ), including halogens such as iodine or 2nd and 3rd row transition metals. Increasing SOC can increase the rates of ISC into spin-forbidden triplet states. By the same token, increased proclivity toward ISC will also enhance the phosphorescence efficiency by increasing the "allowed-ness" of radiative relaxation to the ground state.

#### *1.1.4 Photoinduced Electron Transfer*

Excited molecules needn't only relax to the ground state all alone. If they come into contact with a suitable molecule, they can engage in a number of bimolecular processes, one of which is photoinduced electron transfer (PET). In PET, an electron is transferred from a donor to an acceptor in a redox process, and either the electron donor or acceptor species can be the one in an excited state.<sup>10,11</sup> The first criterion that must be met for PET to occur in solution is the electron being transferred must be moving to an orbital that is thermodynamically favorable. Generally, this requires the electron to come from a higher-energy orbital than its destination orbital, but more complex processes, such as Auger scattering, can also obey the laws of thermodynamics. Another requirement is wavefunction overlap between the two orbitals of interest. In bimolecular processes, this overlap is often collisional, which leads to a requirement that the excited state lifetime is sufficiently long to allow diffusion to result in collisions between excited species and the other species involved in the PET of interest. Examples of PET are laid out in Figure 1.3 with oxidative quenching illustrated in Figure 1.3a and reductive quenching demonstrated in Figure 1.3b. In either case, PET results in an oxidized donor and a reduced acceptor.

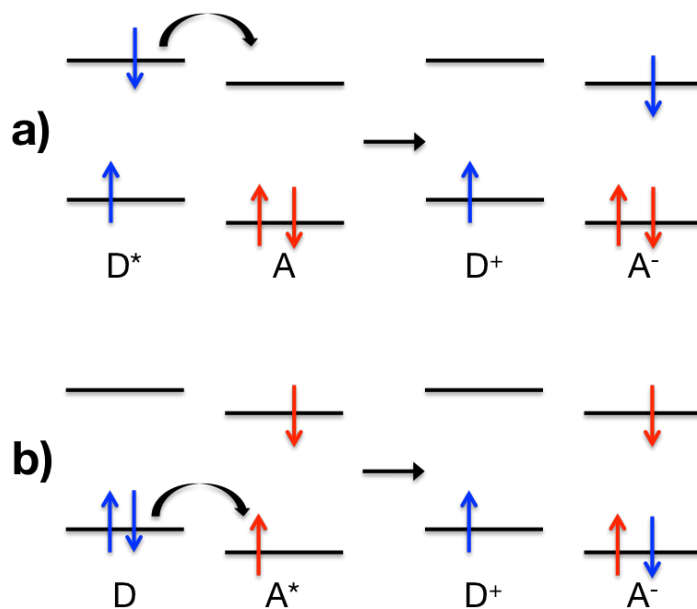


**Figure 1.3** Schematic illustration of photoinduced electron transfer processes, showing (a) oxidative quenching and (b) reductive quenching of the photoexcited species.

Alternative terminology for these processes instead labels the charge transfer processes with reference to the initial photoexcitation. This method consists of referring to oxidative quenching as electron transfer and reductive quenching as hole transfer. However, electron transfer and hole transfer both fall under the broader category of PET. Within the context of molecular photochemistry, where singlets and triplets are the typical spin states of concern, triplet excited states are the primary excited species involved in PET, owing to their longer excited-state lifetimes. It is also conceivable to have two successive electron transfer steps after which the initially excited molecule has returned to its ground state and the other molecule is now in an excited electronic state. This type of occurrence is termed indirect energy transfer, since the excited state energy has essentially been transferred from the original species to the new one by the consecutive electron transfer steps. If a two-step process is deemed indirect, then it stands to reason that a direct energy transfer process should take place in a single step.

### 1.1.5 Direct Energy Transfer Mechanisms

After discussing electron transfer processes, the most straightforward example of direct energy transfer is Dexter energy transfer.<sup>12</sup> The Dexter mechanism (Figure 1.4a), sometimes called exchange energy transfer, must have orbital overlap to occur, and often involves a collision between the excited-state donor and acceptor. Even in the absence of a collision, the two species need to be close ( $< 10 \text{ \AA}$  apart) to generate adequate wavefunction overlap. This mechanism necessitates concerted, two-electron exchange between the donor and acceptor species, with the end result of the donor in its ground state and a newly excited acceptor. The Dexter energy transfer rate constant is notoriously sensitive to the distance separating the donor and the acceptor, leading to extremely slow energy transfer rates at intermolecular distances greater than  $10 \text{ \AA}$ .

Dexter is the dominant mechanism for direct energy transfer from a triplet excited state, but for singlet energy transfer, it is outcompeted by a longer-range direct energy transfer mechanism called Förster resonance energy transfer (FRET). Illustrated in Figure 1.4b, FRET, also called fluorescence resonance energy transfer, resonance energy transfer, or dipole-dipole energy transfer, proceeds *via* dipolar coupling between the donor and acceptor. This dipolar coupling mechanism can be likened to the donor emitting a virtual photon absorbed by the acceptor.<sup>13</sup> This mechanism requires strong spectral overlap of donor photoluminescence and acceptor absorption, and functionally requires spin-allowed transitions. In molecular photophysics, with singlet ground states, FRET mostly proceeds from a donor in a singlet excited state, generating a singlet excited state on the acceptor. With sufficient spectral overlap, it is also possible to have the donor emit an actual photon that is subsequently absorbed by the acceptor. This

radiative energy transfer mechanism is somewhat trivial and should show no dependence on donor-acceptor separation distance.

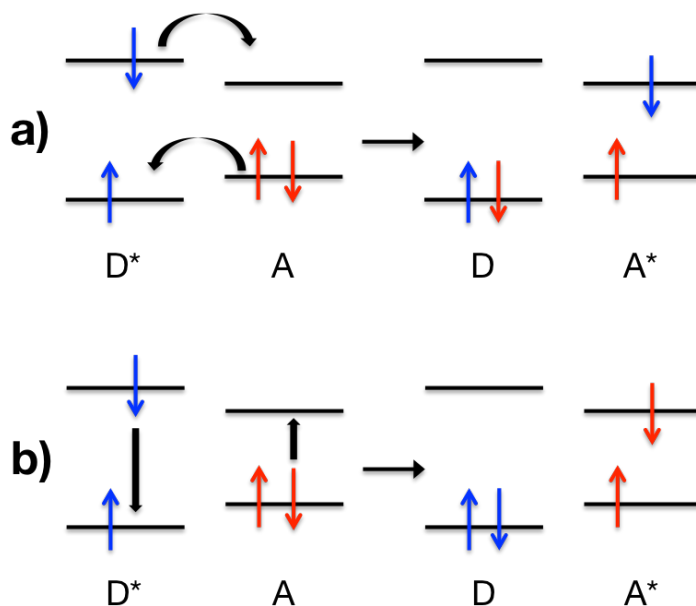


**Figure 1.4** Schematic illustration of direct energy transfer processes, showing (a) Dexter energy transfer and (b) FRET.

## 1.2 Photophysical Processes in Semiconductor Nanomaterials

### 1.2.1 Semiconductor Nanomaterials

What is a semiconductor? For an excellent introduction to solid-state physics from the perspective of an inorganic chemist, the reader is directed to “How Chemistry and Physics Meet in the Solid State” by Roald Hoffmann.<sup>14</sup> In addition to serving as a useful primer on concepts such as the Brillouin zone and density of states, the article also acknowledges NCSU Chemistry’s own Prof. Mike Whangbo. To grossly summarize a more detailed treatment, extended systems that show semiconducting behavior will possess a band gap that can, in some respects, be treated like a HOMO-LUMO gap for a molecule. However, these extended systems, being extended, are not nanomaterials. Nanomaterials, as the name suggests, are materials that typically have one to three

dimensions spanning from  $10^{-10}$  to  $10^{-7}$  m (the prefix “nano-” means  $10^{-9}$ ). With the invention and early development of scanning tunneling microscopy (STM) and in the early 1980's,<sup>15</sup> there was an explosion of research into the measurement and characterization of nanomaterials. In combination with other measurement and characterization techniques such as transmission electron microscopy (TEM), it became possible in that decade to investigate nanomaterials in much greater detail than ever before.

As part of that explosion, the effects of quantum confinement on nanoscale semiconductor crystallites were first reported in 1984.<sup>16</sup> In crystal size regimes where the diameter of the nanomaterial is the same order of magnitude as the calculated Bohr radius of the Wannier exciton, the charge carriers are spatially confined. The result is the band structure of the bulk semiconductor will begin to split into discrete quasi-molecular states. This process can be visualized with the help of Figure 1.5a. As a result of this quasi-molecular behavior, semiconductor nanomaterials have developed into a significant category of stable light-emitters. Moreover, as Figure 1.5b shows, they can be systematically tuned due to the size-dependence of the quantum confinement effect. Depending on the material composition and size regime employed, this can produce distinct absorption and photoluminescence bands spanning the electromagnetic spectrum from the UV to the near-infrared (NIR).<sup>17, 18</sup>

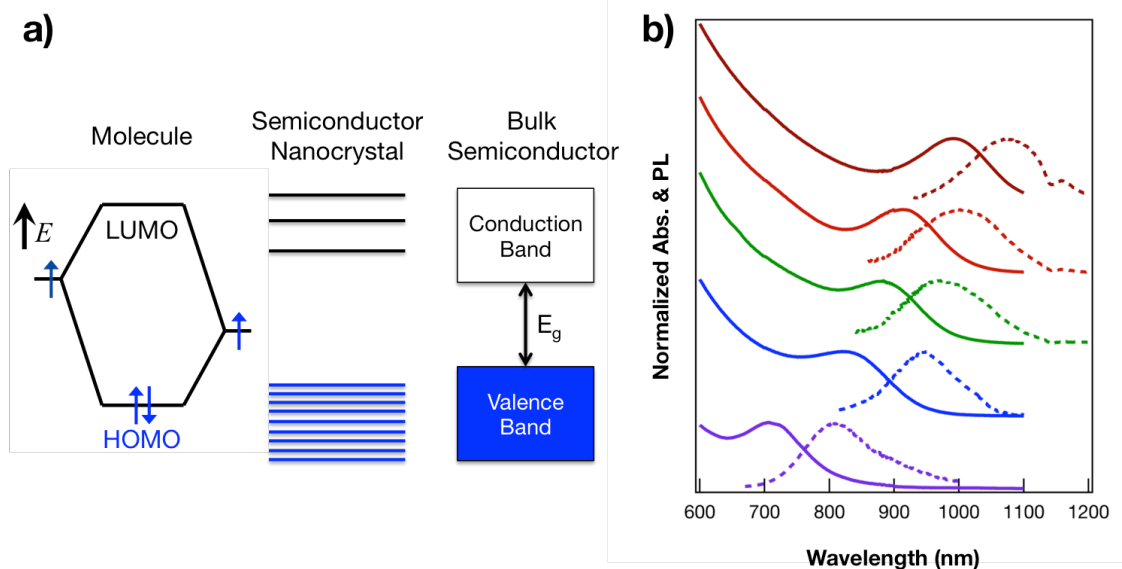


**Figure 1.5** Illustration of (a) electronic energy states of a semiconductor in the transition from discrete molecules to nano-sized crystals and bulk crystals. Blue shading denotes ground state electron occupation. Experimental (b) electronic absorption (solid) and photoluminescence (dashed) spectra of PbS semiconductor nanocrystals showing quantum confinement and size tunability. Figure 1.5a was adapted from ref. 19.<sup>19</sup>

### 1.2.2 Photosensitization from Semiconductor Nanomaterials

These quasi-molecular semiconductor nanomaterials potentially offer important improvements upon the molecular photosensitizer paradigm in a number of ways. They are trivial to synthesize, provide increased photostability, possess size-tunable electronic and photophysical properties, display high molar extinction coefficients, and are amenable to facile post-synthetic modification. Furthermore, the large and energy-consuming singlet-triplet energy gaps inherent in molecular sensitizers can be circumvented using this class of materials, with their ill-defined spin quantum numbers and closely spaced (1-15 meV) excited state energy levels.<sup>19, 20</sup> The absorption feature most reminiscent of those seen in molecules is typically found at the lowest energy (longest wavelength). The transition responsible for this absorption is typically also responsible for the narrow photoluminescence, which is displaced by a minimal Stokes

shift. Of the myriad electronic transitions possible in a semiconductor nanomaterial, this one most closely resembles the familiar HOMO-LUMO transition in molecules. At times in this document, this low energy peak in the electronic absorption spectrum will be referred to as the first exciton band or the first excitonic absorption band.

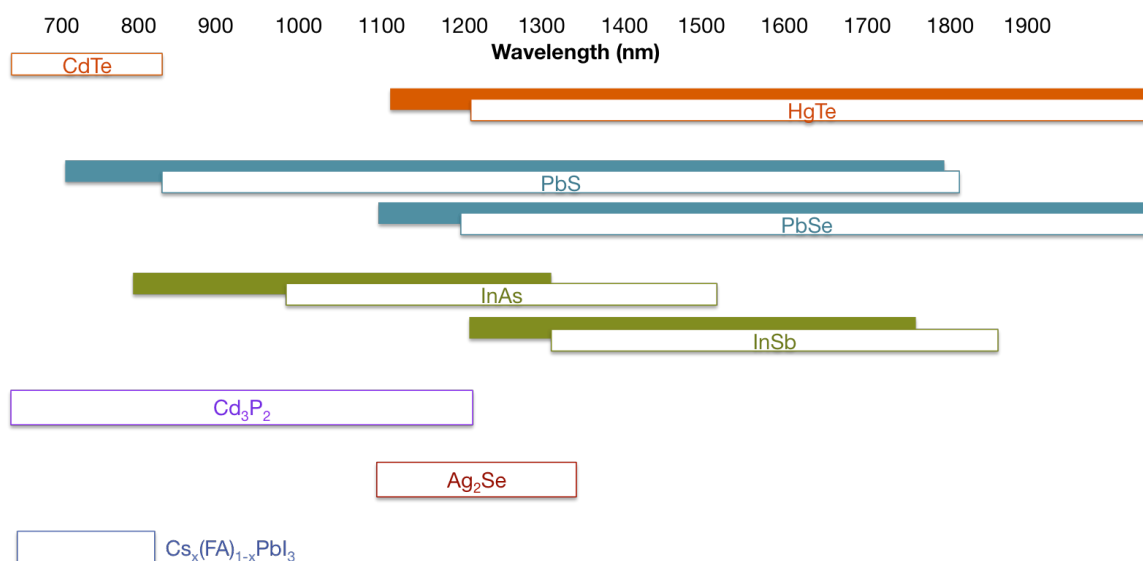


**Figure 1.6** Composition-based wavelength ranges of absorption (closed) and emission (open) for reported near-infrared-emitting nanomaterials prepared by solution-based methodologies.

In addition to the advantageous quasi-molecular properties that allow semiconductor nanomaterials to function as the next generation of molecular photosensitizers, light absorption can still extend into the NIR in some nanomaterials. A number of examples of these long wavelength emitters are featured in Figure 1.6. Constructing molecular photosensitizers capable of absorbing light in the NIR while remaining photostable is a daunting challenge that could be surmounted with semiconductor nanomaterials. In fact, many recent studies have demonstrated the benefit of these nanomaterials being paired with traditional organic chromophores to achieve exceptional triplet-triplet energy transfer efficiencies. Tabachnyk *et al.* and Thompson *et*

*al.* independently demonstrated Dexter-like triplet-triplet energy transfer (TTET) from organic molecules (as thin films) to PbS and PbSe QDs in 2014.<sup>21, 22</sup> These reports were followed in 2016 by the first direct observation of the reverse process, TTET from selectively excited CdSe NCs to surface-appended molecules.<sup>23</sup> In addition to observing TTET from CdSe to various organic molecules,<sup>24, 25</sup> the types of QDs that have successfully served as energized donors in TTET to surface anchored chromophores has recently expanded to include PbS,<sup>26-30</sup> CsPbBr<sub>3</sub>,<sup>31-34</sup> Si,<sup>35</sup> and CuInS<sub>2</sub>.<sup>36</sup> The compositions of interest herein are PbS and L<sub>2</sub>PbX<sub>4</sub>, and the latter will be introduced in greater depth in Chapter 4.

### **1.3 Spectroscopic Instrumentation and Techniques**

#### *1.3.1 Electronic Absorption Spectroscopy (UV-vis)*

For measuring light absorption, ultraviolet-visible (UV-vis) spectroscopy measures the relative absorption intensities of incident photons as a function of their wavelength across the UV-vis region of the electromagnetic spectrum. It can be utilized to determine the nature of the electronic transitions of a species like those mentioned above. It should also be familiar to anyone who has taken a general chemistry laboratory class for its analytical use to determine the concentration of molecules in solution.

Commercially available UV-vis spectrophotometers come in two different arrangements, single and dual beam. In a single beam spectrophotometer, the reference standard, or “blank,” is analyzed before any further analysis takes place. A typical blank in either type of UV-vis spectrophotometer is an empty substrate or an optical cell with the same solvent as the samples of interest. The dual beam alignment splits the incident light beam into two separate beams that are directed into an analytical sample and its

reference simultaneously. Broadly, dual beam spectrophotometers should allow for higher reproducibility and faster scans. However, one cannot necessarily prevent their coworkers from employing dual beam spectrophotometers as if they are single beam instruments.

Regardless of the number of beams, the instruments work by measuring the intensities of light passing through the blank ( $I_0$ ) and through a main sample of interest ( $I$ ). The light source for a typical UV-vis spectrophotometer uses both deuterium and halogen lamps to emit in the UV and visible regions, respectively. The other important components along with the light source are the monochromator and the detector. Traditionally, light from the source would pass through the monochromator, which would selectively send one wavelength at a time to the sample or reference and then scan across the UV-vis region. Eventually, the light reaches the detector, where the intensities of the sample and reference beams ( $I$  and  $I_0$ ) are determined. In these instruments, the common detector types are either a photomultiplier tube (PMT) or a photodiode. However, there are also newer, non-scanning UV-vis spectrophotometers, which place the diffraction grating component after the sample in the light path and employ detector arrays, to capture the entire spectrum at once.<sup>37</sup>

The relationship between the sample and reference intensities ( $I$  and  $I_0$ ) is the transmittance,  $T$ , given in Equation 3.

$$T = I/I_0 \quad (\text{Eq. 3})$$

Since transmittance values are necessarily between 0 and 1, it is often reported as a percentage to satisfy the human desire to deal with integers between 0 and 100. However, for analytical determinations such as concentration in dilute solution, absorbance ( $A$ ) is a

more straightforward value to use. Absorbance is derived from  $I$  and  $I_0$  by following Equation 4 and is related to concentration by the Beer-Lambert Law (Eq. 5).

$$A = -\log(T) = -\log(I/I_0) \quad (\text{Eq. 4})$$

$$A = \varepsilon \ell c \quad (\text{Eq. 5})$$

From Equation 5, it's clear that  $A$  is linearly related to concentration ( $c$ ). The other two terms are path length ( $\ell$ ) and molar absorptivity ( $\varepsilon$ ). The molar absorptivity, also known as the molar extinction coefficient or molar attenuation coefficient, can be related back to the quantum mechanical probability of the absorption transition by using oscillator strength ( $f$ ). First, treating the molecule as a classical oscillating dipole, the oscillator strength is extracted from the molar absorptivity by the integral over the absorption band in frequency or wavenumber units (Eq. 6).<sup>2</sup> Second, the oscillator strength can serve as a bridge from the classical to the quantum, because it is also related to the transition dipole moment,  $\langle \Psi_i | \hat{\mu} | \Psi_f \rangle$ , from subsection 1.1.1 (Eq. 7).<sup>2</sup>

$$f = 4.315 \times 10^{-9} \int \varepsilon d\nu \quad (\text{Eq. 6})$$

$$f = \frac{8\pi^3 \nu_{if} m_e}{3he^2} \langle \Psi_i | \hat{\mu} | \Psi_f \rangle^2 \quad (\text{Eq. 7})$$

In this way, the experimental intensity of the absorbance band can be used to say something more quantitative about the nature of the observed transition.

### 1.3.2 Steady-State Photoluminescence Spectroscopy

Steady-state photoluminescence spectral data are collected using a spectrofluorometer, often referred to as a fluorimeter for short. In the Castellano lab, all spectrofluorometers use a xenon arc lamp as the light source, which passes through an “excitation” monochromator to excite the sample with light centered on a specific wavelength (Figure 1.7). Light emitting from the sample is focused into a second

“emission” monochromator, which precedes the detector(s). The entrance to the emission monochromator is located perpendicular to the light path out of the emission monochromator to minimize the amount of excitation light scattered into the detector(s). The detectors used are photomultiplier tubes (PMTs) with single-photon counting for increased sensitivity. Photoluminescence spectra like those discussed in subsection 1.1.2 are collected as “emission spectra”, where the excitation wavelength is held constant and the emission monochromator is scanned across a desired spectral range. It is also possible to hold the emission wavelength constant on a band of interest and scan the excitation monochromator over some spectral range to generate an “excitation spectrum.” The excitation spectrum can sometimes be extremely useful for inferring the species responsible for certain photoluminescence bands or uncovering excited-state energy transfer processes.

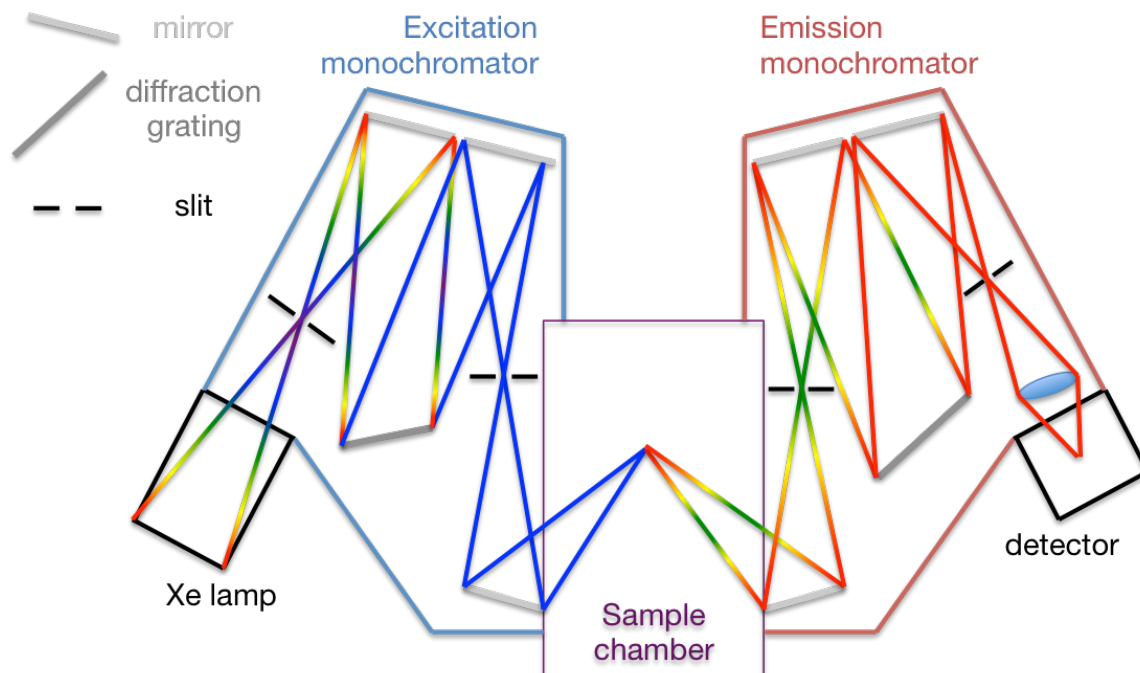


**Figure 1.7** Schematic diagram of a spectrofluorometer based on a continuous Xe light source, two Czerny-Turner monochromators, and a detector for sample emission.

### *1.3.3 Time-Resolved Photoluminescence Spectroscopy*

Among other criteria, time-resolved spectroscopy requires a pulsed excitation source, such as a pulsed lamp or a laser. At longer time scales ( $\tau > 10$  ns) for any data presented herein, wavelength-tunable excitation pulses are generated by either a N<sub>2</sub> laser-pumped dye laser or a Nd:YAG laser with an optical parametric oscillator (OPO). The dye laser excitation wavelength is a function of the laser dye chosen, but can also be configured to pass through the 337 nm pulses directly from the N<sub>2</sub> laser. The Nd:YAG/OPO system will be discussed more later, but briefly, it produces pulses with 5-7 ns fwhm from 310 nm to 2400 nm. The time-resolved photoluminescence (PL) data collected after excitation by the preceding sources take one of two forms, depending on the nature of the detector utilized. Single-wavelength kinetic traces are collected by directing the sample photoluminescence through a monochromator into either a PMT (for visible wavelengths) or an InGaAs photodiode (for near-infrared wavelengths). The detectors are connected to an oscilloscope, which is triggered by the arrival of the excitation pulse. This data is plotted with PL intensity on the ordinate and time on the abscissa with the knowledge that it was collected with the monochromator selecting a specific wavelength. The other possible detector involves diffraction of the emitted light into a charge-coupled device (CCD) camera. The CCD camera allows emission spectra to be collected over the entire visible region at once after a specific time delay following the excitation pulse. This data is plotted with PL intensity on the ordinate and wavelength on the abscissa with the knowledge that it was collected with the digital delay generator selecting a specific time delay after excitation.

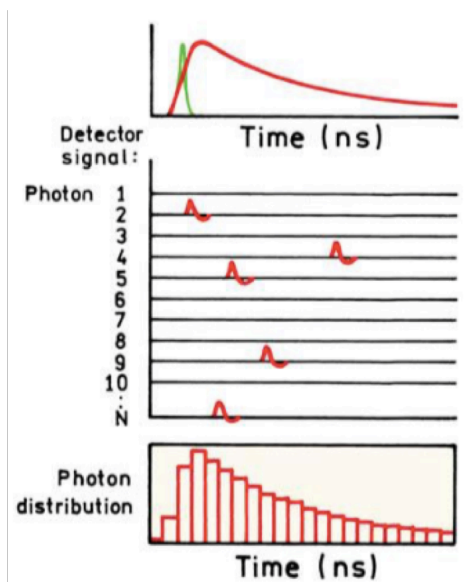


**Figure 1.8** The principle of TCSPC is illustrated by (top) the laser (green) and photoluminescence (red) waveforms, the detection of individual photons (middle) adding counts to time bins, and the constructed histogram (bottom) after many laser pulses. Figure was adapted from ref. 13.<sup>13</sup>

At shorter time scales ( $10 \text{ ns} > \tau > 10 \text{ ps}$ ), shorter excitation pulses and different post-detection electronics are required. The technique of time-correlated single photon counting (TCSPC) is based on the detection of single photons from an emissive sample at stochastic detection times after the laser pulse to create a histogram that resembles the original waveform (Figure 1.8).<sup>13</sup> The limit to the time resolution of TCSPC is electronic jitter, which introduces error on the order of 10's of picoseconds. In order to properly leverage TCSPC detection, pulsed excitation sources consist of diode lasers with fwhm  $\sim 50 \text{ ps}$  or Ti:sapphire lasers with pulses on the order of 100's of femtoseconds. The collection conditions for TCSPC are set such that there is less than 1 photon detected for every 20 pulses or more. This should eliminate the potential for a build-up error where multiple photons are detected within one pulse. At the time of the excitation pulse, a time-to-amplitude converter will initiate a voltage ramp, increasing linearly until a photon is detected or the next excitation pulse has arrived. If a photon arrived, a count is added to

one of the time channels corresponding to the voltage amplitude at the photon's arrival. After a user-defined number of counts (typically in the thousands) are reached in a single channel, the histogram formed should resemble the original waveform. For even shorter timescales ( $10 \text{ ps} > \tau > 100 \text{ fs}$ ), other fluorescence detection methods exist, such as optically gated fluorescence, also called "fluorescence upconversion."<sup>38</sup>

#### *1.3.4 Transient Absorption Spectroscopy*

If PL spectroscopy can be steady state and time resolved, why couldn't UV-vis be time-resolved as well? Time-resolved absorption spectroscopy with respect to photoexcitation of the analytical sample is known as transient absorption (TA) spectroscopy. TA spectroscopy measures the absorbance of the sample's excited states, generated after an excitation pulse interacts with the sample. This method is used to measure the absorption of excited states as a function of time after excitation, and it can also be used to monitor the kinetics of excited state decay processes. The general principle is that a species is excited at a particular wavelength to bring some fraction of the species within the excitation beam volume into an electronic excited state. The excitation pulse is then followed at specific time delays by a broadband "white light" probe to measure the absorbance of the sample following excitation. In the aforementioned "long" time domains ( $\tau > 10 \text{ ns}$ ), the delay between the excitation pulse and the white light pulse (typically a pulsed Xe lamp) can be controlled electronically, commonly termed nanosecond TA spectroscopy. In shorter time domains ( $10 \text{ ns} > \tau > 100 \text{ fs}$ ), the delay between the excitation and white light pulses is controlled optically, generally by employing a delay line. Delay lines utilize physical distance to force each pulse of light to traverse a different distance to reach the sample, allowing the time delay

to be calculated from the speed of light. This version of TA spectroscopy is referred to herein as ultrafast TA spectroscopy. Both types of TA experiment measure the change in absorbance between the ground and excited states. The collected data comes out as a difference spectrum, with  $\Delta A$  on the ordinate as a function of wavelength. The  $\Delta A$  values obtained at any specific time delay can be described as the mathematical difference between the absorptions of the ground and excited states.

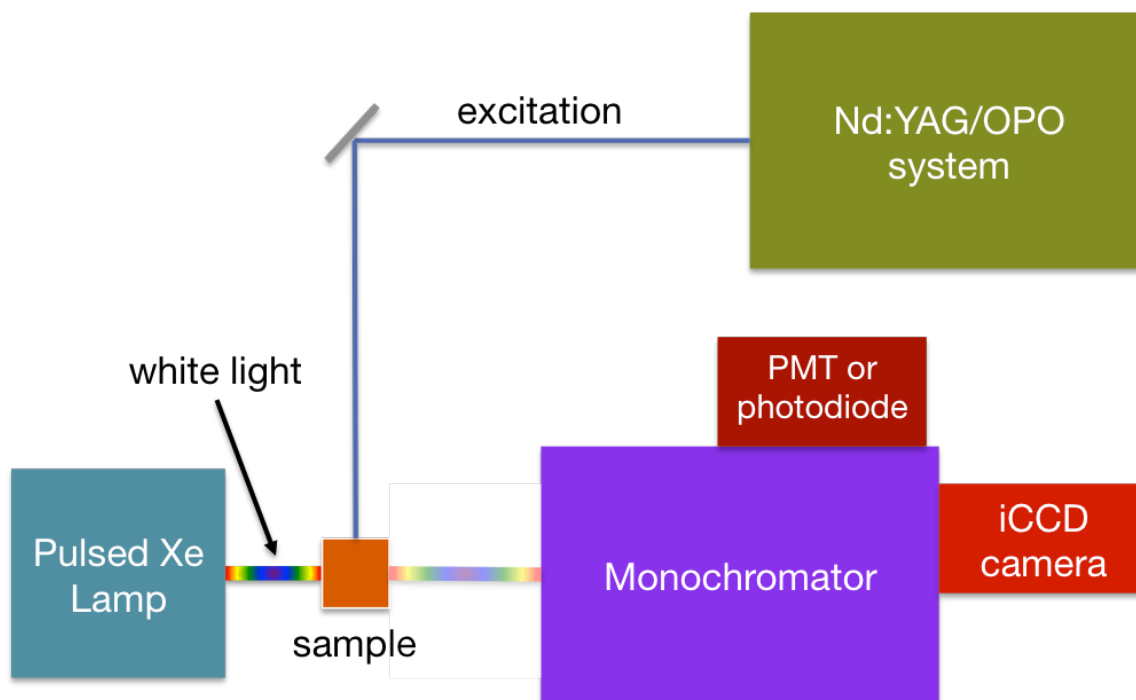


**Figure 1.9** Simplified schematic diagram of a nanosecond transient absorption spectrometer.

Nanosecond TA spectroscopy (Figure 1.9) uses a tunable excitation source, such as the Nd:YAG/OPO system briefly introduced in subsection 1.3.3 above. The Nd:YAG laser outputs 355 nm pulses to pump the OPO, which combines an optical resonator and a number of non-linear optics to generate the desired excitation wavelength.<sup>39</sup> Time zero is recorded by either directing the excitation beam into a photodiode trigger or by sending a signal from the Q-switch to the instrument. The broadband probe from the pulsed xenon

arc lamp is passed through the sample perpendicular to the excitation beam. As discussed previously, the detectors can be configured for either single-wavelength kinetics or time-gated spectra. As a reminder, single-wavelength kinetics pass the white light through a monochromator to a PMT or photodiode connected to an oscilloscope, while time-gated spectra involve diffraction of the white light into a CCD camera. Unlike PL spectra and kinetics, TA spectra and kinetics cannot be obtained in a single event. Instead, the instrument first uses a shutter to block the excitation pulse, allowing the probe to pass through the unexcited sample and serve as a background representing the ground state. Next, the excitation pulse is allowed to reach the sample, and the probe is again passed through the sample to the detectors. Calculating the difference in the detector responses gives the  $\Delta A$  values with respect to either time (at a fixed wavelength) or wavelength (at a fixed time).

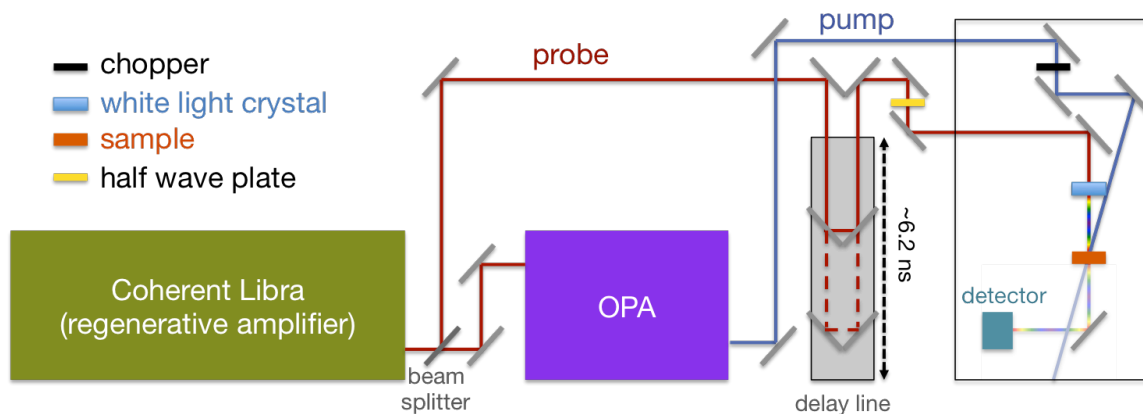


**Figure 1.10** Simplified schematic diagram of an ultrafast transient absorption spectrometer.

As mentioned previously, nanosecond TA can use electronics to control the delay between the pump and probe pulses, but ultrafast TA requires the use of a delay line. As part of that, the pump and probe pulses are both generated from the output of the same laser (Figure 1.10). To generate a sufficiently short pulse for time resolution down to

100's of femtoseconds with enough power to generate a pump and probe from the same beam, a regenerative amplifier is employed. A Coherent Libra directs a mode-locked Ti:sapphire laser (pumped by a CW diode) through chirped pulse amplification to serve as the seed laser for the regenerative amplifier, which is then pumped by a 1 kHz, intracavity doubled Nd:YLF laser. The regenerative amplifier produces 800 nm pulses (100 fs fwhm, 4 mJ/pulse), which are directed into a beam splitter to separate the pump and probe beams. The pump is directed into an optical parametric amplifier (OPA), which operates similarly to an OPO, but without the optical resonator, meaning the beam passes through only once, to generate the desired excitation wavelength. The pump continues through a chopper, operating at 500 Hz, to prevent every other pump pulse from reaching the sample, allowing for measurements with and without excitation and calculation of  $\Delta A$  at each delay time. Finally, the pump reaches the sample, and it does so along a path that keeps it from entering the detector optics. The probe beam is routed around the OPA and into the delay line, made up of mirrors that move along a motorized track, which alters the distance traversed by the probe pulse before reaching sample. In this way, a temporal delay between the pump and probe pulses has now been created. The probe can continue to a half-wave plate, where it is polarized to the magic angle ( $54.7^\circ$ ) relative to the polarization of the pump to remove rotational artifacts. The 800 nm probe can be converted into one of three broadband white light continua using one of three white light generating crystals. The crystals generate broadband output across the UV-visible ( $\text{CaF}_2$  crystal, 340-750 nm), visible (sapphire crystal, 425-775 nm), and NIR ["NIR crystal" (thicker sapphire), 825-1500 nm] spectral regions. At the sample, the pump and probe must be overlapped spatially as well as temporally in order to generate

meaningful TA data. Finally, the transmitted probe light is directed through some filtering optics and into a fiber optic cable leading to either a UV-visible (for the CaF<sub>2</sub> and sapphire crystals) or NIR (for the NIR crystal) detector array.

## 1.4 References

1. Salehi, A.; Dong, C.; Shin, D.-H.; Zhu, L.; Papa, C. M.; Thy Bui, A.; Castellano, F. N.; So, F., Realization of high-efficiency fluorescent organic light-emitting diodes with low driving voltage. *Nature Communications* **2019**, *10* (1), 2305.
2. Balzani, V.; Ceroni, P.; Juris, A., *Photochemistry and Photophysics: Concepts, Research, Applications*. Wiley-VCH: Weinheim, Germany, 2014.
3. Born, M.; Oppenheimer, R., Zur Quantentheorie der Molekeln. *Annalen der Physik* **1927**, *389* (20), 457-484.
4. Condon, E., A Theory of Intensity Distribution in Band Systems. *Physical Review* **1926**, *28* (6), 1182-1201.
5. IUPAC, Compendium of Chemical Terminology. In *the "Gold Book"* [Online] 2nd ed.; McNaught, A. D.; Wilkinson, A., Eds. Blackwell Scientific Publications: Oxford, 1997.
6. Parker, C. A., *Photoluminescence of Solutions*. Elsevier Publishing Company: Amsterdam, New York, 1968; p 544.
7. Turro, N. J., *Modern Molecular Photochemistry*. 1991.
8. Rosspeintner, A.; Lang, B.; Vauthey, E., Ultrafast Photochemistry in Liquids. *Annual Review of Physical Chemistry* **2013**, *64* (1), 247-271.
9. El-Sayed, M. A., Origin of the Phosphorescence Radiation in Aromatic Hydrocarbons. *Nature* **1963**, *197* (4866), 481-482.
10. Ramamurthy, V.; Schanze, K. S., *Organic and Inorganic Photochemistry*. Marcel Dekker: New York, 1998.
11. Vlček, A., Highlights of the spectroscopy, photochemistry and electrochemistry of [M(CO)<sub>4</sub>( $\alpha$ -diimine)] complexes, M=Cr, Mo, W. *Coordination Chemistry Reviews* **2002**, *230* (1), 225-242.
12. Dexter, D. L., A Theory of Sensitized Luminescence in Solids. *Journal of Chemical Physics* **1953**, *21* (5), 836-850.
13. Lakowicz, J. R., *Principles of Fluorescence Spectroscopy*. 3rd ed.; Springer: New York, 2006.
14. Hoffmann, R., How Chemistry and Physics Meet in the Solid State. *Angewandte Chemie International Edition* **1987**, *26* (9), 846-878.
15. Binnig, G.; Rohrer, H.; Gerber, C.; Weibel, E., Surface Studies by Scanning Tunneling Microscopy. *Physical Review Letters* **1982**, *49* (1), 57-61.
16. Brus, L. E., Electron-electron and electron - hole interactions in small semiconductor crystallites: The size dependence of the lowest excited electronic state. *The Journal of Chemical Physics* **1984**, *80* (9), 4403-4409.
17. Garakyaraghi, S.; Castellano, F. N., Nanocrystals for Triplet Sensitization: Molecular Behavior from Quantum-Confined Materials. *Inorganic Chemistry* **2018**, *57* (5), 2351-2359.
18. Lu, H.; Carroll, G. M.; Neale, N. R.; Beard, M. C., Infrared Quantum Dots: Progress, Challenges, and Opportunities. *ACS Nano* **2019**.
19. Smith, A. M.; Nie, S., Semiconductor Nanocrystals: Structure, Properties, and Band Gap Engineering. *Accounts of Chemical Research* **2010**, *43* (2), 190-200.

20. Scholes, G. D., Controlling the optical properties of inorganic nanoparticles. *Advanced Functional Materials* **2008**, *18* (8), 1157-1172.
21. Tabachnyk, M.; Ehrler, B.; Gelinias, S.; Boehm, M. L.; Walker, B. J.; Musselman, K. P.; Greenham, N. C.; Friend, R. H.; Rao, A., Resonant energy transfer of triplet excitons from pentacene to PbSe nanocrystals. *Nature Materials* **2014**, *13* (11), 1033-1038.
22. Thompson, N. J.; Wilson, M. W. B.; Congreve, D. N.; Brown, P. R.; Scherer, J. M.; Bischof, T. S.; Wu, M.; Geva, N.; Welborn, M.; Van Voorhis, T.; Bulovic, V.; Bawendi, M. G.; Baldo, M. A., Energy harvesting of non-emissive triplet excitons in tetracene by emissive PbS nanocrystals. *Nature Materials* **2014**, *13* (11), 1039-1043.
23. Mongin, C.; Garakyaraghi, S.; Razgoniaeva, N.; Zamkov, M.; Castellano, F. N., Direct observation of triplet energy transfer from semiconductor nanocrystals. *Science* **2016**, *351* (6271), 369-372.
24. Xu, Z. H.; Jin, T.; Huang, Y. M.; Mulla, K.; Evangelista, F. A.; Egap, E.; Lian, T. Q., Direct triplet sensitization of oligothiophene by quantum dots. *Chemical Science* **2019**, *10* (24), 6120-6124.
25. De Roo, J.; Huang, Z.; Schuster, N. J.; Hamachi, L. S.; Congreve, D. N.; Xu, Z.; Xia, P.; Fishman, D. A.; Lian, T.; Owen, J. S.; Tang, M. L., Anthracene Diphosphate Ligands for CdSe Quantum Dots; Molecular Design for Efficient Upconversion. *Chemistry of Materials* **2020**, *32* (4), 1461-1466.
26. Garakyaraghi, S.; Mongin, C.; Granger, D. B.; Anthony, J. E.; Castellano, F. N., Delayed Molecular Triplet Generation from Energized Lead Sulfide Quantum Dots. *Journal of Physical Chemistry Letters* **2017**, *8* (7), 1458-1463.
27. Huang, Z.; Xu, Z.; Mahboub, M.; Li, X.; Taylor, J. W.; Harman, W. H.; Lian, T.; Tang, M. L., PbS/CdS Core-Shell Quantum Dots Suppress Charge Transfer and Enhance Triplet Transfer. *Angewandte Chemie-International Edition* **2017**, *56* (52), 16583-16587.
28. Kroupa, D. M.; Arias, D. H.; Blackburn, J. L.; Carroll, G. M.; Granger, D. B.; Anthony, J. E.; Beard, M. C.; Johnson, J. C., Control of Energy Flow Dynamics between Tetracene Ligands and PbS Quantum Dots by Size Tuning and Ligand Coverage. *Nano Letters* **2018**, *18* (2), 865-873.
29. Bender, J. A.; Raulerson, E. K.; Li, X.; Goldzak, T.; Xia, P.; Van Voorhis, T.; Tang, M. L.; Roberts, S. T., Surface States Mediate Triplet Energy Transfer in Nanocrystal-Acene Composite Systems. *Journal of the American Chemical Society* **2018**, *140* (24), 7543-7553.
30. Papa, C. M.; Garakyaraghi, S.; Granger, D. B.; Anthony, J. E.; Castellano, F. N., TIPS-pentacene triplet exciton generation on PbS quantum dots results from indirect sensitization. *Chemical Science* **2020**, *11* (22), 5690-5696.
31. Luo, X.; Lai, R. C.; Li, Y. L.; Han, Y. Y.; Liang, G. J.; Liu, X.; Ding, T.; Wang, J. H.; Wu, K. F., Triplet Energy Transfer from CsPbBr<sub>3</sub> Nanocrystals Enabled by Quantum Confinement. *Journal of the American Chemical Society* **2019**, *141* (10), 4186-4190.
32. Han, Y. Y.; Luo, X.; Lai, R. C.; Li, Y. L.; Liang, G. J.; Wu, K. F., Visible-Light-Driven Sensitization of Naphthalene Triplets Using Quantum-Confined

- CsPbBr<sub>3</sub> Nanocrystals. *Journal of Physical Chemistry Letters* **2019**, *10* (7), 1457-1463.
33. Luo, X.; Liang, G. J.; Wang, J. H.; Liu, X.; Wu, K. F., Picosecond multi-hole transfer and microsecond charge-separated states at the perovskite nanocrystal/tetracene interface. *Chemical Science* **2019**, *10* (8), 2459-2464.
  34. Luo, X.; Han, Y. Y.; Chen, Z. W.; Li, Y. L.; Liang, G. J.; Liu, X.; Ding, T.; Nie, C. M.; Wang, M.; Castellano, F. N.; Wu, K. F., Mechanisms of triplet energy transfer across the inorganic nanocrystal/organic molecule interface. *Nature Communications* **2020**, *11* (1).
  35. Xia, P.; Raulerson, E. K.; Coleman, D.; Gerke, C. S.; Mangolini, L.; Tang, M. L.; Roberts, S. T., Achieving spin-triplet exciton transfer between silicon and molecular acceptors for photon upconversion. *Nature Chemistry* **2020**, *12* (2), 137-144.
  36. Han, Y.; He, S.; Luo, X.; Li, Y.; Chen, Z.; Kang, W.; Wang, X.; Wu, K., Triplet Sensitization by “Self-Trapped” Excitons of Nontoxic CuInS<sub>2</sub> Nanocrystals for Efficient Photon Upconversion. *Journal of the American Chemical Society* **2019**, *141* (33), 13033-13037.
  37. Skoog, D. A.; Holler, F. J.; Crouch, S. R., *Principles of Instrumental Analysis*. 7th ed.; Cengage Learning: Boston, MA, 2018
  38. Mahr, H.; Hirsch, M. D., An optical up-conversion light gate with picosecond resolution. **1975**, *13* (2), 96-99.
  39. Orr, B. J.; Haub, J. G.; White, R. T., Spectroscopic Applications of Pulsed Tunable Optical Parametric Oscillators. In *Tunable Laser Applications*, 3rd ed.; Duarte, F. J., Ed. CRC Press: Boca Raton, FL, 2016; pp 17–142.

## CHAPTER 2: TIPS-Pentacene Triplet Exciton Generation on PbS Quantum Dots

### Results from Indirect Sensitization

This chapter has been previously published: *Chemical Science*, **2020**, *11* (22), 5690–5696. DOI: 10.1039/D0SC00310G

#### 2.1 Abstract

Many fundamental questions remain in the elucidation of energy migration mechanisms across the interface between semiconductor nanomaterials and molecular chromophores. The present transient absorption study focuses on PbS quantum dots (QDs) of variable size and band-edge exciton energy (ranging from 1.15 to 1.54 eV) post-synthetically modified with a carboxylic acid-functionalized TIPS-pentacene derivative (TPn) serving as the molecular triplet acceptor. In all instances, selective excitation of the PbS NCs at 743 nm leads to QD size-dependent formation of an intermediate with time constants ranging from 2-13 ps, uncorrelated to the PbS QD valence band potential. However, the rate constant for the delayed formation of the TPn triplet excited state markedly increases with increasing PbS conduction band energy, featuring a parabolic Marcus free energy dependence in the normal region. These observations provide evidence of an indirect triplet sensitization process being inconsistent with a concerted Dexter-like energy transfer process. The collective data are consistent with the generation of an intermediate resulting from hole trapping of the initial PbS excited state by midgap states, followed by formation of the TPn triplet excited state whose rate constant and yield increases with decreasing quantum dot size.

#### 2.2 Introduction

Inorganic-organic hybrid materials constructed from semiconductor nanocrystals (NCs) with appended chromophoric molecules have found increasingly widespread use

for a number of light-harvesting and light-emitting functions.<sup>1-3</sup> Most of these photonic processes rely on formally spin-triplet excited states, which are generally long-lived in organic molecules owing to their singlet ground states making radiative transitions spin-forbidden while possessing relatively low intrinsic spin-orbit coupling.<sup>4,5</sup> Meanwhile, triplet excited states are more easily accessed in inorganic semiconductor NCs due to their ill-defined (nearly isoenergetic) spin states following light absorption.<sup>6</sup> The earliest reports of triplet exciton transfer in such hybrid materials incorporated PbS or PbSe NCs coated with a thin film of tetracene or pentacene. These constructs relied on singlet fission<sup>7,8</sup> to generate triplet excitons in these molecular films that ultimately transferred to the NC triplet acceptors.<sup>9,10</sup> Subsequent to these reports, our laboratory discovered triplet-triplet energy transfer occurring in the reverse direction in toluene solutions featuring selectively photoexcited CdSe NCs with surface-anchored anthryl or pyrenyl molecules.<sup>11</sup> This investigation provided clear cut experimental evidence for direct Dexter-type energy transfer occurring across the CdSe quantum dot-molecule interface.<sup>12</sup>

However, PbS quantum dots, while unequivocally generating molecular triplet excitons following direct excitation of the NC,<sup>13-16</sup> have proven more mechanistically complex with respect to CdSe. Of particular importance was the identification of an unusual photogenerated reaction intermediate that appeared when 6,13-*bis*(triisopropylsilylethynyl)pentacene-2-carboxylic acid (TPn),<sup>13</sup> a closely related structural derivative of TIPS-pentacene, was anchored to the surface of PbS NCs. This observation was attributed to a sluggish hole trapping process that produced a charge separated state between PbS(e<sup>-</sup>) and TPn<sup>•+</sup> and upon recombination generated the triplet excited state of TPn. A more recent account offered for PbS quantum dots'

spectroscopically-observed deviation from traditional Dexter-type direct TTET relied on quantum chemical calculations to implicate a theoretical NC surface-localized excited state as the kinetic intermediate.<sup>16</sup>

To continue the mechanistic analysis of this hybrid system, four sizes of PbS NC were synthesized. Upon post-synthetic modification of the PbS NC surfaces with TPn, the sub-picosecond to supra-nanosecond dynamics of these systems were studied using transient absorption spectroscopy. Kinetic analysis of the experimental data indicates the conservation of a stepwise energy transfer mechanism from PbS NCs to TPn, irrespective to the size or band-gap energy of the NC. The rates of the second step in the stepwise mechanism suggest Marcus free energy dependence in the normal region. These results will be rationalized within the context of surface-trapped holes mediating triplet energy transfer.

## **2.3 Experimental**

### *2.3.1 Nanomaterial synthesis and characterization*

**Quantum dot syntheses.** Oleate-capped PbS NCs were synthesized by adapting previously reported procedures.<sup>13, 17</sup> For the smallest PbS NC sizes, the sulfide precursor injection temperature was lowered from 110°C to 95°C for PbS-945 or 80°C for PbS-805. While multiple batches per NC size were synthesized to ensure future synthetic reproducibility, all experiments (ligand exchanges, spectroscopy, and materials characterization) were performed on a single synthetic batch to eliminate batch-to-batch inhomogeneity. TPn was synthesized and structurally characterized as published previously.<sup>18</sup>

**Ligand exchange with TPn.** The oleate-capped PbS NCs were subjected to well established ligand exchange procedures.<sup>11, 13-16, 19-21</sup> Briefly, oleate-capped NCs were suspended in toluene to which TPn was added to initiate 1:1 X-type ligand exchange<sup>15</sup> with the oleate ligands. The NC-TPn hybrids were then purified by successive precipitation-centrifugation-resuspension and filtration steps. The average NC:TPn ratio was determined *via* UV-vis absorption spectroscopy. These values were found to be 1:20.7 for PbS-805-TPn, 1:33.2 for PbS-970-TPn, 1:42.3 for PbS-1000-TPn, and 1:53.9 for PbS-1075-TPn for time resolved spectroscopy samples. Treating the PbS NCs as spheres to calculate their surface areas, these TPn loadings give bound TPn molecules per nm<sup>2</sup> values of 1.35, 1.29, 1.52, and 1.54, respectively. From the dimensions of the unit cell for crystalline TIPS-pentacene, a maximum theoretical surface density can be set at 1.65 molecules/nm<sup>2</sup>. These surface densities, especially for PbS-1075-TPn and PbS-1000-TPn, are broadly consistent with NCs that are at their maximum functional surface density of TPn molecules. PbS-970-TPn, meanwhile, gives a significantly lower value than PbS-1000-TPn. This could be due to the average diameter of the PbS-970-TPn ensemble (2.9 nm) deviating furthest from the possible vertex-to-vertex lengths for idealized PbS cuboctahedra (Figure S2.19). The relevant PbS cuboctahedron vertex-to-vertex lengths for this study are 2.17 nm, 2.55 nm, 3.00 nm, and 3.40 nm. The implication is that PbS-970 NCs contain the highest percentage of S-terminated NCs, lowering the effective Pb surface area of the ensemble. The lack of available Pb atoms for the TPn molecules to bind can be used to rationalize the low surface density on PbS-970-TPn. The surface density on PbS-805-TPn is higher than that on PbS-970-TPn, but not as high as PbS-1000-TPn and PbS-1075-TPn, in spite of an ensemble average (2.2 nm)

close to an idealized length (2.17 nm). This may be due to the practical loading limit beginning to approach 1 molecule per face (14 molecules per cuboctahedron) in the smallest NCs.

**Static spectroscopy.** Electronic absorption spectra were measured on a Shimadzu UV-3600 UV-vis-NIR spectrophotometer. Steady-state photoluminescence spectra were measured on an Edinburgh Instruments FS920 fluorescence spectrometer equipped with both a visible and a near-infrared photomultiplier tube. Excitation at 743 nm was achieved by a 450 W Xe arc lamp equipped with a monochromator and appropriate long pass filters.

**Electron microscopy.** Transmission Electron Microscopy (TEM) experiments were carried out using a JEM 2000FX Scanning TEM (JEOL). Images were acquired at an accelerating voltage of 200 kV. Samples were prepared by evaporation of dilute NC suspensions in toluene that had been dropped onto an ultrathin carbon film on a lacey carbon support film on a 400 mesh Cu TEM grid. Size distributions were measured using ImageJ software (<https://imagej.nih.gov/ij/>). Particle sizing was done with the software's analyze particle function, after selection of an appropriate contrast threshold for the images. Scanning Electron Microscopy with Energy Dispersive X-ray Spectroscopy (SEM-EDS) was carried out on a FEI Verios 460L field-emission SEM (Thermo Fisher Scientific) equipped with a Si Drift Detector (Oxford Instruments). SEM-EDS samples were prepared by evaporation of dilute NC suspensions in toluene that had been dropped onto atomically smooth Si wafers.

### 2.3.2 Time-resolved spectroscopic methods

**Ultrafast transient absorption spectroscopy.** Ultrafast transient absorption spectroscopy measurements were performed using an amplified Ti:sapphire laser system described previously in the literature.<sup>22</sup> Briefly, the output from a Coherent Libra 1 kHz Ti:Sapphire regenerative amplifier (4 mJ/pulse, 100 fs fwhm at 800 nm) was split into pump and probe beams. The pump beam was directed into an optical parametric amplifier (Coherent OPerA Solo) to generate tunable excitation (743 nm) while the probe beam was delayed in a 6.2 ns optical delay stage before being broadened by a nonlinear optical crystal into broadband white light (sapphire to generate the probe light for visible TA or a proprietary crystal to generate the probe light for NIR TA) before passing through the sample. The two beams were focused and spatially overlapped with the relative polarization of the pump and probe beams set to the magic angle of 54.7°. NC suspensions were measured in 2 mm path length quartz cuvettes and stirred constantly to alleviate local heating from the laser pulses. The PbS and PbS-TPn solutions were prepared to possess optical densities (OD) of approximately 0.06 at 743 nm. The transient absorption difference spectra and kinetics were obtained using a Helios transient absorption spectrometer (Ultrafast Systems), averaging four scans and using 2 s of averaging at every given delay. The ground state absorption spectra were taken before and after each experiment using an Agilent 8453 UV-visible spectrophotometer to ensure there was no sample decomposition.

**Nanosecond transient absorption spectroscopy.** Nanosecond TA measurements were executed using a LP920 spectrometer (Edinburgh Instruments). An iStar ICCD camera (Andor Technology) was used to obtain transient difference spectra. Single-

wavelength kinetics were collected on either a visible light PMT or an InGaAs photodiode for NIR detection. The excitation source was a tunable Vibrant 355 Nd:YAG/OPO system (OPOTEK) tuned to 743 nm (1 mJ/pulse, 5-7 ns fwhm). While this excitation power is sufficient to generate multiple excitons in PbS NCs, multiexciton processes such as biexciton and triexciton annihilation are expected to be significantly shorter-lived than the pulse duration (5-7 ns fwhm). The excitation source operated at 1 Hz and 3.3 Hz for spectra and kinetics acquisitions, respectively. Appropriate long pass filters were used to remove residual leaking light from the excitation source. The samples were deaerated by a minimum of three freeze-pump-thaw degassing cycles. The PbS and PbS-TPn samples were diluted to OD of approximately 0.06 at 743 nm.

**Extracting kinetic rate constants from transient absorption spectra.** Ultrafast transient absorption (TA) spectra were fit using a model based on the assumption that the time-resolved TA spectra of these hybrid materials can be linearly decomposed as the sum of time-independent decay-associated difference spectra (DADS) with specific time-dependent amplitudes.<sup>23</sup> Under this assumption, each DADS is therefore presumed to represent the TA spectrum of an individual excited state in the system. The time-dependent amplitudes correspond to the concentration or population of their respective DADS. In solving for these values from the PbS-TPn TA data, each DADS was assumed to interconvert to the next in a sequential, first order fashion.

Three DADS and an additional fitting parameter could model the complete ultrafast TA spectral datasets for all PbS-TPn materials studied. The additional fitting parameter, resembling a fourth DADS, is included in the model to account for a nonlinear response feature from the toluene occurring coincidentally with the impulse response

function (IRF). The spectra produced by the model appear in Figures 2.3a-d.

Additionally, the fits obtained from the model are compared to the experimental data at the end of the Supplementary Information (Figures S2.12-S2.18). The PbS-TPn TA data was fit separately for the individual white light continua in the visible and NIR, respectively, and the corresponding rate constants were found to be in excellent agreement. The kinetic rate constants extracted from the model have been used to interpret the experimental data (Table S2.3).

## 2.4 Results and Discussion

The four sizes of PbS NC that were synthesized are displayed in Figure 2.1a&b. Consistent with quantum-confined semiconductor nanomaterials, the lowest energy PbS NC exciton absorbance maximum shifts to higher energies with decreasing PbS NC average diameter,<sup>24-27</sup> supported by analysis of TEM images (Figure S2.1). The wavelength of maximum photoluminescence intensity shifts in concert with the maximum absorbance wavelength in the first exciton band. The PbS NCs possess photoluminescence intensity maxima near 805, 970, 1000, and 1075 nm, and will be referred to as PbS-805, PbS-970, PbS-1000, and PbS-1075. In the ensuing discussion, it is more physically accurate (see Experimental) to consider PbS-970 and PbS-1000 as ensembles of the same NC size but with vastly different surfaces. Therefore, the two species may be treated as an internal control experiment on the relative influence of band edge energies against surface chemistry effects.

As a representative example of the change in electronic effects upon surface-functionalization, the absorption and photoluminescence spectra for PbS-1075 before and after ligand exchange of oleate to TPn and subsequent purification are given in Figure

2.1c. The absorption spectrum of free TPn is included for reference. The corresponding spectra for all other hybrid materials subjected to TA spectroscopy are presented in Figure S2.2. While the colloidal NC ligand exchange process and its specific effects in the context of time-resolved optical spectroscopy has been discussed at length elsewhere,<sup>11, 13-16, 19-21</sup> a subtle spectral feature is noteworthy here. In all four discrete materials investigated, a red shift of the TPn absorption bands was consistently observed, often accompanied by a blue shift of the PbS first exciton band. TEM images taken after ligand exchange (Figure S2.3) showed no change in PbS NC average particle size. In the PbS-805 hybrid materials, spectral congestion from the energetic similarity between the PbS first exciton absorbance band and the TPn absorbance band prohibits definitive assignment of the concomitant PbS absorption blue shift. These shifts are reminiscent of NC-molecule electronic wavefunction interactions that occur in strongly quantum-confined materials.<sup>13, 28</sup>

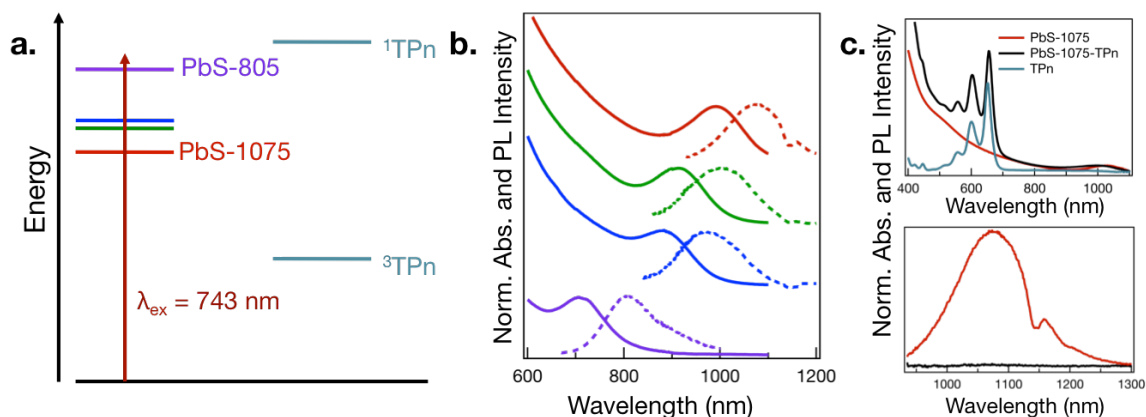


**Figure 2.1** (a) Illustration of PbS nanocrystal first exciton and TPn-centered energy levels. (b) Electronic absorption (solid lines) and emission spectra (dashed lines) for PbS NCs ranging in diameter from  $3.3 \pm 0.6 \text{ nm}$  (top, red) to  $2.2 \pm 0.3 \text{ nm}$  (bottom, violet). (c) Electronic absorption spectra (top) in toluene of PbS-1075 nanocrystals before and after ligand exchange by TPn with free TPn shown, and photoluminescence spectra in toluene (bottom) of PbS-1075 and PbS-1075-TPn. The depression in the photoluminescence near 1150 nm results from toluene absorption.

TA spectroscopy was utilized to interrogate the excited state dynamics occurring in the oleate-capped PbS NCs. Figure 2.2a displays time dependent TA difference spectra for PbS-805 suspended in toluene using a visible light probe (430-780 nm) following 743 nm pulsed laser excitation (0.15  $\mu$ J/pulse, 100 fs fwhm, 0.8 excitations/NC). This excitation wavelength was chosen because it is absorbed by all four NC species but not by TPn, therefore allowing all hybrid materials to achieve selective PbS excitation at a single wavelength. Pumping a solution of TPn without any PbS NCs at 743 nm results in no discernible TA signals (Figure S2.4), indicating that the PbS NCs are selectively excited at this wavelength. Visible and near-IR (830-1380 nm) TA difference spectra for solutions of PbS-1075, PbS-1000, PbS-970, PbS-805 following 743 nm pulsed laser excitation are presented in Figure S2.5, All four PbS species display a prompt, characteristic negative polarity absorption feature, associated with bleaching of their first exciton absorption band. PbS-805 is instructive to illustrate the general excited-state spectral signatures of PbS NCs. This is because the negative polarity TA signal for the PbS-805 first exciton bleach appears within the same visible region of the electromagnetic spectrum as the other notable PbS-TPn excited state features. These PbS-TPn features consist of the broad induced absorption band characteristic of interband transitions in the excited PbS NCs<sup>29-32</sup> and some notable TPn transient spectral features. Over the maximum probe delay of the ultrafast TA measurements (6.2 ns), all four PbS TA difference spectra remain mostly unchanged. Nanosecond TA experiments (Figures S2.6, S2.7) feature symmetric decay of PbS excited state spectral features on a 1-2  $\mu$ s time scale. These results are consistent with extant knowledge of the excited state dynamics of carboxylate-capped PbS NCs.<sup>13, 15, 16, 32-45</sup>

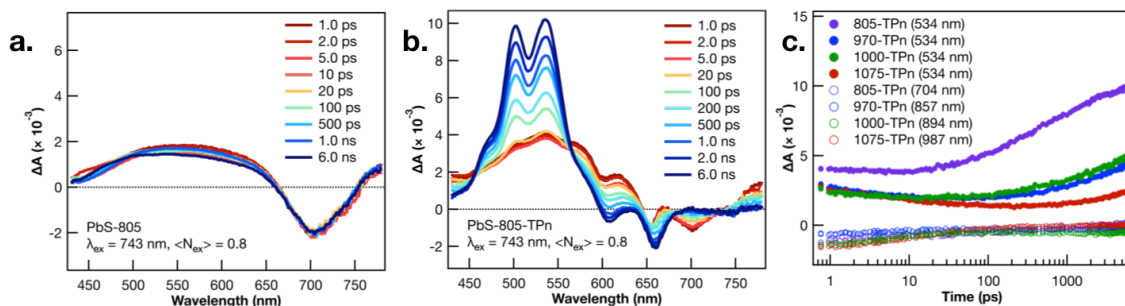


**Figure 2.2** Ultrafast TA difference spectra of PbS-805 (a) and PbS-805-TPn (b) suspensions in toluene following 743 nm pulsed laser excitation (0.15  $\mu\text{J}/\text{pulse}$ , 100 fs fwhm). Time delays range from 1.0 ps (red) to 6.0 ns (blue). Ultrafast TA kinetics (c) probed at 534 nm (closed circles) and different PbS first exciton bleach wavelengths (open circles) for PbS-805-TPn (purple), PbS-970-TPn (blue), PbS-1000-TPn (green), and PbS-1075-TPn (red) suspensions in toluene following 743 nm pulsed laser excitation (0.15  $\mu\text{J}/\text{pulse}$ , 100 fs fwhm).

Following PbS NC surface functionalization with TPn molecules, the TA difference spectra and kinetics following selective excitation of the NCs are changed significantly (Figures 2.2b and S2.8). Upon pulsed laser excitation at 743 nm, the initially formed excited state resembles the excited state of the oleate-capped PbS NCs with the added presence of three negative absorption features at 550, 600, and 650 nm superimposed on the broad PbS excited state. The location of the negative features implies a relationship to the ground state absorption spectrum of TPn. These negative features have been previously assigned<sup>13</sup> and independently reproduced in a closely related study<sup>16</sup> as a transient dipole-induced shift of the  $S_0$  to  $S_1$  electronic transitions in TPn.<sup>46-50</sup> In PbS-1075-TPn, the material most analogous to those studied previously,<sup>13, 16</sup> the first exciton absorption band bleach disappears over the first 250 ps after excitation. Concomitantly, the broad PbS excited state absorbance was observed to symmetrically attenuate. This was followed by the growth of a band centered at 530 nm, previously assigned to the PbS-bound molecular triplet  $^3\text{TPn}$ .<sup>13, 16</sup> The molecular triplet develops with a time constant of roughly 8 ns, in stark contrast to the ps-regime decays of the

spectral features associated with the PbS NC excited state, but in universal agreement with previous related studies.<sup>13, 16</sup> The assignments and temporal ordering of the time-resolved spectral features for all PbS NC hybrid materials, regardless of size, are consistent with the same mechanism. This mechanism consists of a decay of the PbS NC excited state on ps time scales to a kinetic intermediate<sup>13, 16</sup> followed by a nanosecond time scale growth of the TPn excited triplet state.

In all four TPn-modified materials, the time constants for the observed decay of the NIR bleach features were coterminous with the decays of the broad visible absorption features (Table S2.1). PbS-805-TPn (Figure S2.8a) is of particular interest to this study because the first exciton bleach is now contained in the region probed by the same visible white light generating crystal. This enables comparison of the dominant <sup>3</sup>TPn signal at 534 nm with the PbS NC first exciton bleach at 710 nm. Furthermore, the shift of the bleach wavelength decongests the NIR white light continuum for observation of the <sup>3</sup>TPn signal at 994 nm and a characteristic TPn<sup>++</sup> signal expected near 876 nm.<sup>21</sup> The <sup>3</sup>TPn signal at 994 nm appears in TA difference spectra for PbS-1000-TPn, PbS-970-TPn, and PbS-805-TPn following 743 nm pulsed laser excitation on time scales matching the growth of the <sup>3</sup>TPn feature around 530 nm (Figures S2.8b, S2.8d, S2.8f). However, the TPn<sup>++</sup> signal expected near 876 nm is not observed in PbS-1000-TPn or PbS-970-TPn at any time point. There is a feature observed at 876 nm in PbS-805-TPn on the same time scale as the <sup>3</sup>TPn features at 530 nm and 994 nm. This kinetic behaviour is indicative that the TPn<sup>++</sup> formed is unlikely to be acting as the primary kinetic intermediate to <sup>3</sup>TPn formation. The decay rates of the characteristic PbS NC excited state features all increased with increasing PbS NC first exciton energy, as did the growth rates of <sup>3</sup>TPn

(Figure 2.2c). The TA difference spectra and kinetics for the PbS-TPn materials on supra-nanosecond time scales (Figures S2.9, S2.10) illustrate symmetric decay of the NC-appended  $^3\text{TPn}$  spectral features on microsecond time scales (Table S2.2). The time constants associated with this excited state relaxation process approach the time constant for the relaxation of freely diffusing  $^3\text{TPn}$  as the PbS NCs decrease in diameter.<sup>13</sup> The observed trend in  $^3\text{TPn}$  lifetime as a function of PbS NC size is consistent with a concentration effect<sup>15</sup> induced by the greater number of TPn molecules that can be accommodated by the larger NCs. Temperature-dependent decay kinetics of the  $^3\text{TPn}$  TA signals (Figure S2.11) indicate the reduction in lifetime is unlikely to be a thermally activated excited state process, as previously observed in other NC-molecule materials featuring reverse triplet-triplet energy transfer.<sup>19, 20</sup> The lack of experimental evidence supporting any reverse TTET occurring at these interfaces remains inconsistent with a concerted Dexter-like process.

In the interest of assigning consistent rate constants to the three excited state processes occurring in each material, we used a spectral decomposition model<sup>23</sup> (*vide supra*) to fit the time-resolved TA difference spectra. The three decay-associated difference spectra (DADS) fit to the model of the PbS-1075-TPn data collected over the first 6.2 ns after pulsed 743 nm excitation are displayed in Figure 2.3a. The first DADS (dark red) is reminiscent of the spectrum observed immediately upon selective excitation of the PbS NC. Specifically, it contains a PbS first exciton bleach in the NIR combined with a broadband PbS induced absorption in the visible with the three negative absorption features from the transient dipole-induced TPn absorption shift. Meanwhile, the third DADS (Figure 2.3a, pink) is a strong match to the spectrum of the PbS-appended  $^3\text{TPn}$

species from the final ultrafast TA time delay and the prompt nanosecond TA difference spectra (Figures S2.8g, S2.8h, and S2.9d). The first DADS evolves into the second DADS (Figure 2.3a, red) with a time constant of 12.6 ps. Subsequently, the second DADS evolves into the third with a time constant of 8.0 ns. Both time constants are in good agreement with single-wavelength kinetic analyses of the experimental data and previously published results.<sup>13, 16</sup> Consistent with the single wavelength kinetic analyses, three sequential DADS model the TA difference spectra in every PbS-TPn species investigated here. The sub-microsecond time constants for the PbS-TPn materials extracted from the model are summarized in Table S2.3. The final step to obtain consistent rate constants for the two sub-microsecond excited state processes was to average the rate constants on an average TPn per PbS NC basis, which are also included in Table S2.3.

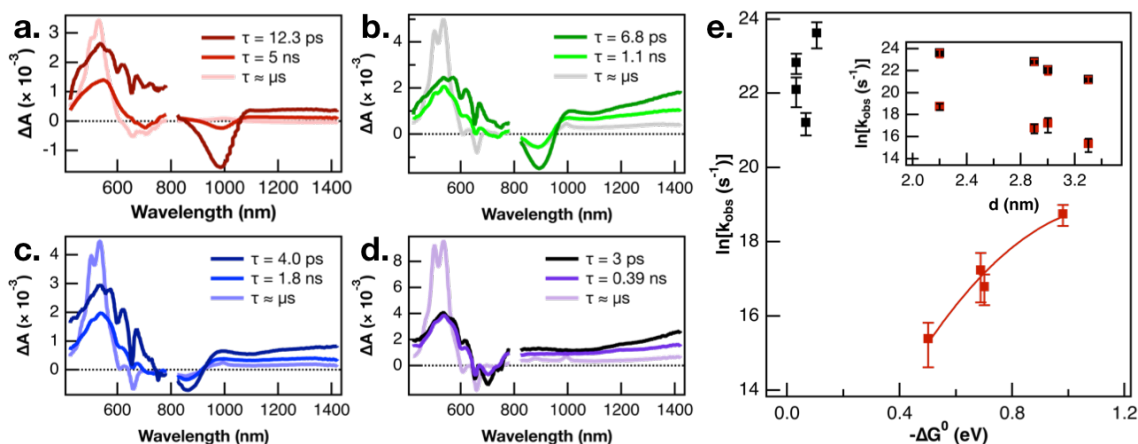


**Figure 2.3** Basis spectra modeled on TA spectra of (a) PbS-1075-TPn, (b) PbS-1000-TPn, (c) PbS-970-TPn, and (d) PbS-805-TPn materials. The ultrafast TA spectra initially resemble the 1st (darkest hues) spectra and eventually come to resemble the 3rd spectra (palest hues) by the end of the 6.2 ns delay stage. The 2nd spectra (intermediate hues) are necessary to accurately model the experimental data. Data from 425 to 775 nm and data from 825 to 1325 nm were fit with matching rate constants. Logarithm of extracted rate constants plotted as a function of thermodynamic driving force (e) and approximate PbS NC diameter (e, inset). Bars in (e) and (e, inset) reflect the standard error calculated from three independent measurements. The solid red line in (e) is a Marcus theory fit to the data intended as a phenomenological guide for the eye.

Recent work on CuInS<sub>2</sub> NCs has magnified the existence of charge-carrier trapping phenomena in semiconductor NCs, specifically with respect to energy transfer across the NC-molecule interface.<sup>51</sup> In the related PbS-acene study by Bender, Raulerson *et al.*, electronic structure calculations provide a rationale for the existence of surface-localized excited states on the PbS NC.<sup>16</sup> A direct comparison of the triplet sensitization of two different acene molecules by CsPbBr<sub>3</sub> NCs suggested that electrons and holes could possess vastly different trapping kinetics.<sup>52</sup> The calculated PbS NC surface states were previously tentatively assigned to hole-trapping phenomena at the NC surface.<sup>16</sup> A plausible next step toward validating that mechanistic assignment would be to study the NC size-dependence of triplet-triplet energy transfer from multiple sizes of PbS NC to pentacene. This is the first such PbS NC to acene triplet-triplet energy transfer NC-size-dependence study to employ either NC-selective excitation or a pentacene derivative as the acceptor. If the kinetic intermediate, which is observed comprehensively across all PbS NC sizes investigated, is a surface hole-trapping phenomenon, that could explain the absence of TPn<sup>++</sup> TA signals discussed earlier. Furthermore, we propose this mechanism provides a suitable explanation for the size-dependent behaviour of the <sup>3</sup>TPn TA signal growth rates displayed in Figure 2.3e. The rate constants for formation of the <sup>3</sup>TPn state increase with increasing PbS conduction band position, featuring a parabolic Marcus free energy dependence in the normal region. As mentioned previously, the rate constants on the vertical axis in Figure 2.3e have been adjusted to reflect the differing surface concentrations of TPn on the different sizes of the PbS NC. However, they do not account for any changes in NC-TPn electronic coupling as a function of PbS NC size. Taking these factors into account, the fit applied to the data herein was intended primarily

as a phenomenological guide to the eye. However, the values extracted from the fit in this study are broadly consistent with recently reported data from a PbS QD and tetracene study which also employed a fit to Marcus theory.<sup>53</sup> Meanwhile, the rate constants associated with the attenuation of the initial PbS NC excited state are not well-predicted by Marcus theory. As shown in the inset of Figure 2.3e, the PbS NC size-dependence of the rate constants for decay of the PbS excited state appears to be directly related to the NC diameter. We suggest the rate constants for this first step deviate from Marcus theory in part because they are intrinsic to the PbS NCs or otherwise independent from the energetics of TPn. The combination of the current size and band gap kinetic dependence data, the recent work on charge carrier trapping,<sup>51, 52</sup> and the theoretical evidence for surface state mediation,<sup>16</sup> supports a hole-trapping mechanism for <sup>3</sup>TPn generation from excited PbS NCs. On picosecond time scales, surface state trapping of photogenerated holes quenches the PbS band edge exciton, while <sup>3</sup>TPn is directly generated from the hole-trapped PbS NC much more slowly.

## 2.5 Conclusions

We have functionalized a series of PbS NCs with TPn, a derivative of TIPS-pentacene, to generate a suite of hybrid inorganic-organic nanomaterials. We have investigated these nanomaterials from sub-picosecond to supra-nanosecond time scales using transient absorption spectroscopy in the visible and near-IR portions of the electromagnetic spectrum. Selective photoexcitation of PbS NCs produces a kinetic intermediate over picosecond time scales, which decays to yield TPn-localized triplet excitons on nanosecond time scales. This stepwise triplet sensitization process is comprehensive across all PbS NC sizes and band-edge exciton energies investigated. The

evidence is demonstrative of stepwise (indirect) sensitization and inconsistent with a concerted Dexter-like process. This work demonstrates the inherent complexity in the interactions between direct energy transfer processes, semiconductor trap states, and stepwise electron transfers. Understanding these interactions is fundamental to successfully govern directional triplet energy transfer or sensitization from semiconductor NCs to surface-appended molecules.

## **2.6 Acknowledgments**

We acknowledge support for this work from the Organic Materials Chemistry program in the Air Force Office of Scientific Research (FA9550-18-1-0331). Electron microscopy was performed at the Analytical Instrumentation Facility (AIF) at North Carolina State University, which is supported by the State of North Carolina and the National Science Foundation (Award Number ECCS-1542015). The AIF is a member of the North Carolina Research Triangle Nanotechnology Network (RTNN), a site in the National Nanotechnology Coordinated Infrastructure (NNCI). Dr. Sofia Garakyaraghi assisted with the collection of the ultrafast TA data. Dr. Devin B. Granger synthesized the TPn used in this study under the supervision of Prof. John E. Anthony.

## 2.7 References

1. Huang, Z.; Lee Tang, M., Semiconductor Nanocrystal Light Absorbers for Photon Upconversion. *The Journal of Physical Chemistry Letters* **2018**, *9* (21), 6198-6206.
2. Garakyaraghi, S.; Castellano, F. N., Nanocrystals for Triplet Sensitization: Molecular Behavior from Quantum-Confined Materials. *Inorganic Chemistry* **2018**, *57* (5), 2351-2359.
3. Lu, H.; Carroll, G. M.; Neale, N. R.; Beard, M. C., Infrared Quantum Dots: Progress, Challenges, and Opportunities. *ACS Nano* **2019**.
4. Turro, N. J., *Modern Molecular Photochemistry*. 1991.
5. Olaya-Castro, A.; Scholes, G. D., Energy transfer from Förster–Dexter theory to quantum coherent light-harvesting. *International Reviews in Physical Chemistry* **2011**, *30* (1), 49-77.
6. Scholes, G. D., Controlling the optical properties of inorganic nanoparticles. *Advanced Functional Materials* **2008**, *18* (8), 1157-1172.
7. Smith, M. B.; Michl, J., Singlet Fission. *Chemical Reviews* **2010**, *110* (11), 6891-6936.
8. Smith, M. B.; Michl, J., Recent Advances in Singlet Fission. In *Annual Review of Physical Chemistry, Vol 64*, Johnson, M. A.; Martinez, T. J., Eds. Annual Reviews: Palo Alto, 2013; Vol. 64, pp 361-386.
9. Tabachnyk, M.; Ehrler, B.; Gelin, S.; Boehm, M. L.; Walker, B. J.; Musselman, K. P.; Greenham, N. C.; Friend, R. H.; Rao, A., Resonant energy transfer of triplet excitons from pentacene to PbSe nanocrystals. *Nature Materials* **2014**, *13* (11), 1033-1038.
10. Thompson, N. J.; Wilson, M. W. B.; Congreve, D. N.; Brown, P. R.; Scherer, J. M.; Bischof, T. S.; Wu, M.; Geva, N.; Welborn, M.; Van Voorhis, T.; Bulovic, V.; Bawendi, M. G.; Baldo, M. A., Energy harvesting of non-emissive triplet excitons in tetracene by emissive PbS nanocrystals. *Nature Materials* **2014**, *13* (11), 1039-1043.
11. Mongin, C.; Garakyaraghi, S.; Razgoniaeva, N.; Zamkov, M.; Castellano, F. N., Direct observation of triplet energy transfer from semiconductor nanocrystals. *Science* **2016**, *351* (6271), 369-372.
12. Dexter, D. L., A THEORY OF SENSITIZED LUMINESCENCE IN SOLIDS. *Journal of Chemical Physics* **1953**, *21* (5), 836-850.
13. Garakyaraghi, S.; Mongin, C.; Granger, D. B.; Anthony, J. E.; Castellano, F. N., Delayed Molecular Triplet Generation from Energized Lead Sulfide Quantum Dots. *Journal of Physical Chemistry Letters* **2017**, *8* (7), 1458-1463.
14. Huang, Z.; Xu, Z.; Mahboub, M.; Li, X.; Taylor, J. W.; Harman, W. H.; Lian, T.; Tang, M. L., PbS/CdS Core-Shell Quantum Dots Suppress Charge Transfer and Enhance Triplet Transfer. *Angewandte Chemie-International Edition* **2017**, *56* (52), 16583-16587.
15. Kroupa, D. M.; Arias, D. H.; Blackburn, J. L.; Carroll, G. M.; Granger, D. B.; Anthony, J. E.; Beard, M. C.; Johnson, J. C., Control of Energy Flow Dynamics between Tetracene Ligands and PbS Quantum Dots by Size Tuning and Ligand Coverage. *Nano Letters* **2018**, *18* (2), 865-873.

16. Bender, J. A.; Raulerson, E. K.; Li, X.; Goldzak, T.; Xia, P.; Van Voorhis, T.; Tang, M. L.; Roberts, S. T., Surface States Mediate Triplet Energy Transfer in Nanocrystal-Acene Composite Systems. *Journal of the American Chemical Society* **2018**, *140* (24), 7543-7553.
17. Hines, M. A.; Scholes, G. D., Colloidal PbS nanocrystals with size-tunable near-infrared emission: Observation of post-synthesis self-narrowing of the particle size distribution. *Advanced Materials* **2003**, *15* (21), 1844-1849.
18. Li, Z.; Shankar, K.; Mor, G. K.; Grimminger, R. A.; Lin, C.-M.; Anthony, J. E.; Grimes, C. A., Functionalized pentacenes for dye-sensitized solar cells. *Journal of Photonics for Energy* **2011**, *1*.
19. Mongin, C.; Moroz, P.; Zamkov, M.; Castellano, F. N., Thermally activated delayed photoluminescence from pyrenyl-functionalized CdSe quantum dots. *Nature Chemistry* **2018**, *10* (2), 225-230.
20. La Rosa, M.; Denisov, S. A.; Jonusauskas, G.; McClenaghan, N. D.; Credi, A., Designed Long-Lived Emission from CdSe Quantum Dots through Reversible Electronic Energy Transfer with a Surface-Bound Chromophore. *Angewandte Chemie-International Edition* **2018**, *57* (12), 3104-3107.
21. Lu, H. P.; Chen, X. H.; Anthony, J. E.; Johnson, J. C.; Beard, M. C., Sensitizing Singlet Fission with Perovskite Nanocrystals. *Journal of the American Chemical Society* **2019**, *141* (12), 4919-4927.
22. Garakyaraghi, S.; Danilov, E. O.; McCusker, C. E.; Castellano, F. N., Transient Absorption Dynamics of Sterically Congested Cu(I) MLCT Excited States. *Journal of Physical Chemistry A* **2015**, *119* (13), 3181-3193.
23. van Wilderen, L. J. G. W.; Lincoln, C. N.; van Thor, J. J., Modelling Multi-Pulse Population Dynamics from Ultrafast Spectroscopy. *PLOS ONE* **2011**, *6* (3), e17373.
24. Kambhampati, P., Unraveling the the Structure and Dynamics of Excitons in Semiconductor Quantum Dots. *Accounts of Chemical Research* **2011**, *44* (1), 1-13.
25. Turner, D. B.; Hassan, Y.; Scholes, G. D., Exciton Superposition States in CdSe Nanocrystals Measured Using Broadband Two-Dimensional Electronic Spectroscopy. *Nano Letters* **2012**, *12* (2), 880-886.
26. Schnitzenbaumer, K. J.; Labrador, T.; Dukovic, G., Impact of Chalcogenide Ligands on Excited State Dynamics in CdSe Quantum Dots. *Journal of Physical Chemistry C* **2015**, *119* (23), 13314-13324.
27. Azzaro, M. S.; Babin, M. C.; Stauffer, S. K.; Henkelman, G.; Roberts, S. T., Can Exciton-Delocalizing Ligands Facilitate Hot Hole Transfer from Semiconductor Nanocrystals? *Journal of Physical Chemistry C* **2016**, *120* (49), 28224-28234.
28. Zhu, H.; Yang, Y.; Hyeon-Deuk, K.; Califano, M.; Song, N.; Wang, Y.; Zhang, W.; Prezhdo, O. V.; Lian, T., Auger-Assisted Electron Transfer from Photoexcited Semiconductor Quantum Dots. *Nano Letters* **2014**, *14* (3), 1263-1269.
29. Kambhampati, P., On the kinetics and thermodynamics of excitons at the surface of semiconductor nanocrystals: Are there surface excitons? *Chemical Physics* **2015**, *446*, 92-107.

30. Klimov, V. I., Spectral and dynamical properties of multiexcitons in semiconductor nanocrystals. In *Annual Review of Physical Chemistry*, 2007; Vol. 58, pp 635-673.
31. Cho, B.; Peters, W. K.; Hill, R. J.; Courtney, T. L.; Jonas, D. M., Bulklike Hot Carrier Dynamics in Lead Sulfide Quantum Dots. *Nano Letters* **2010**, *10* (7), 2498-2505.
32. Yang, Y.; Rodriguez-Cordoba, W.; Lian, T., Ultrafast Charge Separation and Recombination Dynamics in Lead Sulfide Quantum Dot-Methylene Blue Complexes Probed by Electron and Hole Intraband Transitions. *Journal of the American Chemical Society* **2011**, *133* (24), 9246-9249.
33. Du, H.; Chen, C. L.; Krishnan, R.; Krauss, T. D.; Harbold, J. M.; Wise, F. W.; Thomas, M. G.; Silcox, J., Optical properties of colloidal PbSe nanocrystals. *Nano Letters* **2002**, *2* (11), 1321-1324.
34. Wehrenberg, B. L.; Wang, C. J.; Guyot-Sionnest, P., Interband and intraband optical studies of PbSe colloidal quantum dots. *Journal of Physical Chemistry B* **2002**, *106* (41), 10634-10640.
35. Warner, J. H.; Thomsen, E.; Watt, A. R.; Heckenberg, N. R.; Rubinsztein-Dunlop, H., Time-resolved photoluminescence spectroscopy of ligand-capped PbS nanocrystals. *Nanotechnology* **2005**, *16* (2), 175-179.
36. Clark, S. W.; Harbold, J. M.; Wise, F. W., Resonant energy transfer in PbS quantum dots. *Journal of Physical Chemistry C* **2007**, *111* (20), 7302-7305.
37. Chen, Y.; Yu, D.; Li, B.; Chen, X.; Dong, Y.; Zhang, M., Size-dependent radiative emission of PbS quantum dots embedded in Nafion membrane. *Applied Physics B-Lasers and Optics* **2009**, *95* (1), 173-177.
38. Gaponenko, M. S.; Lutich, A. A.; Tolstik, N. A.; Onushchenko, A. A.; Malyarevich, A. M.; Petrov, E. P.; Yumashev, K. V., Temperature-dependent photoluminescence of PbS quantum dots in glass: Evidence of exciton state splitting and carrier trapping. *Physical Review B* **2010**, *82* (12).
39. Knowles, K. E.; Malicki, M.; Weiss, E. A., Dual-Time Scale Photoinduced Electron Transfer from PbS Quantum Dots to a Molecular Acceptor. *Journal of the American Chemical Society* **2012**, *134* (30), 12470-12473.
40. Yang, Y.; Rodriguez-Cordoba, W.; Lian, T., Multiple Exciton Generation and Dissociation in PbS Quantum Dot-Electron Acceptor Complexes. *Nano Letters* **2012**, *12* (8), 4235-4241.
41. Yang, Y.; Rodriguez-Cordoba, W.; Xiang, X.; Lian, T., Strong Electronic Coupling and Ultrafast Electron Transfer between PbS Quantum Dots and TiO<sub>2</sub> Nanocrystalline Films. *Nano Letters* **2012**, *12* (1), 303-309.
42. Yang, Y.; Lian, T., Multiple exciton dissociation and hot electron extraction by ultrafast interfacial electron transfer from PbS QDs. *Coordination Chemistry Reviews* **2014**, *263*, 229-238.
43. Aruda, K. O.; Kunz, M. B.; Tagliazucchi, M.; Weiss, E. A., Temperature-Dependent Permeability of the Ligand Shell of PbS Quantum Dots Probed by Electron Transfer to Benzoquinone. *Journal of Physical Chemistry Letters* **2015**, *6* (14), 2841-2846.

44. Chung, H.; Choi, H.; Kim, D.; Jeong, S.; Kim, J., Size Dependence of Excitation-Energy-Related Surface Trapping Dynamics in PbS Quantum Dots. *Journal of Physical Chemistry C* **2015**, *119* (13), 7517-7524.
45. Wu, M.; Congreve, D. N.; Wilson, M. W. B.; Jean, J.; Geva, N.; Welborn, M.; Van Voorhis, T.; Bulovic, V.; Bawendi, M. G.; Baldo, M. A., Solid-state infrared-to-visible upconversion sensitized by colloidal nanocrystals. *Nature Photonics* **2016**, *10* (1), 31-34.
46. Sebastian, L.; Weiser, G.; Bassler, H., CHARGE-TRANSFER TRANSITIONS IN SOLID TETRACENE AND PENTACENE STUDIED BY ELECTRO-ABSORPTION. *Chemical Physics* **1981**, *61* (1-2), 125-135.
47. Norris, D. J.; Sacra, A.; Murray, C. B.; Bawendi, M. G., MEASUREMENT OF THE SIZE-DEPENDENT HOLE SPECTRUM IN CDSE QUANTUM DOTS. *Physical Review Letters* **1994**, *72* (16), 2612-2615.
48. Bublitz, G. U.; Boxer, S. G., Stark spectroscopy: Applications in chemistry, biology, and materials science. *Annual Review of Physical Chemistry* **1997**, *48*, 213-242.
49. Ardo, S.; Sun, Y.; Castellano, F. N.; Meyer, G. J., Excited-State Electron Transfer from Ruthenium-Polypyridyl Compounds to Anatase TiO<sub>2</sub> Nanocrystallites Evidence for a Stark Effect. *Journal of Physical Chemistry B* **2010**, *114* (45), 14596-14604.
50. Gelinas, S.; Rao, A.; Kumar, A.; Smith, S. L.; Chin, A. W.; Clark, J.; van der Poll, T. S.; Bazan, G. C.; Friend, R. H., Ultrafast Long-Range Charge Separation in Organic Semiconductor Photovoltaic Diodes. *Science* **2014**, *343* (6170), 512-516.
51. Han, Y.; He, S.; Luo, X.; Li, Y.; Chen, Z.; Kang, W.; Wang, X.; Wu, K., Triplet Sensitization by "Self-Trapped" Excitons of Nontoxic CuInS<sub>2</sub> Nanocrystals for Efficient Photon Upconversion. *Journal of the American Chemical Society* **2019**, *141* (33), 13033-13037.
52. Luo, X.; Han, Y. Y.; Chen, Z. W.; Li, Y. L.; Liang, G. J.; Liu, X.; Ding, T.; Nie, C. M.; Wang, M.; Castellano, F. N.; Wu, K. F., Mechanisms of triplet energy transfer across the inorganic nanocrystal/organic molecule interface. *Nature Communications* **2020**, *11* (1).
53. Gray, V.; Allardice, J. R.; Zhang, Z.; Dowland, S.; Xiao, J.; Petty, A. J.; Anthony, J. E.; Greenham, N. C.; Rao, A., Direct vs Delayed Triplet Energy Transfer from Organic Semiconductors to Quantum Dots and Implications for Luminescent Harvesting of Triplet Excitons. *ACS Nano* **2020**, *14* (4), 4224-4234.

## 2.8 Supplementary Information

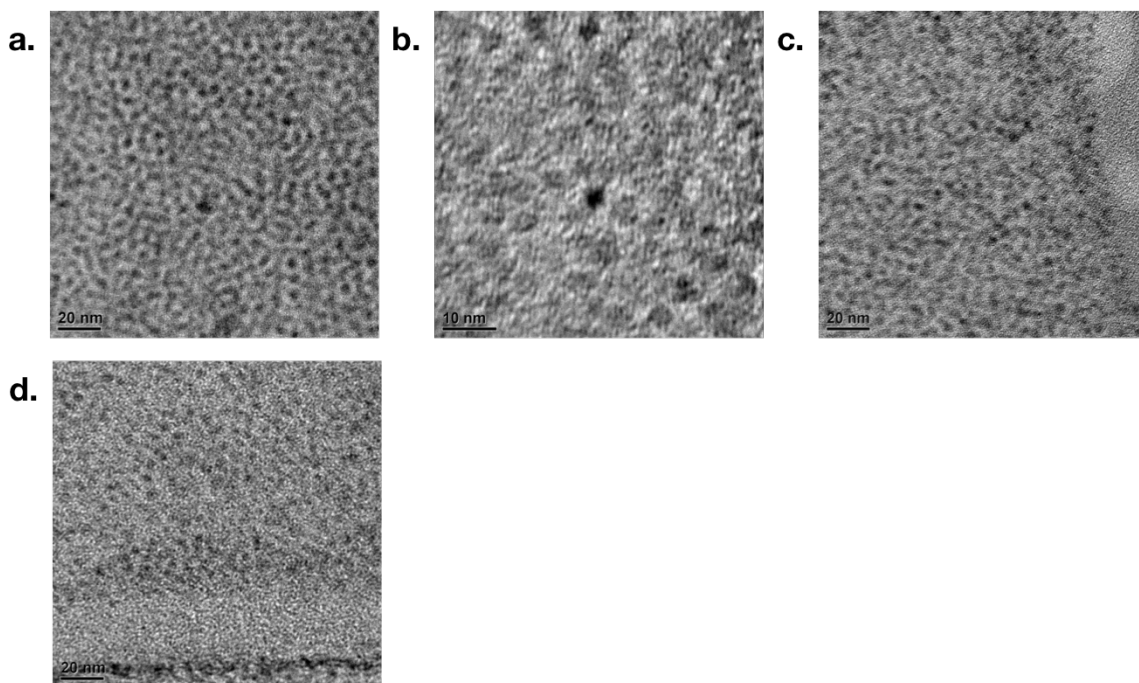


**Figure S2.1** TEM images of PbS NCs with average diameters of **(a)**  $3.3 \pm 0.6$  nm, **(b)**  $3.0 \pm 0.5$  nm, **(c)**  $2.9 \pm 0.5$  nm, and **(d)**  $2.2 \pm 0.3$  nm.

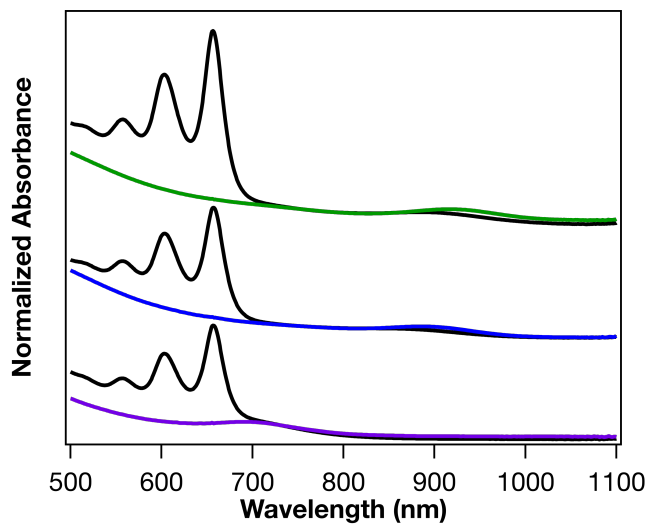


**Figure S2.2** Electronic absorption spectra of PbS-1000 (red), PbS-970 (green), PbS-805 (purple) with their corresponding PbS-TPn hybrid materials (black lines, matching y-axis offset indicates matching NC size).

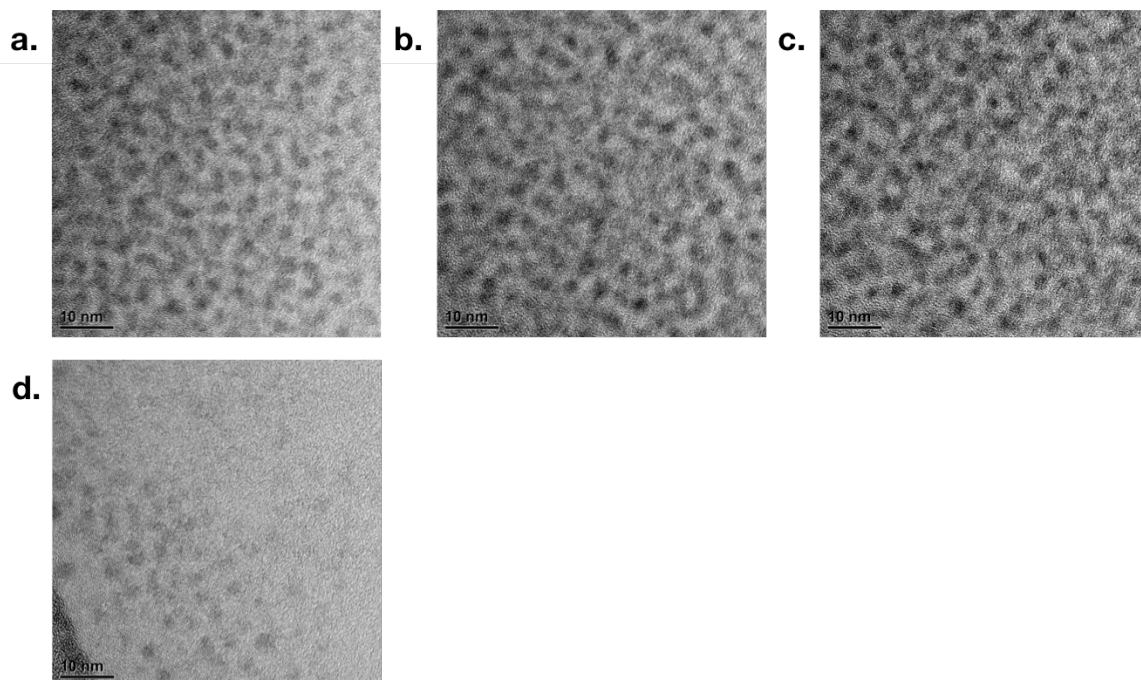


**Figure S2.3** TEM images of (a) PbS-1075-TPn, (b) PbS-1000-TPn, (c) PbS-970-TPn, (d) PbS-805-TPn.

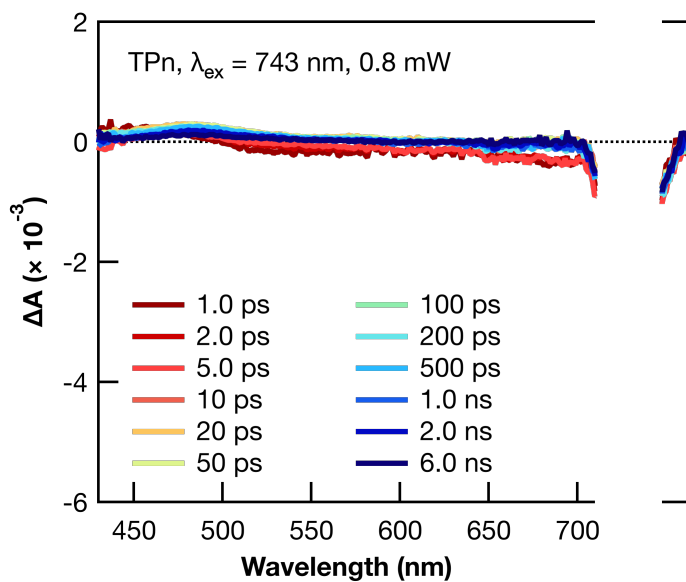


**Figure S2.4** Ultrafast TA difference spectra of a solution of TPn in toluene following 743 nm pulsed laser excitation (0.80  $\mu\text{J}/\text{pulse}$ , 100 fs fwhm). The non-time-resolved spectral feature centered around 743 nm is scattered excitation.

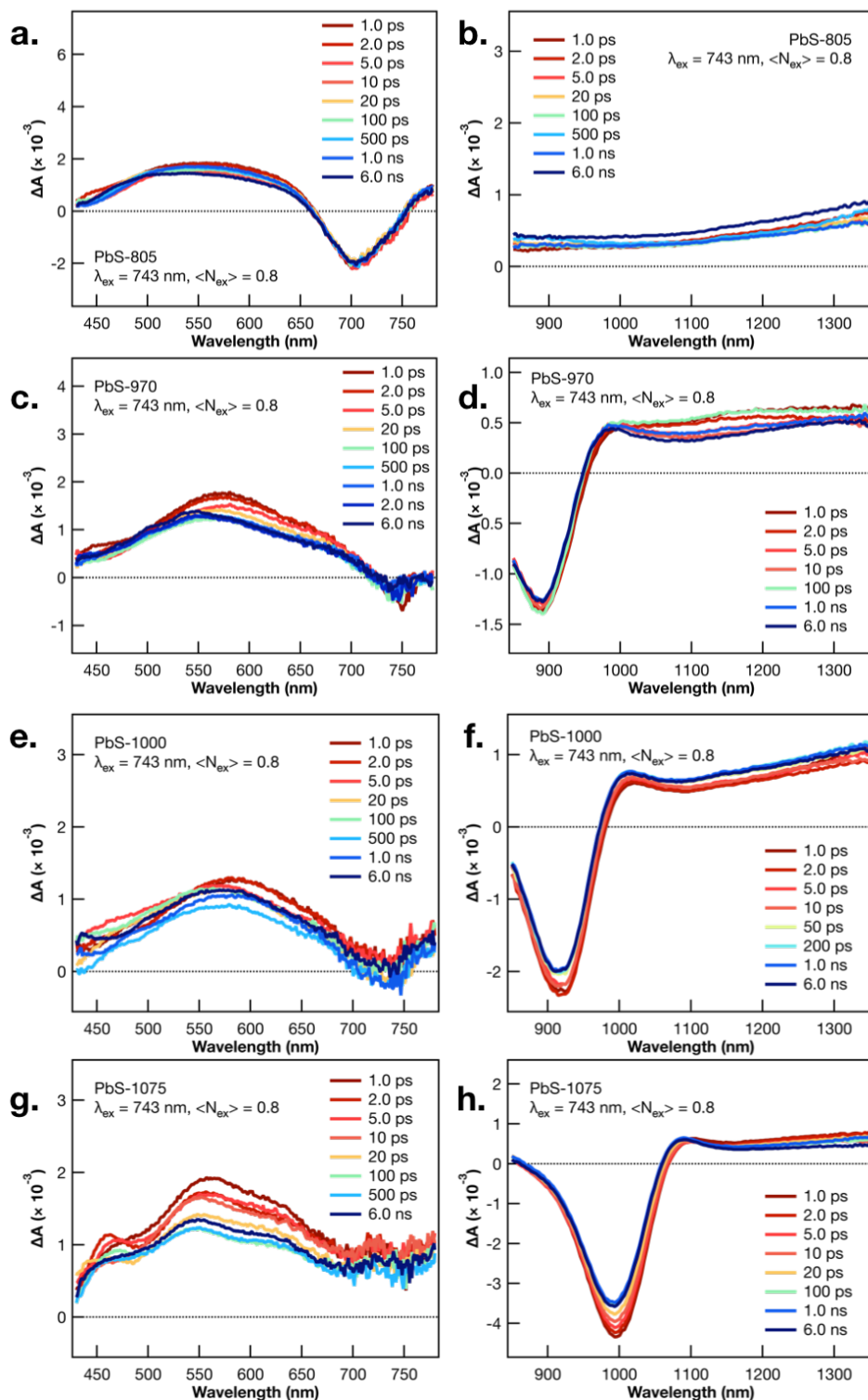


**Figure S2.5** Ultrafast TA difference spectra of PbS nanocrystal suspensions in toluene following 743 nm pulsed laser excitation (0.15  $\mu\text{J}/\text{pulse}$ , 100 fs fwhm). The spectra correspond to PbS-805 in the (a) visible and (b) near-IR spectral regions, PbS-970 in the (c) visible and (d) NIR, PbS-1000 in the (e) visible and (f) NIR, and PbS-1075 in the (g) visible and (h) NIR. Time delays range from 1.0 ps (red) to 6.0 ns (blue).

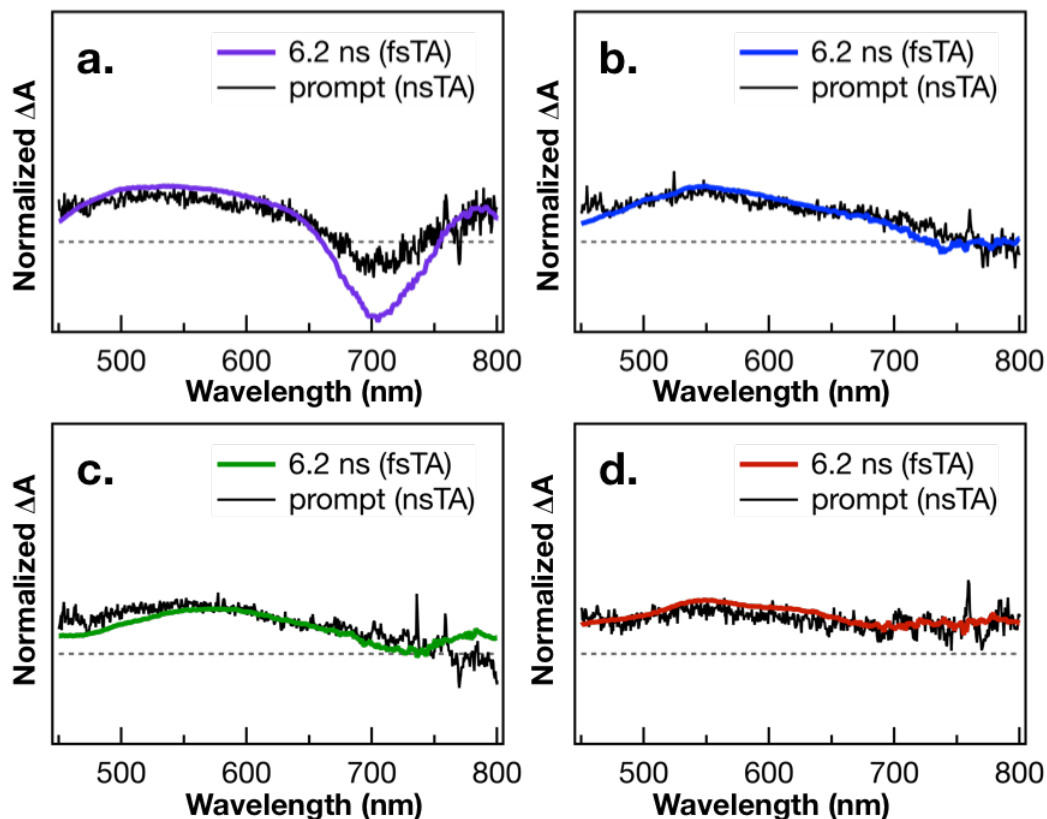


**Figure S2.6** Comparison of normalized, ultrafast (0.15  $\mu\text{J}/\text{pulse}$ , 100 fs fwhm, 743 nm) TA difference spectra (colored) and normalized, nanosecond (1.0 mJ/pulse, 5 ns fwhm, 743 nm) TA difference spectra (black) of PbS nanocrystal suspensions in toluene following pulsed laser excitation. The spectra correspond to **(a)** PbS-805, **(b)** PbS-970, **(c)** PbS-1000, and **(d)** PbS-1075. Time delays are prompt for the nanosecond TA spectra and 6.2 ns for the ultrafast TA spectra.

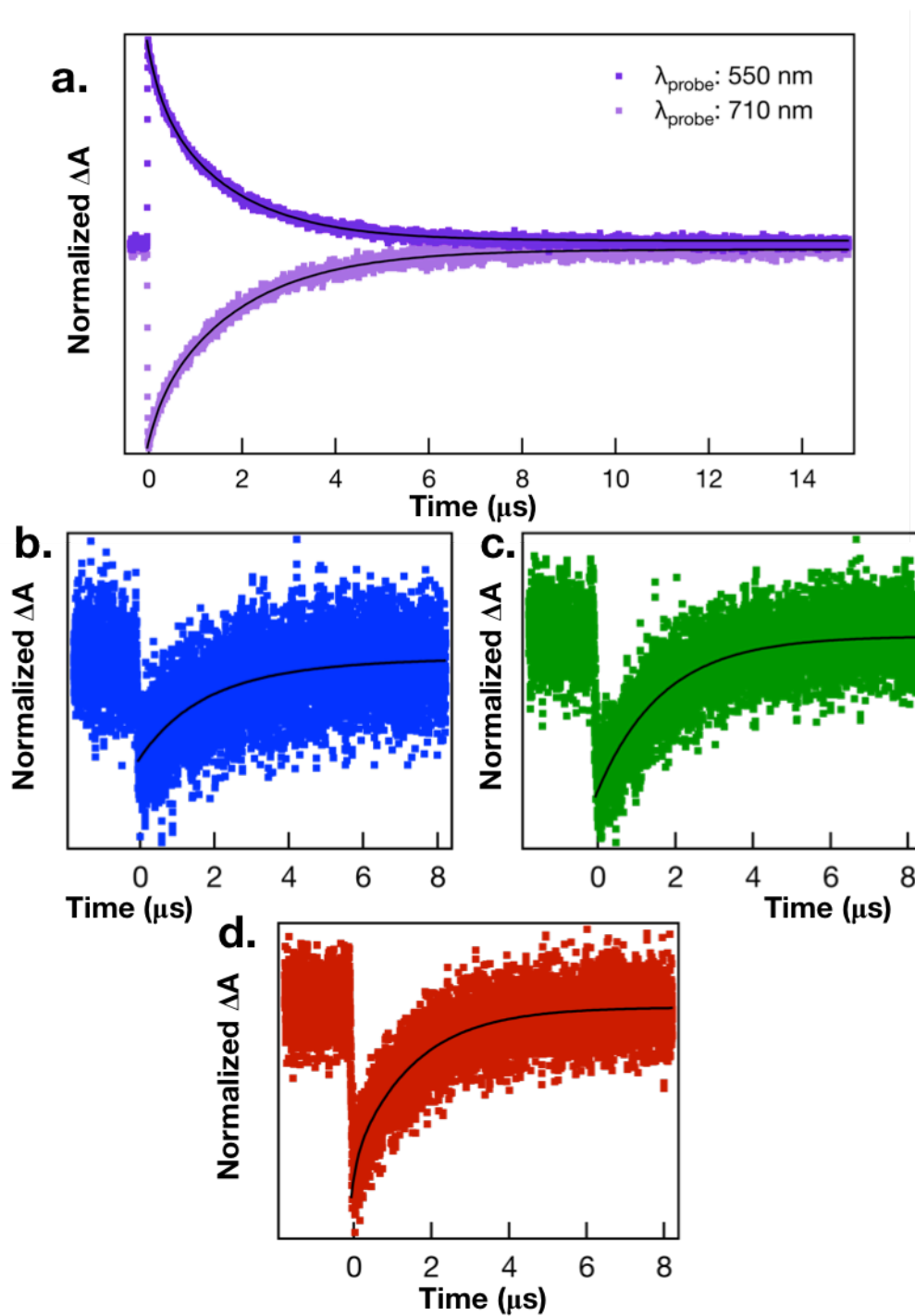


**Figure S2.7** Nanosecond TA kinetics of (a) PbS-805, (b) PbS-970, (c) PbS-1000, and (d) PbS-1075 in toluene following pulsed excitation at 743 nm (1.0 mJ/pulse, 5 ns fwhm). The decays of the PbS NC induced absorption observed at 550 nm and the X1 bleaches at 710, 890, 920 and 1010 nm can be fit by biexponential functions (black lines) with time constants of  $0.22 \pm 0.07$  and  $1.8 \pm 0.2 \mu s$ .

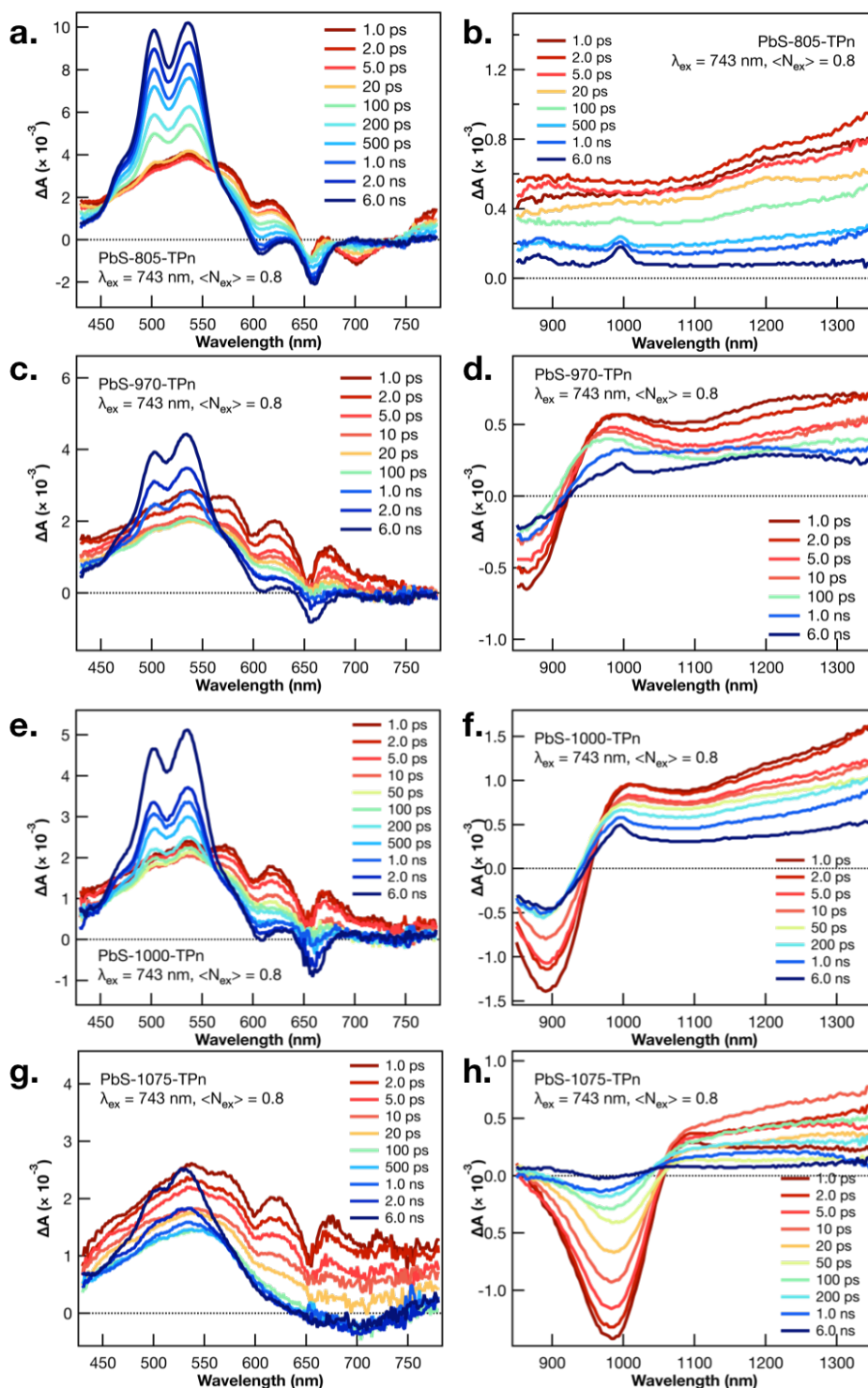


**Figure S2.8** Ultrafast TA difference spectra of PbS-TPn nanocrystal-molecule hybrid materials suspended in toluene following 743 nm pulsed laser excitation (0.15  $\mu\text{J}/\text{pulse}$ , 100 fs fwhm). The spectra correspond to PbS-805-TPn in the (a) visible and (b) near-IR spectral regions, PbS-970-TPn in the (c) visible and (d) NIR, PbS-1000-TPn in the (e) visible and (f) NIR, and PbS-1075-TPn in the (g) visible and (h) NIR. Time delays range from 1.0 ps (red) to 6.0 ns (blue).

**Table S2.1** Decay constants obtained from fitting kinetic traces at single wavelengths of TA data for PbS-TPn nanocrystal-molecule hybrid materials suspended in toluene following pulsed excitation at 743 nm (0.15  $\mu$ J/pulse, 100 fs fwhm).

	$\tau_1$ (ps) 528-540 nm & GSB <sup>a</sup>	GSB $\lambda_{\text{probe}}$ (nm)	$\tau_2$ (ns) 528-540 nm <sup>b</sup>
<b>PbS-805-TPn</b>	1.7 – 2.4	698 – 710	0.35 – 0.41
<b>PbS-970-TPn</b>	5.4 – 10.5	851 – 863	2.7
<b>PbS-1000-TPn</b>	5.7 – 7.3	888 – 900	2.5
<b>PbS-1075-TPn</b>	16 – 27	981 – 993	9.4

*a* Determined by fitting the attenuation of the PbS NC features from 528 – 540 nm (photoinduced absorption) and the ground state bleach (GSB column). *b* Determined from monitoring the rise of the characteristic <sup>3</sup>TPn signal from 528 – 540 nm.

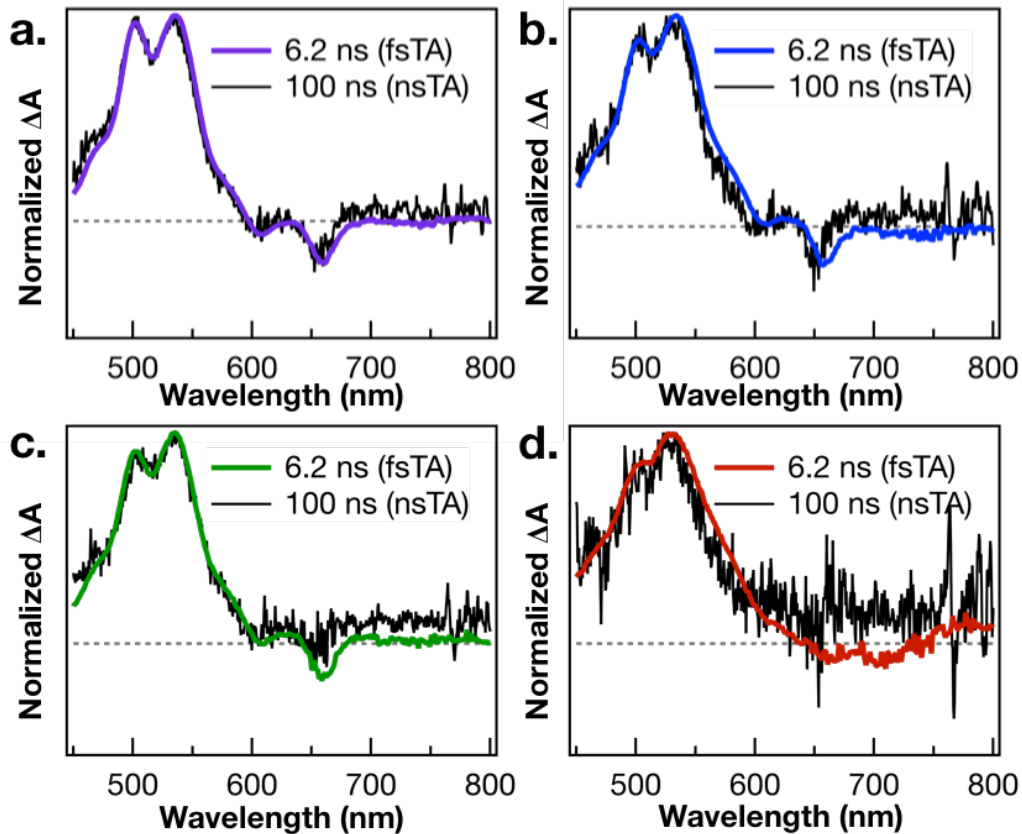


**Figure S2.9** Comparison of normalized, ultrafast (0.15  $\mu\text{J}/\text{pulse}$ , 100 fs fwhm, 743 nm) TA difference spectra (colored) and normalized, nanosecond (1.0 mJ/pulse, 5 ns fwhm, 743 nm) TA difference spectra (black) of PbS-TPn hybrid material suspensions in toluene following pulsed laser excitation. The spectra correspond to **(a)** PbS-805-TPn, **(b)** PbS-970-TPn, **(c)** PbS-1000-TPn, and **(d)** PbS-1075-TPn. Time delays are 6.2 ns for the ultrafast TA spectra and 100 ns for the nanosecond TA spectra.

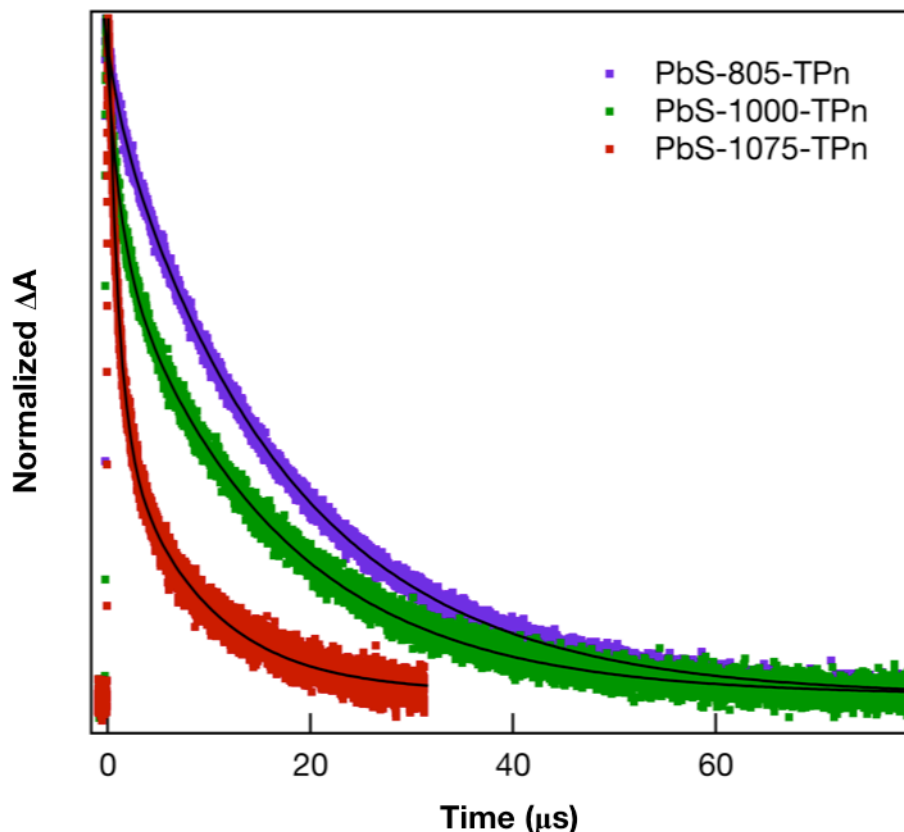


**Figure S2.10** Nanosecond TA kinetics of PbS-TPn nanocrystal-molecule hybrid materials suspended in toluene following pulsed excitation at 743 nm (1.0 mJ/pulse, 5 ns fwhm). The decays of the  $^3\text{TPn}$  feature observed at 534 nm are fit by biexponential functions (black lines) with time constants given in Table S2.2. PbS-970-TPn TA kinetics omitted for clarity.

**Table S2.2** Decay constants obtained from fitting kinetic traces ( $\lambda_{\text{probe}} = 534 \text{ nm}$ ) displayed in Fig. S2.10 to biexponential functions. Data is from TA kinetics of PbS-TPn nanocrystal-molecule hybrid materials suspended in toluene following pulsed excitation at 743 nm (1.0 mJ/pulse, 5 ns fwhm).

	$\tau_1$ ( $\mu\text{s}$ )	$\tau_2$ ( $\mu\text{s}$ )
<b>PbS-805-TPn</b>	$11.7 \pm 0.2$	$22.3 \pm 0.9$
<b>PbS-970-TPn</b>	$1.34 \pm 0.09$	$15.1 \pm 0.2$
<b>PbS-1000-TPn</b>	$1.40 \pm 0.02$	$15.6 \pm 0.1$
<b>PbS-1075-TPn</b>	$0.87 \pm 0.06$	$6.85 \pm 0.06$

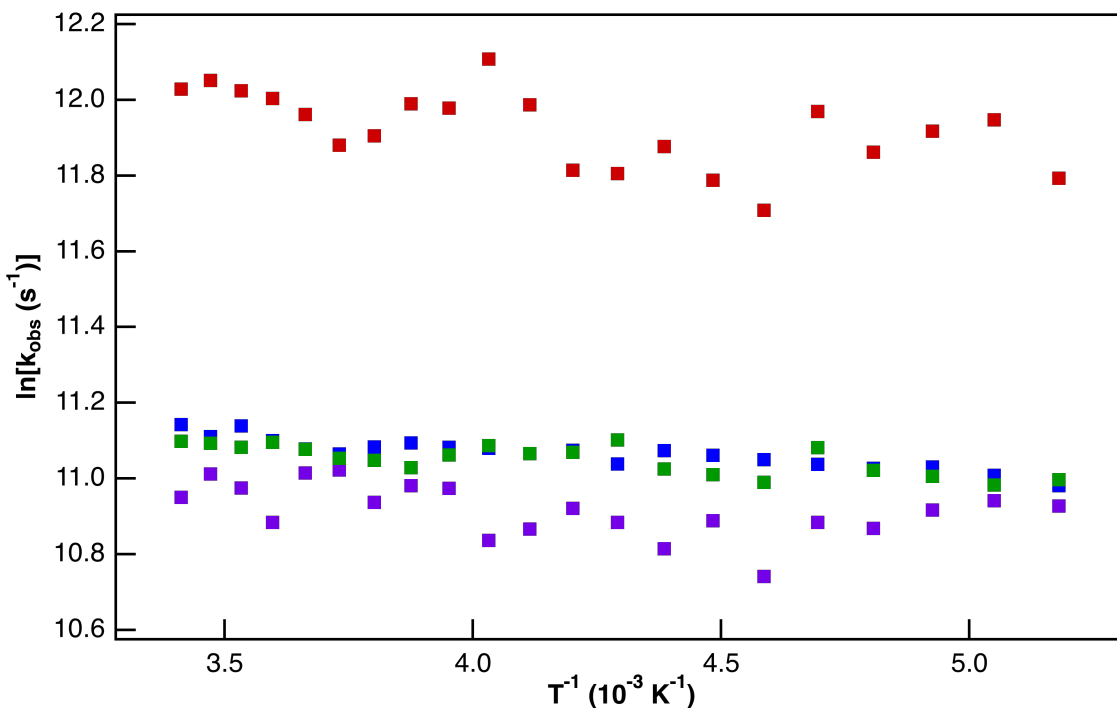


**Figure S2.11** Rate constants from temperature-dependent nanosecond TA kinetics of PbS-TPn nanocrystal-molecule hybrid materials suspended in toluene following pulsed excitation at 743 nm (1.0 mJ/pulse, 5 ns fwhm). The logarithm of the rate constants determined by mathematical fitting of the  $^3\text{TPn}$  decay observed at 534 nm is compared to the inverse of the temperature at which the decay was recorded.

**Table S2.3** Raw time constants and per-TPn-adjusted rate constants obtained by modeling ultrafast TA spectra for PbS-TPn materials. Corresponding basis spectra are displayed in Figure 2.3. For accurate lifetimes for the relaxation of  $^3\text{TPn}$ , see Table S2.2.

	$\tau_1$ (ps)	$k_1$ ( $\times 10^9 \text{ s}^{-1}$ )	$\tau_2$ (ns)	$k_2$ ( $\times 10^6 \text{ s}^{-1}$ )	$\tau_3^a$
<b>PbS-805-TPn</b>	$3 \pm 1$	$18 \pm 6$	$0.39 \pm 0.07$	$140 \pm 40$	infinite
<b>PbS-970-TPn</b>	$4.0 \pm 0.1$	$8 \pm 2$	$1.8 \pm 0.3$	$20 \pm 8$	infinite
<b>PbS-1000-TPn</b>	$6.8 \pm 0.3$	$4 \pm 2$	$1.1 \pm 0.4$	$30 \pm 20$	infinite
<b>PbS-1075-TPn</b>	$12.3 \pm 0.2$	$1.6 \pm 0.5$	$5 \pm 2$	$5 \pm 3$	infinite

<sup>a</sup> The third time constant is “infinite” over the 6.2 ns delay stage of the ultrafast TA experiment.

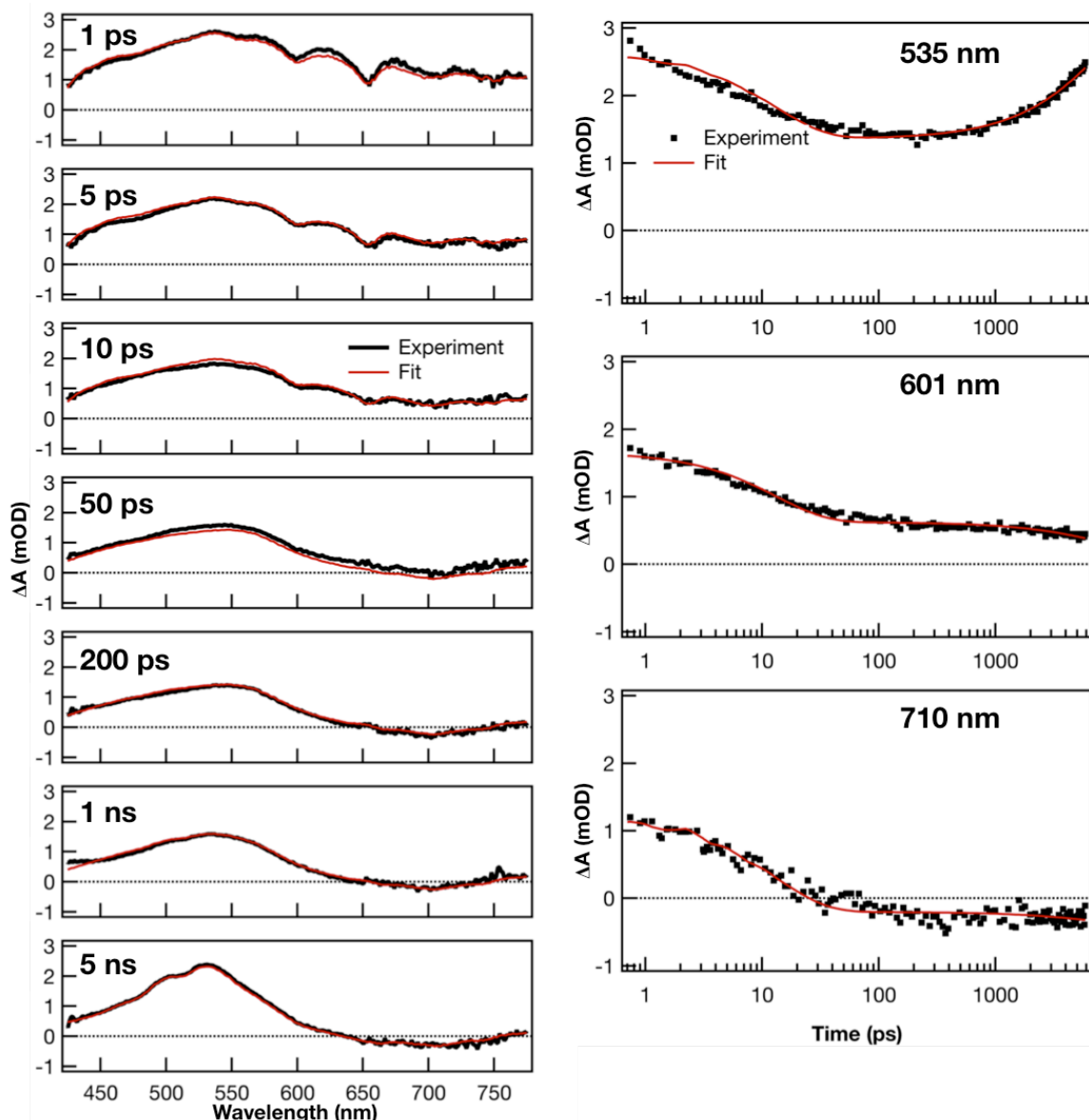


**Figure S2.12** Experimental PbS-1075-TPn ultrafast TA spectra (black) probed in the visible region of the electromagnetic spectrum compared to the fit modeled by linear decomposition (red). Three DADS were necessary to reproduce the changes in the spectra. Time constants for first-order interconversion between the DADS were found to be 12.3 ps and 5 ns as described in Table S2.3.

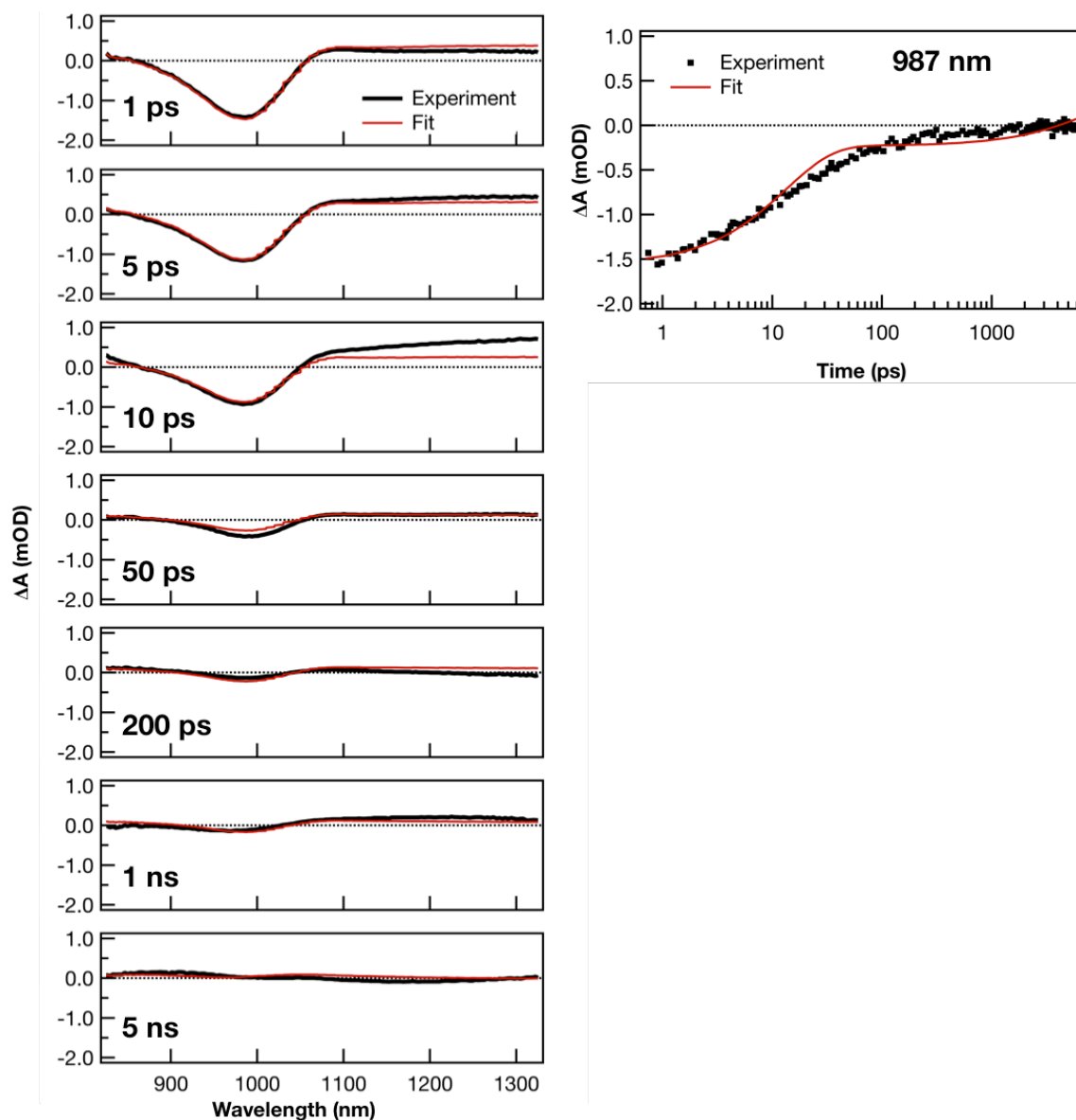


**Figure S2.13** Experimental PbS-1075-TPn ultrafast TA spectra (black) probed in the near-infrared region of the electromagnetic spectrum compared to the fit modeled by linear decomposition (red). Three DADS were necessary to reproduce the changes in the spectra. Time constants for first-order interconversion between the DADS were found to be 12.3 ps and 5 ns as described in Table S2.3.

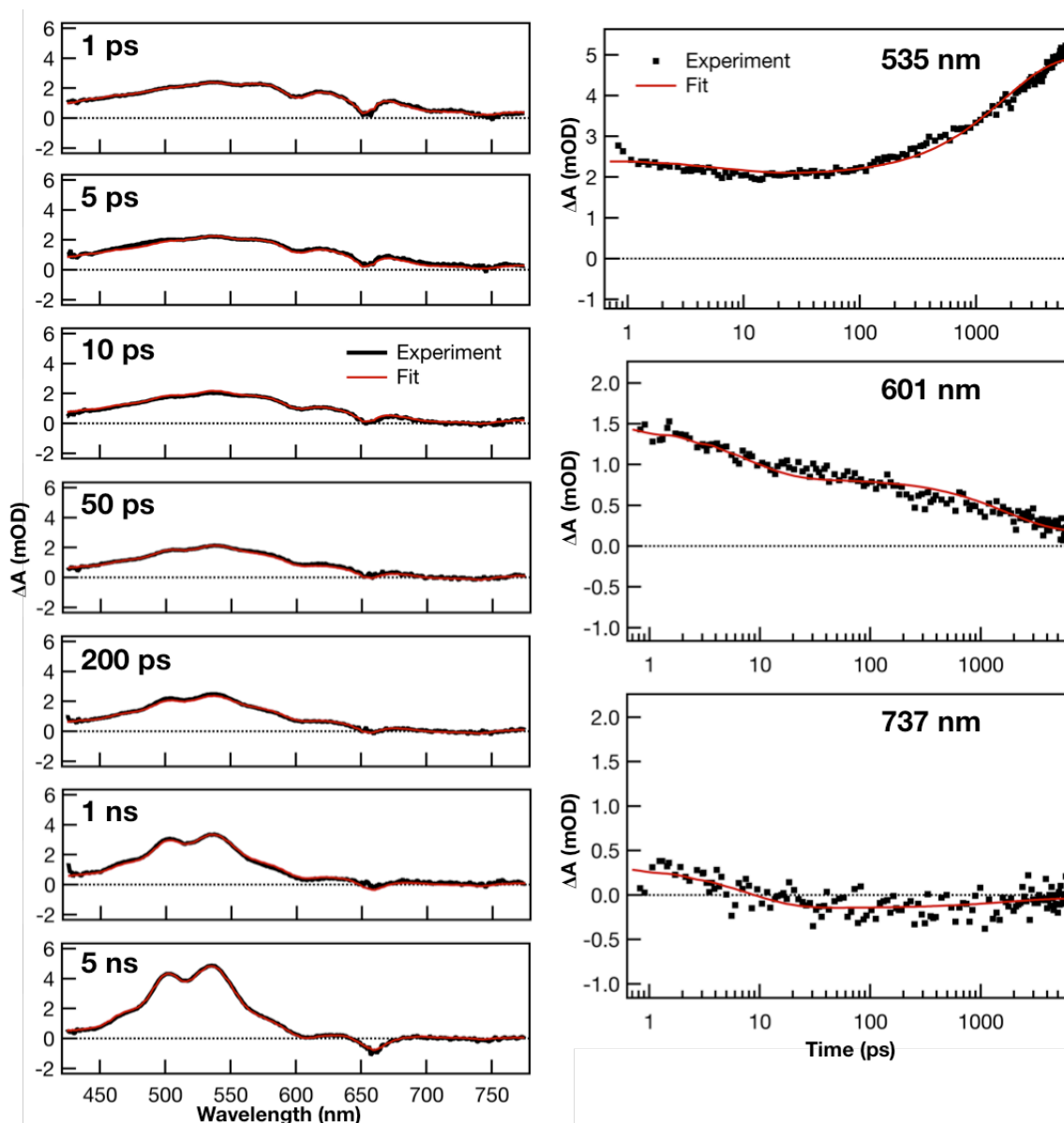


**Figure S2.14** Experimental PbS-1000-TPn ultrafast TA spectra (black) probed in the visible region of the electromagnetic spectrum compared to the fit modeled by linear decomposition (red). Three DADS were necessary to reproduce the changes in the spectra. Time constants for first-order interconversion between the DADS were found to be 6.8 ps and 1.1 ns as described in Table S2.3.

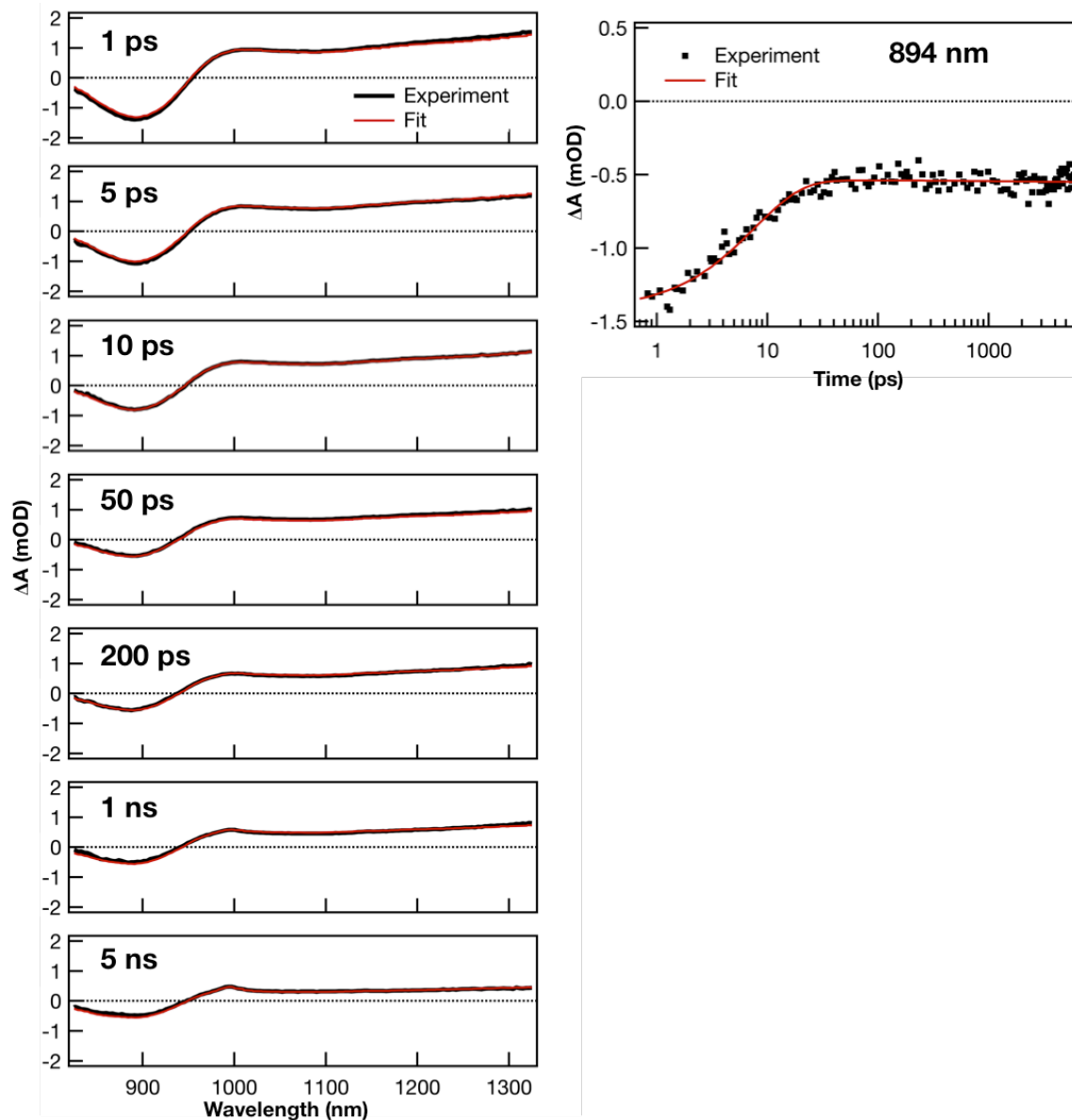


**Figure S2.15** Experimental PbS-1000-TPn ultrafast TA spectra (black) probed in the near-infrared region of the electromagnetic spectrum compared to the fit modeled by linear decomposition (red). Three DADS were necessary to reproduce the changes in the spectra. Time constants for first-order interconversion between the DADS were found to be 6.8 ps and 1.1 ns as described in Table S2.3.

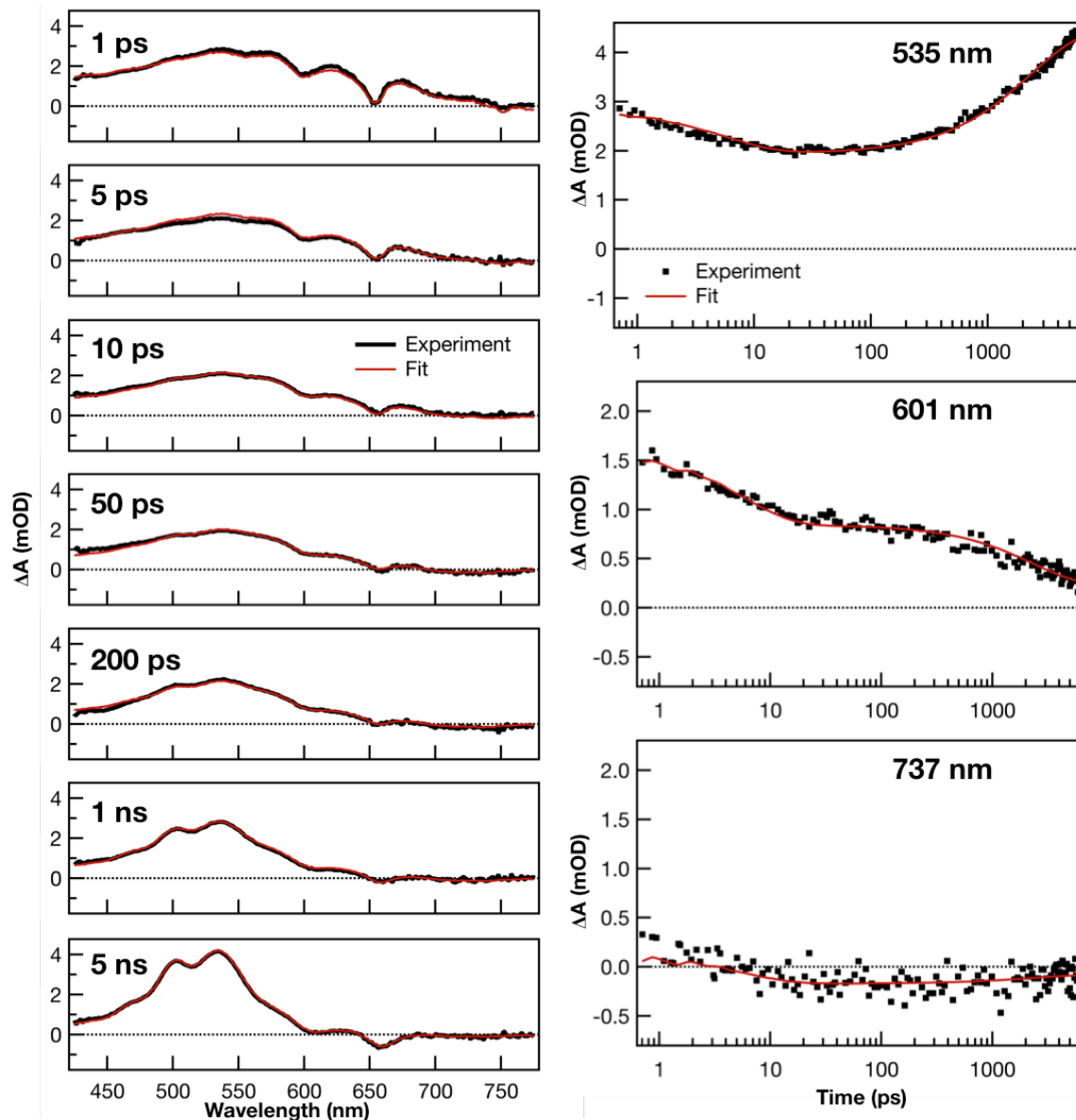


**Figure S2.16** Experimental PbS-970-TPn ultrafast TA spectra (black) probed in the visible region of the electromagnetic spectrum compared to the fit modeled by linear decomposition (red). Three DADS were necessary to reproduce the changes in the spectra. Time constants for first-order interconversion between the DADS were found to be 4.0 ps and 1.8 ns as described in Table S2.3.

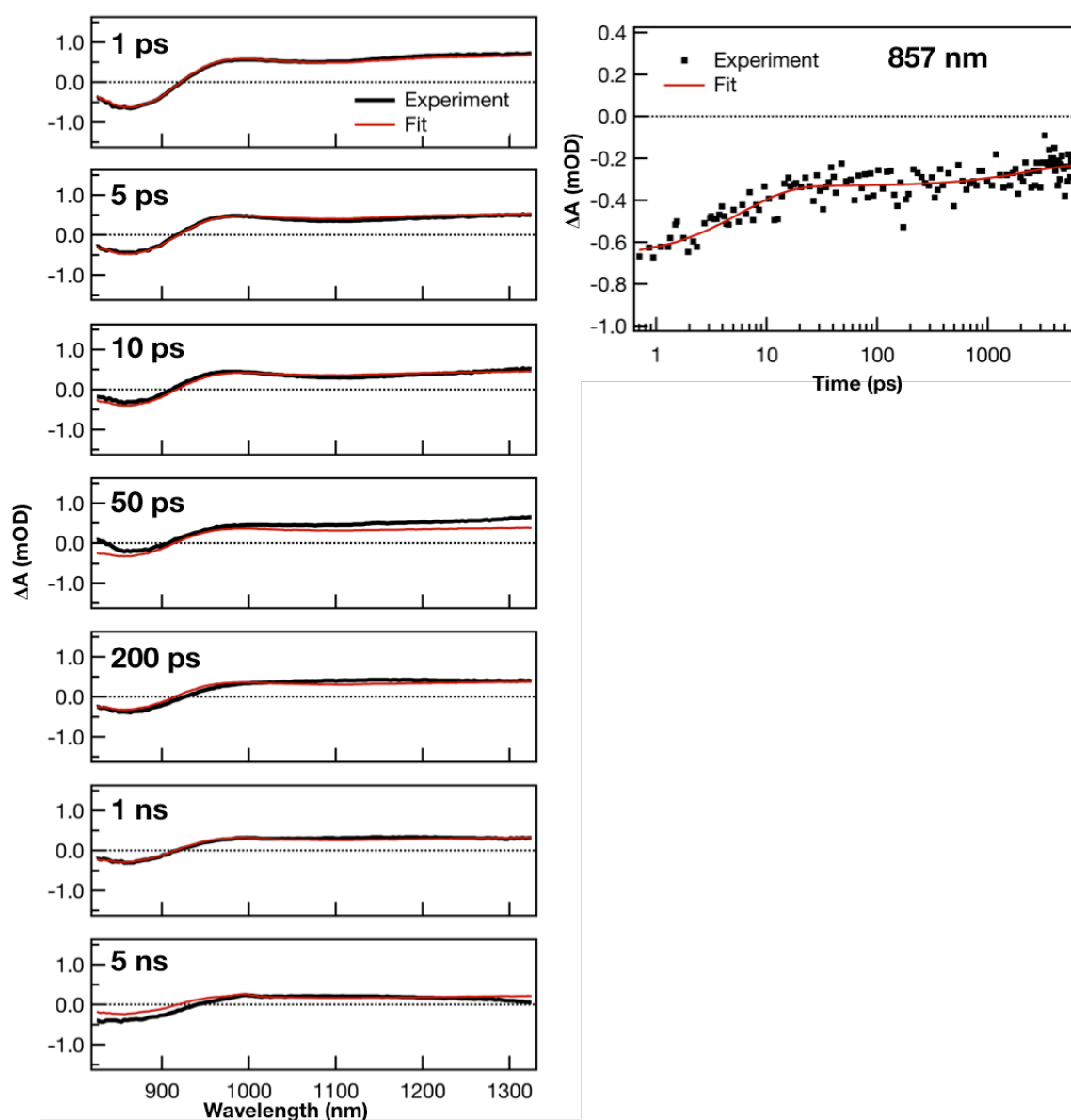


**Figure S2.17** Experimental PbS-970-TPn ultrafast TA spectra (black) probed in the near-infrared region of the electromagnetic spectrum compared to the fit modeled by linear decomposition (red). Three DADS were necessary to reproduce the changes in the spectra. Time constants for first-order interconversion between the DADS were found to be 4.0 ps and 1.8 ns as described in Table S2.3.

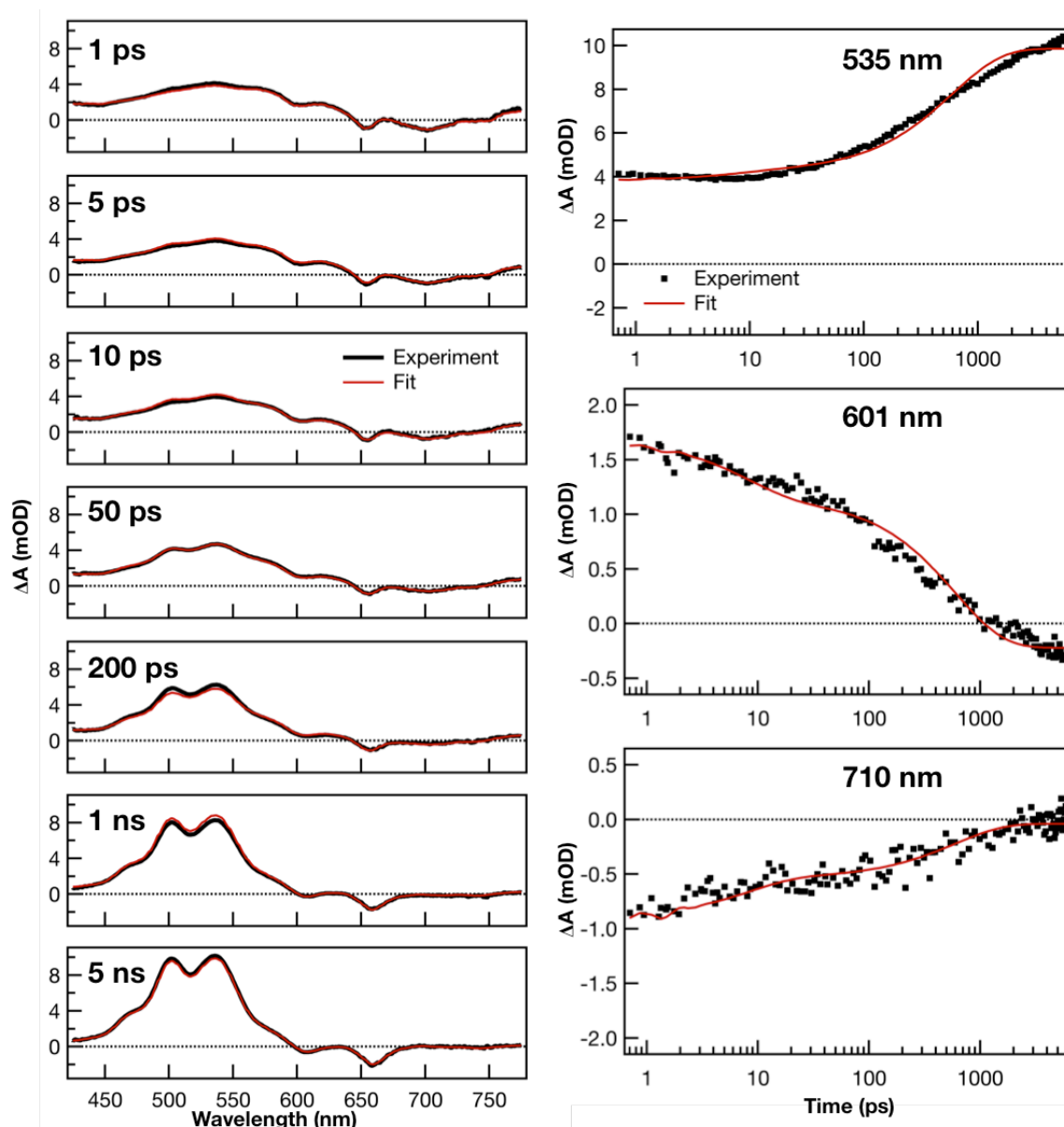


**Figure S2.18** Experimental PbS-805-TPn ultrafast TA spectra (black) probed in the visible region of the electromagnetic spectrum compared to the fit modeled by linear decomposition (red). Three DADS were necessary to reproduce the changes in the spectra. Time constants for first-order interconversion between the DADS were found to be 3 ps and 0.39 ns as described in Table S2.3. This sample was absorbance matched at excitation to the PbS-TPn materials.

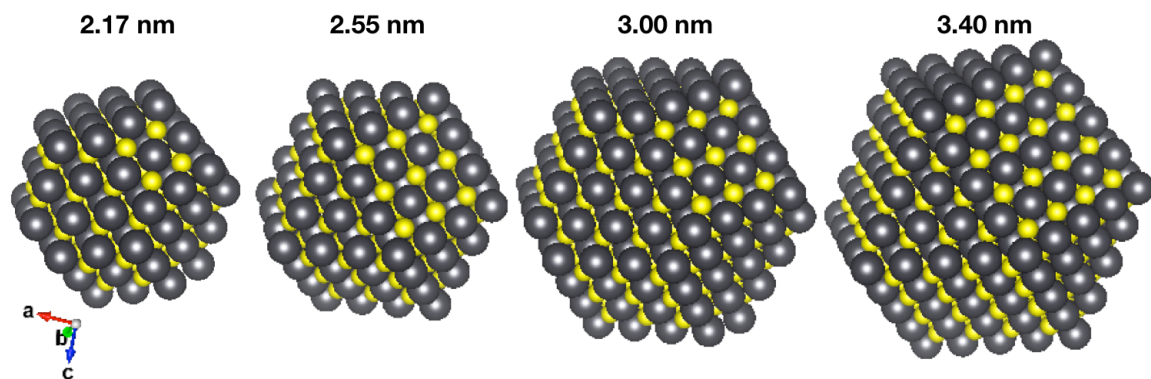


**Figure S2.19** Atomically precise space-filling models of rock salt PbS cuboctahedra possessing vertex-to-vertex distances of 2.17, 2.55, 3.00, and 3.40 nm.

## **CHAPTER 3: CdS Shells Inhibit Surface-Trap Involvement in Triplet Energy Transfer Mechanisms from PbS Nanocrystals**

### **3.1 Abstract**

Semiconductor nanomaterials decorated with molecular chromophores have recently emerged as a promising platform for photonic applications. The energy migration mechanisms at play in systems composed of PbS nanocrystals (NCs) and derivatives of 6,13-bis(triisopropylsilylethynyl)-pentacene (TIPS-pentacene) have proven particularly intransigent. To help elucidate and untangle the mechanisms at the PbS – TIPS-pentacene interface, we have synthesized PbS-CdS core-shell NCs with multiple CdS shell thicknesses ranging from 0 to 1.6 Cd-S bond lengths. After surface functionalization with a carboxylic acid derivative of TIPS-pentacene (TPn), transient absorption and steady state photoluminescence spectroscopic investigation suggests the shells serve to decrease the rate of molecular triplet generation. We conclude this is due to both increased tunneling distance through the CdS shells and blocking PbS surface-trapped states that are non-innocent in PbS-TPn triplet sensitization. We also propose that the sulfur-to-sulfur interatomic distance is a more reasonable unit of length for characterizing the thickness of cation-exchange-generated shells. Lastly, we determine that indirect triplet sensitization of TPn by PbS surface states, while viable, is less efficient than tunneling through CdS from an adequately-passivated PbS NC.

### **3.2 Introduction**

Recently, triplet sensitization of organic molecules by colloidal semiconductor nanocrystals (NCs), also called quantum dots (QDs), has been discovered as an efficient route to generate organic molecular triplet excited states.<sup>1-5</sup> These processes allow

absorbed light energy to be utilized in applications such as sensitized triplet-triplet annihilation photon upconversion<sup>2, 6-14</sup> and photoredox catalysis.<sup>15, 16</sup> However, molecular triplet generation in these systems can be more diverse than only Dexter-like triplet-triplet energy transfer (TTET) mechanisms consisting of concerted two-electron exchange<sup>17</sup> between the QD donor and the organic molecular acceptor. Progressively greater numbers of spectroscopic studies indicate that NC-to-molecule TTET is often mediated by indirect mechanisms consisting of charge-carrier-trapping states<sup>18-20</sup> or interfacial charge-transfer states.<sup>21-23</sup> Similar interfacial charge-transfer-mediated TTET mechanisms have also been observed in the solid state.<sup>24-26</sup>

As part of efforts to better understand and potentially counteract NC surface effects,<sup>27-33</sup> researchers have employed core-shell heterostructures where the core is the QD and the shell serves as a putative passivation layer.<sup>32, 34-36</sup> Implementation of the core-shell motif within NC-sensitized triplet-triplet annihilation photon upconversion (TTA-UC) schemes has led to measurable increases in the detected quantum yield of TTA-UC when high laser excitation power densities are used.<sup>10, 37-39</sup> The basis for this uptick in quantum efficiency was previously assigned to suppression of competitive charge transfer pathways in a system comprised of PbS-CdS core-shell NCs and a derivative of tetracene.<sup>37</sup> Conversely, transient absorption studies on shell-free PbS QDs paired with a carboxylic acid derivative of 6,13-bis(triisopropylsilylethynyl)-tetracene (TIPS-tetracene) makes a compelling case against the formation of any photoinduced charge transfer in the observed excited state dynamics.<sup>40</sup>

To shed further empirical light on the complex mechanisms at the acene-PbS NC interface, we have brought the PbS-CdS core-shell motif to bear on the TIPS-pentacene

and PbS QD combination. This has been achieved by synthesizing PbS-CdS core-shell NCs with multiple CdS shell thicknesses and functionalizing their surfaces with a carboxylic acid derivative of TIPS-pentacene, 6,13-bis(triisopropylsilylethynyl)-pentacene-2-carboxylic acid (TPn).<sup>41</sup> The relevant energy levels of TPn and the PbS-CdS NC hybrid materials investigated here are presented in Figure 3.1a.

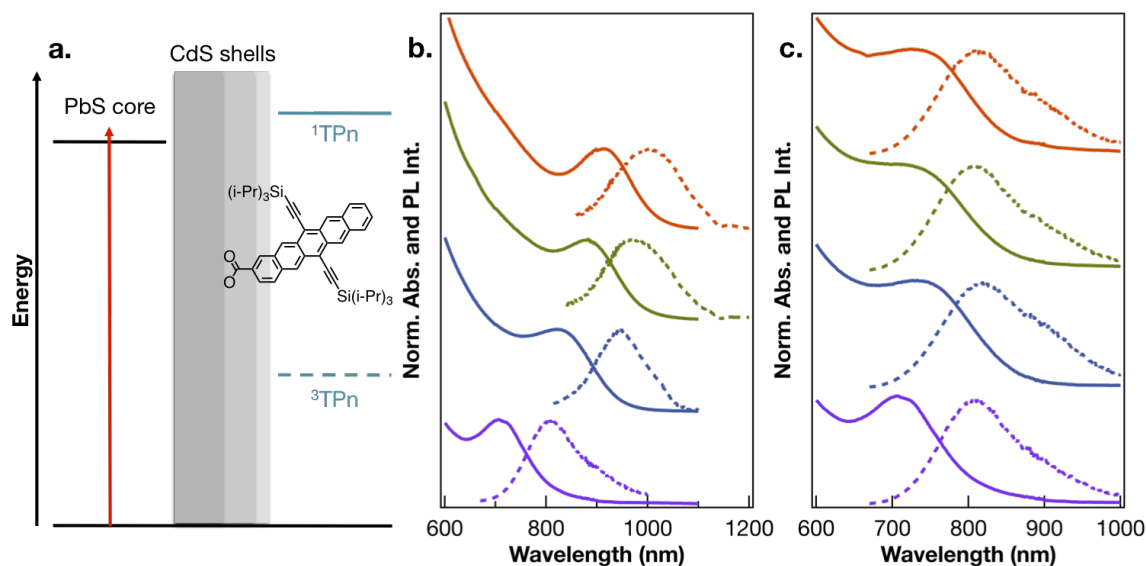


**Figure 3.1** (a) Schematic illustration of PbS core first exciton and TPn-centered energy levels separated by CdS shells of varying thickness. (b) Electronic absorption (solid lines) and emission spectra (dashed lines) for PbS NCs ranging in diameter from  $3.0 \pm 0.5$  nm (top, orange) to  $2.2 \pm 0.3$  nm (bottom, violet). (c) Electronic absorption (solid lines) and emission spectra (dashed lines) for PbS-CdS NCs following cation exchange. Colors are matched to the parent PbS NCs in (b), and 2.2 nm PbS NCs (bottom, violet) were not subjected to cation exchange.

Our data suggests that the addition of CdS shells serves to decrease the rate constants for formation of the intermediate compared to their shell-free counterparts. Additionally, the same CdS shell thickness concomitantly retards the rate of production of the TPn-localized triplet excited state in comparison to the shell-free PbS QD of comparable bandgap energy. We find that the increasingly sluggish rates of <sup>3</sup>TPn generation could be ascribed to an instant CdS-induced drop-off or a simple distance dependence with a tunneling coefficient  $\beta = 0.42 \text{ \AA}^{-1}$ . We conclude that this increased

PbS-to-TPn distance is also responsible for the attenuation of a transient dipole-induced absorption shift observed in the transient absorption (TA) signal for TPn molecules appended to photoexcited PbS NCs. Separate TA and photoluminescence (PL) spectra show clear evidence that states involving surface-trapped charge carriers are inhibited by the introduction of CdS shells. In that context, an extremely high relative TTET efficiency for the model PbS-TPn system without a CdS shell suggests the indirect sensitization mechanism likely utilizes these surface states. However, sufficiently thick CdS shells produce the highest yield of  $^3\text{TPn}$  after PbS-selective excitation, implying that indirect sensitization *via* the PbS surface is not the most efficient pathway to molecular triplet generation.

### 3.3 Results and Discussion

#### 3.3.1 Optical Properties of PbS-CdS Core-Shell NCs

The electronic absorption and photoluminescence spectra for the four sizes of PbS parent NCs synthesized are given in Figure 3.1b. To maintain consistency with previously published results,<sup>20</sup> the parent PbS NCs are referred to as PbS-805, PbS-945, PbS-970, and PbS-1000, as they possess photoluminescence intensity maxima near 805, 945, 970, and 1000 nm, respectively. The parent NCs PbS-945, PbS-970, and PbS-1000 were converted to PbS-CdS core-shell NCs through cation exchange of  $\text{Cd}^{2+}$  for  $\text{Pb}^{2+}$  (see Experimental Methods). Figure 3.1c presents the electronic absorption and photoluminescence spectra for the three resulting PbS-CdS core-shell NC species, along with PbS-805, which will serve as the CdS-free control sample. As the PbS cores are responsible for the low-energy optical features in PbS-CdS heterostructures, the energetic match of the optical properties across the series is indicative of matching core

diameters.<sup>42</sup> EDS confirmed the presence of Cd atoms in the core-shell NCs, while analysis of TEM images (Figure S3.1) indicates the NCs have not changed size significantly after undergoing cation exchange. It has been proposed that Cd<sup>2+</sup> ions can be introduced in place of Pb<sup>2+</sup> ions, even though CdS (zinc blende) and PbS (rock salt) have different crystal structures. This proposal was rationalized by noting that the S<sup>2-</sup> sublattice experiences minimal distortion between PbS and CdS.<sup>42-44</sup> Furthermore, the cation exchange method employed in this work subjected the NCs to 80°C for 6 minutes, and the mild conditions employed were not anticipated to be sufficient to reorganize the bulk lattice.<sup>42</sup> CdS shell thicknesses for the PbS-CdS NCs were estimated from the optical properties of the parent PbS NC and the final core-shell NC using an empirical formula developed by Moreels *et al.*<sup>45</sup> The PbS-CdS core-shell NCs will be designated herein by their parent PbS NC maximum emission intensity wavelength as opposed to their respective calculated shell thicknesses, *i.e.* PbS-945-CdS (2 Å CdS shell), PbS-970-CdS (3.5 Å), and PbS-1000-CdS (4 Å). These CdS shell thickness values are equivalent to 0.8, 1.4 and 1.6 Cd-S bond lengths beyond the respective PbS cores. Considering the cation-exchange mechanism employed to generate the shells, we suggest the Cd-S bond length is insufficient to characterize the repeating layer of the shell. Since Cd<sup>2+</sup> cations occupy tetrahedral sites while Pb<sup>2+</sup> cations vacate octahedral sites within the S<sup>2-</sup> sublattice, the S-S interatomic distance (PbS = 4.25 Å, CdS = 4.20 Å) appears more relevant as a measure of shell thickness. By this measure, the CdS shell thicknesses herein are 0.5, 0.8, and 1.0 complete cation-exchange layers.

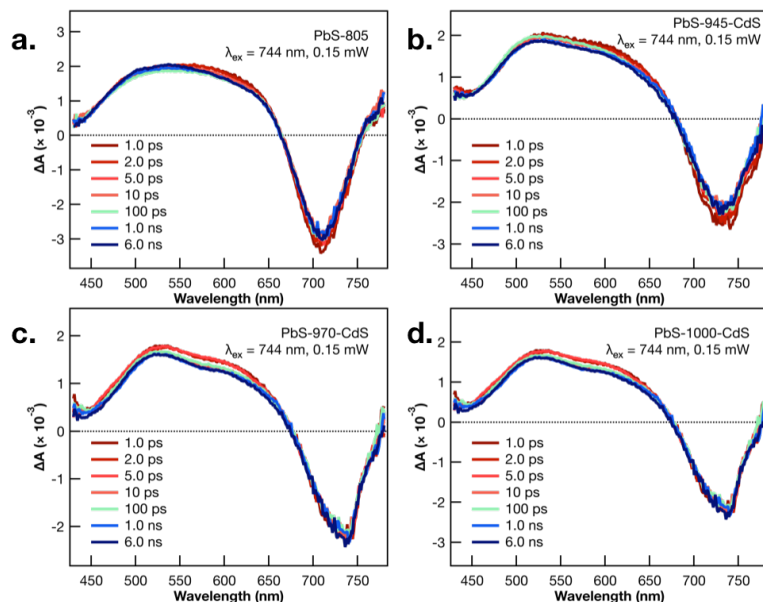


**Figure 3.2** Ultrafast TA difference spectra of (a) PbS-805, (b) PbS-945-CdS, (c) PbS-970-CdS, and (d) PbS-1000-CdS nanocrystal suspensions in toluene following 744 nm pulsed laser excitation (0.15  $\mu\text{J}/\text{pulse}$ , 100 fs fwhm). Time delays range from 1.0 ps (red) to 6.0 ns (blue).

The oleate-capped PbS-CdS NC TA difference spectra upon excitation (Figures 3.2b-d) are reminiscent of those observed for CdS-free PbS-805 NCs (Figure 3.2a). The oleate-capped materials have a characteristic negative TA feature associated with bleaching of their first exciton absorption band and a broad excited-state absorption band characteristic of interband transitions in the PbS cores.<sup>32, 46-48</sup> There is a progression in the shape of the PbS-805 excited-state absorption spectral feature from one broad feature to two separate, less broad features as CdS shell thickness increases. This spectral shape change is attributed to the added presence of a pump-probe biexcitonic state characteristic of improved surface trap passivation upon addition of a CdS shell.<sup>32</sup> Nanosecond TA experiments (Figures S3.2, S3.3) show symmetric decay of PbS-CdS excited state spectral features on a 2.4  $\mu\text{s}$  time scale, consistent with reported data from other oleate-capped PbS NCs.<sup>18-20, 40</sup> After functionalizing the PbS-CdS core-shell NC surface with TPn molecules (Figure S3.4), the TA spectra upon NC-selective excitation (Figures 3.3a-

d) bear qualitative resemblance to spectra previously obtained for PbS-TPn hybrid materials.<sup>18-20</sup>

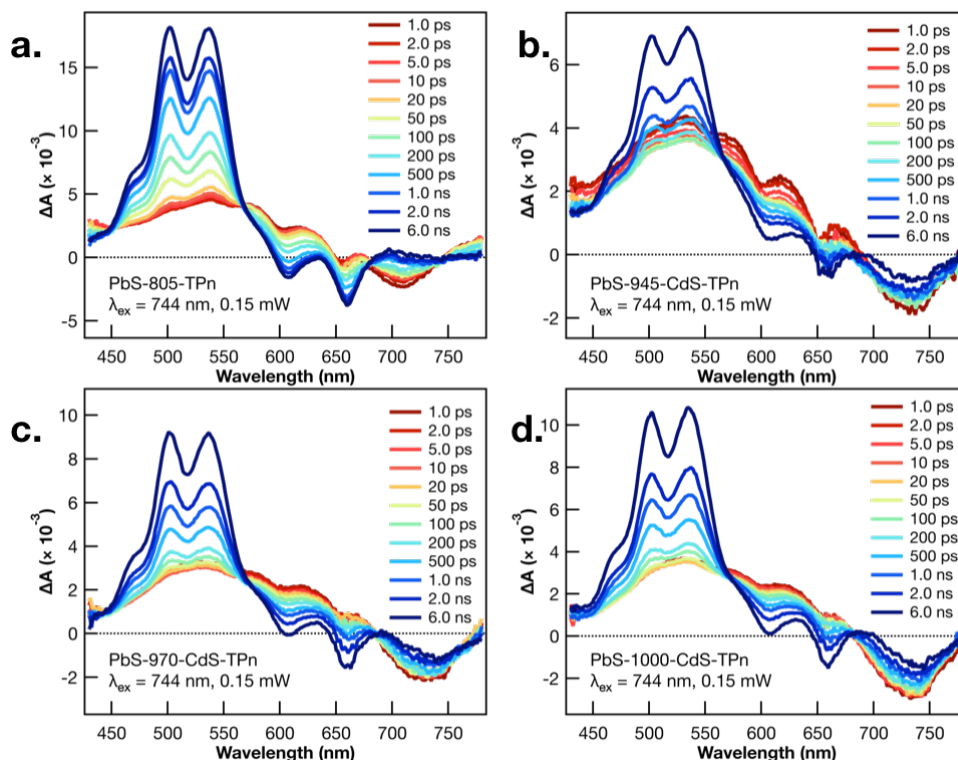


**Figure 3.3** Ultrafast TA difference spectra of (a) PbS-805-TPn, (b) PbS-945-CdS-TPn, (c) PbS-970-CdS-TPn, and (d) PbS-1000-CdS-TPn nanocrystal suspensions in toluene following 744 nm pulsed laser excitation (0.15  $\mu$ J/pulse, 100 fs fwhm). Time delays range from 1.0 ps (red) to 6.0 ns (blue).

### 3.3.2 TPn Triplet Sensitization by PbS-CdS NCs

The first excited state formed after NC-selective excitation at 744 nm resembles that of the oleate-capped NCs with new negative absorption features superimposed in regions corresponding to the ground state absorption spectrum of TPn. These negative features are typically assigned as a transient dipole-induced shift of the  $S_0$  to  $S_1$  electronic transitions in TPn.<sup>18-20, 49, 50</sup> In a study involving PbS-CdS NCs and a tetracene derivative, similar negative absorption features corresponding to the absorption spectrum of the tetracene derivative were described as “instantaneous bleaching,” assigned to ultrafast oxidation of the molecule.<sup>37</sup> Generally, the features from the PbS excited state and

transient dipole-induced shift disappear over the first 10's to 100's of ps, followed by the growth of a feature assigned to NC-bound  $^3\text{TPn}$ .<sup>18-20</sup> The molecular triplets grow in on ns timescales, suggesting addition of sub-monolayer CdS is insufficient to alter the stepwise triplet sensitization mechanism or induce a concerted Dexter-like process.

The kinetic time constants, on the contrary, are markedly different. The trend of a mismatch between the rates of PbS excited state decay and  $^3\text{TPn}$  growth persists somewhat (Figure 3.4), suggesting a degree of continued existence for the kinetic intermediate.<sup>18-20</sup> The ground state bleach features associated with the first exciton of the core-shell-TPn hybrid materials do not fully recover on the 6.2 ns experimental time scale, in contrast to the PbS-805-TPn materials, Figure 3.4b. Once the final  $^3\text{TPn}$  excited state has been formed, supra-nanosecond time-resolved experiments (Figures S3.5, S3.6) demonstrate that  $^3\text{TPn}$  appended to PbS-CdS core-shell NCs relaxes to the ground state on similar microsecond time scales as free TPn<sup>18</sup> and PbS-appended  $^3\text{TPn}$ .<sup>18-20</sup>

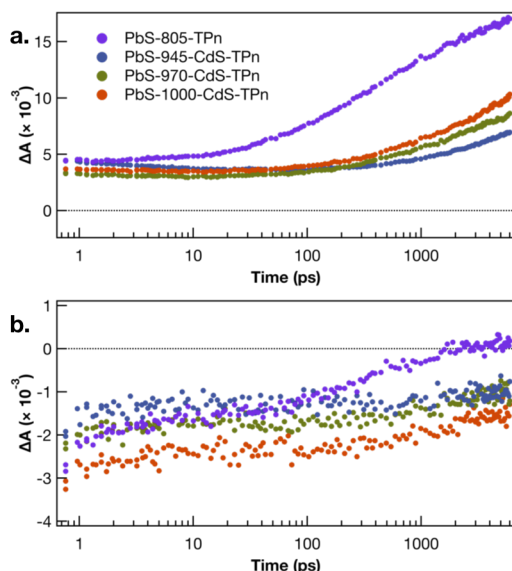


**Figure 3.4** Ultrafast TA kinetics monitoring the (a)  $^3\text{TPn}$  signal probed at 534 nm and (b) PbS first exciton bleach signal probed at 740 nm for PbS-805-TPn (purple), PbS-945-CdS-TPn (blue), PbS-970-CdS-TPn (green), and PbS-1000-CdS-TPn (orange) suspensions in toluene following 744 nm pulsed laser excitation (0.15  $\mu\text{J}/\text{pulse}$ , 100 fs fwhm).

### 3.3.3 Attenuation of the Transient Dipole-Induced Absorption Shift

These findings alternately confirm and contradict a previous report utilizing a tetracene-based acceptor.<sup>37</sup> In that study, molecular triplet formation was assigned to direct Dexter-like triplet energy transfer and the CdS shells putatively suppressed competitive electron transfer processes. The discrepancy regarding the transient dipole-induced shift is still a matter of some debate in the literature.<sup>3, 18-20, 51, 52</sup> However, it may have its origin in the intrinsic energetic differences between tetracene and pentacene, since an indirect exciton generation mechanism from semiconductor NCs to TPn has also been reported for the singlet,  $^1\text{TPn}^*$ .<sup>21</sup> Furthermore, we observed in our TA spectra the attenuation of the feature that others and we have assigned in PbS-TPn<sup>18, 20</sup> and a related system<sup>19</sup> as a transient dipole-induced absorption shift, analogous to the so-called Stark effect. When this feature was observed in the aforementioned system of PbS-CdS NCs with a tetracene derivative, it was described as “instantaneous bleaching” by Huang, Xu *et al.*<sup>37</sup> This assignment was made on the basis of the observed attenuation by a CdS shell and the assumption that this shell was blocking hot hole injection. We posit herein that the observed attenuation of the transient dipole-induced effect in TA spectra for PbS and TIPS-pentacene is due to the increased distance between the shell-appended molecules and the photo-excited PbS cores.

This rationalization starts from treating the PbS-CdS core-shell NCs as having a type I band alignment.<sup>42</sup> In a type I core-shell structure, the photo-generated charge carriers will be confined to the core,<sup>53</sup> PbS in this case. The effect of the CdS shell on the transient dipole-induced shift is primarily to increase the average distance between the photo-excited cores and the TPn molecules that display the TA signal. Distance is also

implicated by Coulomb's law, because the other likely culprit, dielectric screening, should decrease when changing composition from entirely PbS ( $\epsilon_{\text{bulk}} = 169$ ) to a mix of PbS and CdS ( $\epsilon_{\text{bulk}} = 8.6$ ). The increased distance across the CdS shells is also responsible for the decrease in the rate constants for formation of  $^3\text{TPn}$  with the addition of a CdS shell. This finding is in accordance with a triplet-formation step that obeys Marcus theory.<sup>20, 54</sup>

### 3.3.4 Rate Constants for TPn Triplet Formation

To draw further conclusions about the impact of the CdS shells on the kinetic intermediate and on the generation of  $^3\text{TPn}$ , rate constants were calculated for the individual processes. Single wavelength kinetic analysis of the traces in Figure 3.4 is complicated by the presence of overlapping spectral features belonging to PbS and TPn (Figure 3.3). We thus chose to de-convolute the kinetics by fitting the time-resolved TA difference spectra with a spectral decomposition model<sup>20</sup> (see Experimental Methods). The decay-associated difference spectra (DADS) fit to the TA spectra collected over the first 6.2 ns after pulsed 744 nm excitation are displayed in Figures 3.5a-d.

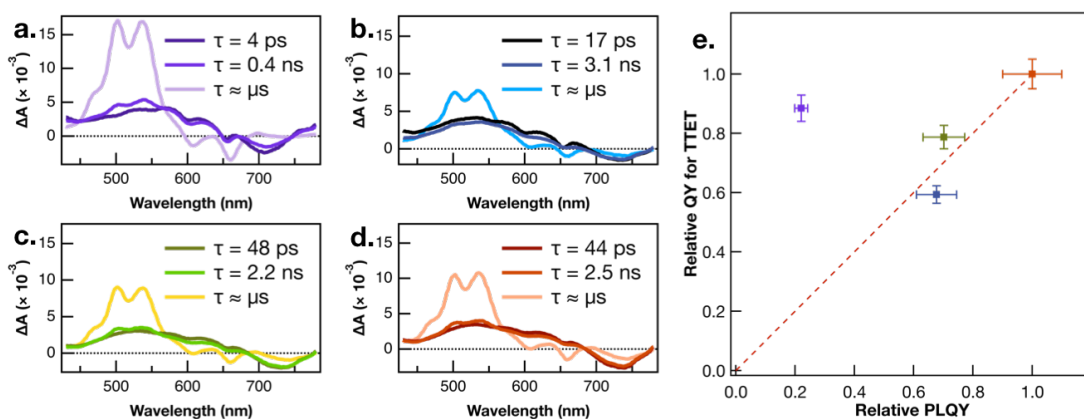


**Figure 3.5** Basis spectra modelled on TA spectra of (a) PbS-805-TPn, (b) PbS-945-CdS-TPn, (c) PbS-970-CdS-TPn, (d) PbS-1000-CdS-TPn materials, and (e) Graphical comparison of relative QY for TTET in PbS-CdS-TPn materials with relative PLQY for the PbS-CdS QD with the same CdS shell thickness. Dashed line included in (e) to show trend for perfect proportional relationship.

The time constants extracted from the fit are given in Table 3.1, along with “intrinsic” rate constants, which were obtained by dividing by the average number of surface-bound TPn molecules. Examination of the data contained therein shows that the processes after photo-excitation have been uniformly slowed by the addition of CdS shells. The rate constants associated with hole trapping in the PbS cores,  $k_1$ , exhibit an exponential decay with shell thickness, corresponding to a tunneling coefficient of  $\beta = 0.69 \text{ \AA}^{-1}$  (Figure S3.7a). This distance-dependent exponential decay behavior matches what would be expected from Type-I core-shell heterostructures. For the rate constant of  $^3\text{TPn}$  formation,  $k_2$ , the data can be interpreted as being “wire-like” for different shell thicknesses after an immediate drop-off upon addition of a CdS shell (Figure S3.7b). If, on the other hand, a distance-dependent exponential decay is fit to the rate constants, a tunneling coefficient of  $\beta = 0.42 \text{ \AA}^{-1}$  is obtained. Interestingly, this value for beta is consistent with a value found for TTET from PbS to tetracene derivatives where the distance is due to phenyl spacers on the acceptor molecules.<sup>52</sup> Distance-dependent decay kinetics is also more consistent with the Type-I band structure of PbS-CdS. The  $k_1$  value and the relative PLQY value obtained for PbS-945-CdS each fit within their respective trend from the other three materials, indicating the  $\text{Cd}^{2+}$  cations, confirmed by EDS, have an effect on the optical properties. However, the obtained  $k_2$  value deviates greatly from the exponential relationship that would be predicted solely from the PbS-CdS band structure. We propose that this is due to the CdS shell being less than a complete S-S interatomic spacing in thickness. We suspect that the cation exchange process has altered the surface chemistry of the PbS-945-CdS NCs, which in turn is altering their interactions with the appended TPn molecules. In summation, the increased distance that the charge

carriers must tunnel, combined with the attenuation of the transient dipole-induced absorption shift, is a likely explanation for the retardation of the rate of triplet formation.

**Table 3.1** Raw time constants and per-TPn-adjusted rate constants obtained by modeling ultrafast TA spectra for PbS-CdS-TPn and PbS-805-TPn materials. Corresponding basis spectra are displayed in Figures 3.5a-d. The third time constant is “infinite” over the 6.2 ns delay stage of the ultrafast TA experiment. For accurate lifetimes for the relaxation of <sup>3</sup>TPn, see Table S3.1.

	$\tau_1$ (ps)	$k_1$ ( $\times 10^9$ s <sup>-1</sup> )	$\tau_2$ (ns)	$k_2$ ( $\times 10^6$ s <sup>-1</sup> )	$\tau_3$
<b>PbS-805-TPn</b>	4 ± 2	20 ± 10	0.4 ± 0.1	180 ± 30	∞
<b>PbS-945-CdS-TPn</b>	17 ± 3	3 ± 1	3.1 ± 0.2	17 ± 6	∞
<b>PbS-970-CdS-TPn</b>	48 ± 3	1.4 ± 0.5	2.2 ± 0.3	29 ± 6	∞
<b>PbS-1000-CdS-TPn</b>	44 ± 7	1.9 ± 0.9	2.5 ± 0.3	29 ± 8	∞

### 3.3.5 Efficiencies of TPn Triplet Sensitization

Analyzing the rate constants for the formation of <sup>3</sup>TPn (Table 3.1), and the amplitude of its TA signal 6.2 ns after excitation (Figure 3.3), the most efficient route to <sup>3</sup>TPn would appear to be shell-free. Conversely, the material with the thickest shell, PbS-1000-CdS-TPn, generates the largest-amplitude <sup>3</sup>TPn TA signal 100 ns after excitation (Figure S3.6). This suggests that sufficient surface passivation (Figure 3.2d) can force PbS-TPn triplet sensitization to proceed along a more efficient pathway. Insight into the source of that efficiency can be gleaned from examination of the time constants for the formation of the kinetic intermediate,  $\tau_1$  (Table 3.1) or the equivalent rate constants,  $k_1$  (Figure S3.7a). Previous studies on PbS-TPn with different sizes of PbS QD and in the absence of CdS shells have shown that the time constants of formation of the intermediate never exceed ~12 ps.<sup>20</sup> Upon introduction of CdS shells, the same time constants not only increase, from 4 ± 2 ps, but they exceed 12 ps and increase with increasing CdS shell thickness. The decrease in the rate of formation of the PbS-TPn

spectral intermediate with increasing CdS shell thickness is consistent with the hypothesis that the PbS surface is complicit in the formation of the intermediate.<sup>19, 20</sup>

The increase in surface passivation can also be imputed by comparison of the relative PL quantum yields (PLQYs) of the PbS-CdS NCs without TPn functionalization (Figure S3.8a). The PLQY increases monotonically with increased CdS shell thickness, as would be expected with decreased surface-trapping behavior. In all cases, <sup>3</sup>TPn formation vastly outcompetes PL from the PbS cores (Figure S3.8b). Even in PbS-1000-CdS-TPn, with its high relative PLQY and sluggish rate of <sup>3</sup>TPn formation, the PL quenching is ~98% efficient. Analysis of the amplitudes of the TA signal for <sup>3</sup>TPn 100 ns after excitation allows for a relative comparison of the QY of TTET. Evaluation of the relative PLQYs for the un-functionalized QDs against the relative QY of <sup>3</sup>TPn formation for the functionalized QDs in Figure 3.5e shows that the shell-free PbS-805-TPn is an extreme outlier. The anomalously high relative QY of <sup>3</sup>TPn formation from the species without a CdS shell indicates that the surface-trapped states likely function as viable intermediates in PbS-TPn triplet sensitization.<sup>19</sup> The formation of the surface-trapped intermediate being intrinsic to the PbS NC is consistent with the rate constant for the first step being independent of driving force for TTET.<sup>20</sup> Triplet energy transfer from both band edge and surface-trapped excitons has been observed in other semiconductor QD systems.<sup>55</sup> Nevertheless, while the surface-trapped intermediate provides a viable indirect triplet sensitization pathway in PbS-TPn, the thickest shell material displaying the highest relative QY for TTET proves that surface-trap-mediated TTET is not maximally efficient.

### 3.4 Conclusions

We have developed a library of TPn-functionalized PbS-CdS core-shell NCs with one PbS core and multiple CdS shell thicknesses ranging from 0 to 1.6 Cd-S bond lengths or 0 to 1 sulfur-to-sulfur interatomic spacings. The TA and PL data indicate the role of CdS shells in decreasing the rate of molecular triplet generation by increasing tunneling distance through the CdS shells and by passivating non-innocent PbS surface-traps. However, indirect triplet sensitization of TPn by PbS surface states, while viable, is less efficient than other TTET mechanisms from PbS NCs with higher PLQY before surface functionalization to append molecular chromophores.

### 3.5 Experimental Methods

#### 3.5.1 Quantum Dot Syntheses

Oleate-capped PbS NCs were synthesized for use as PbS-CdS core-shell precursors by adapting previously reported procedures.<sup>18, 20, 56</sup> The specific synthetic methods for obtaining PbS precursor sizes and their characterization have been reported in detail.<sup>20</sup> PbS-CdS core-shell NCs were synthesized from their respective PbS cores using previously reported cation exchange techniques.<sup>38, 42</sup> All core-shell NC experiments (ligand exchanges, spectroscopy, and materials characterization) were performed on a single synthetic batch to eliminate batch-to-batch inhomogeneity. TPn was synthesized and structurally characterized as published previously.<sup>41</sup>

#### 3.5.2 Ligand Exchange with TPn

The PbS-CdS core-shell NCs were subjected to well-established ligand exchange procedures.<sup>1, 18, 19, 21, 37, 40, 57, 58</sup> Briefly, oleate-capped NCs were suspended in toluene to which TPn was added to initiate 1:1 X-type ligand exchange<sup>40</sup> with the oleate ligands.

The NC-TPn hybrids were then purified by successive precipitation-centrifugation-resuspension and filtration steps. The average NC:TPn ratio was determined *via* UV-vis absorption spectroscopy. These values were found to be 1:17.3 for PbS-805-TPn, 1:24.1 for PbS-945-CdS-TPn, 1:28.1 for PbS-970-CdS-TPn, and 1:31.8 for PbS-1000-CdS-TPn for time resolved spectroscopy samples. Treating the PbS-CdS core-shell NCs as spheres to calculate their surface areas, these TPn loadings give bound TPn molecules/nm<sup>2</sup> values of 1.13, 1.12, 1.09, and 1.14, respectively. These molecular chromophore density estimates are essentially the same within the margin of experimental error. However, these values are less than those obtained in Chapter 2. The excited state dynamics for the PbS-805-TPn samples utilized in this study remained remarkably similar to the measurements observed for the higher surface density samples of the analogous material in Chapter 2. This suggests the surface loadings herein are sufficient to achieve similar conclusions about the photophysical processes in these constructs.

### *3.5.3 Static Spectroscopy*

Electronic absorption spectra were measured on a Shimadzu UV-3600 UV-vis-NIR spectrophotometer. Steady-state photoluminescence spectra were measured on an Edinburgh Instruments FS920 fluorescence spectrometer equipped with both a visible and a near-infrared photomultiplier tube. Excitation at 744 nm was achieved by a 450 W Xe arc lamp equipped with a monochromator and appropriate long pass filters.

### *3.5.4 Electron Microscopy*

Transmission Electron Microscopy (TEM) experiments were carried out using a JEM 2000FX Scanning TEM (JEOL). Images were acquired at an accelerating voltage of 200 kV. Samples were prepared by evaporation of dilute NC suspensions in toluene that

had been dropped onto an ultrathin carbon film on a lacey carbon support film on a 400 mesh Cu TEM grid. Size distributions were measured using ImageJ software (<https://imagej.nih.gov/ij/>). Particle sizing was done with the software's analyze particle function, after selection of an appropriate contrast threshold for the images. Scanning Electron Microscopy with Energy Dispersive X-ray Spectroscopy (SEM-EDS) was carried out on a FEI Verios 460L field-emission SEM (Thermo Fisher Scientific) equipped with a Si Drift Detector (Oxford Instruments). SEM-EDS samples were prepared by evaporation of dilute NC suspensions in toluene that had been dropped onto atomically smooth Si wafers.

### *3.5.5 Ultrafast Transient Absorption Spectroscopy*

Ultrafast transient absorption spectroscopy were performed using an amplified Ti:sapphire laser system described previously.<sup>20</sup> The PbS-CdS and PbS-CdS-TPn solutions were prepared to possess OD of approximately 0.08 at 744 nm. The ground state absorption spectra were taken before and after each experiment using an Agilent 8453 UV-visible spectrophotometer to ensure there was no sample decomposition.

### *3.5.6 Nanosecond Transient Absorption Spectroscopy*

Nanosecond TA measurements were executed using a LP920 spectrometer (Edinburgh Instruments) equipped with an iStar ICCD camera (Andor Technology), a visible light PMT, and an InGaAs photodiode for NIR detection. The excitation source was a tunable Vibrant 355 Nd:YAG/OPO system (OPOTEK) tuned to 744 nm (1 mJ/pulse, 5-7 ns fwhm). While this excitation power is sufficient to generate multiple excitons in PbS-CdS NCs, multiexciton processes such as biexciton and triexciton annihilation are expected to be significantly shorter-lived than the pulse duration (5-7 ns

fwhm). The excitation source operated at 1 Hz and 3.3 Hz for spectra and kinetics acquisitions, respectively. Appropriate long pass filters were used to remove residual leaking light from the excitation source. The samples were deaerated by a minimum of three freeze-pump-thaw degassing cycles. The PbS-CdS and PbS-CdS-TPn solutions were prepared to possess OD of approximately 0.08 at 744 nm.

### *3.5.7 Extracting Time Constants from Transient Absorption Difference Spectra*

Ultrafast transient absorption (TA) spectra were fit using a model based on the assumption that the time-resolved TA spectra of these hybrid materials can be linearly decomposed as the sum of time-independent decay-associated difference spectra (DADS) with specific time-dependent amplitudes.<sup>59</sup> Under this assumption, each DADS is therefore presumed to represent the TA spectrum of an individual excited state in the system. The time-dependent amplitudes correspond to the concentration or population of their respective DADS. In solving for these values from the PbS-CdS-TPn and PbS-805-TPn TA data, each DADS was assumed to interconvert to the next in a sequential, first order fashion.

Three DADS and an additional fitting parameter could model the complete ultrafast TA spectral datasets for all PbS-CdS-TPn and PbS-805-TPn materials studied. The additional fitting parameter, resembling a fourth DADS, is included in the model to account for a nonlinear response feature from the toluene occurring coincidentally with the impulse response function (IRF). The spectra produced by the model appear in Figures 3.5a-d. Additionally, the fits obtained from the model are compared to the experimental data at the end of the Supporting Information (Figures S3.9-S3.12). The

kinetic rate constants extracted from the model have been used to interpret the experimental data (Table 3.1).

### **3.6 Acknowledgments**

We acknowledge support for this work from the Organic Materials Chemistry program in the Air Force Office of Scientific Research (FA9550-18-1-0331). Electron microscopy was performed at the Analytical Instrumentation Facility (AIF) at North Carolina State University, which is supported by the State of North Carolina and the National Science Foundation (award number ECCS-1542015). The AIF is a member of the North Carolina Research Triangle Nanotechnology Network (RTNN), a site in the National Nanotechnology Coordinated Infrastructure (NNCI).

### 3.7 References

1. Mongin, C.; Garakyaraghi, S.; Razgoniaeva, N.; Zamkov, M.; Castellano, F. N., Direct observation of triplet energy transfer from semiconductor nanocrystals. *Science* **2016**, *351* (6271), 369-372.
2. Xia, P.; Raulerson, E. K.; Coleman, D.; Gerke, C. S.; Mangolini, L.; Tang, M. L.; Roberts, S. T., Achieving spin-triplet exciton transfer between silicon and molecular acceptors for photon upconversion. *Nature Chemistry* **2020**, *12* (2), 137-144.
3. Luo, X.; Han, Y. Y.; Chen, Z. W.; Li, Y. L.; Liang, G. J.; Liu, X.; Ding, T.; Nie, C. M.; Wang, M.; Castellano, F. N.; Wu, K. F., Mechanisms of triplet energy transfer across the inorganic nanocrystal/organic molecule interface. *Nature Communications* **2020**, *11* (1).
4. Yanai, N.; Kimizuka, N., New Triplet Sensitization Routes for Photon Upconversion: Thermally Activated Delayed Fluorescence Molecules, Inorganic Nanocrystals, and Singlet-to-Triplet Absorption. *Accounts of Chemical Research* **2017**, *50* (10), 2487-2495.
5. Lu, H.; Huang, Z.; Martinez, M. S.; Johnson, J. C.; Luther, J. M.; Beard, M. C., Transforming energy using quantum dots. *Energy & Environmental Science* **2020**, *13* (5), 1347-1376.
6. Wu, M.; Congreve, D. N.; Wilson, M. W. B.; Jean, J.; Geva, N.; Welborn, M.; Van Voorhis, T.; Bulovic, V.; Bawendi, M. G.; Baldo, M. A., Solid-state infrared-to-visible upconversion sensitized by colloidal nanocrystals. *Nature Photonics* **2016**, *10* (1), 31-34.
7. Okumura, K.; Mase, K.; Yanai, N.; Kimizuka, N., Employing Core-Shell Quantum Dots as Triplet Sensitizers for Photon Upconversion. *Chemistry-a European Journal* **2016**, *22* (23), 7721-7726.
8. Gray, V.; Xia, P.; Huang, Z.; Moses, E.; Fast, A.; Fishman, D. A.; Vullev, V. I.; Abrahamsson, M.; Moth-Poulsen, K.; Lee Tang, M., CdS/ZnS core-shell nanocrystal photosensitizers for visible to UV upconversion. *Chemical Science* **2017**, *8* (8), 5488-5496.
9. Mase, K.; Okumura, K.; Yanai, N.; Kimizuka, N., Triplet sensitization by perovskite nanocrystals for photon upconversion. *Chemical Communications* **2017**, *53* (59), 8261-8264.
10. Huang, Z.; Lee Tang, M., Semiconductor Nanocrystal Light Absorbers for Photon Upconversion. *The Journal of Physical Chemistry Letters* **2018**, *9* (21), 6198-6206.
11. Han, Y.; He, S.; Luo, X.; Li, Y.; Chen, Z.; Kang, W.; Wang, X.; Wu, K., Triplet Sensitization by "Self-Trapped" Excitons of Nontoxic CuInS<sub>2</sub> Nanocrystals for Efficient Photon Upconversion. *Journal of the American Chemical Society* **2019**, *141* (33), 13033-13037.
12. He, S.; Luo, X.; Liu, X.; Li, Y.; Wu, K., Visible-to-Ultraviolet Upconversion Efficiency above 10% Sensitized by Quantum-Confined Perovskite Nanocrystals. *The Journal of Physical Chemistry Letters* **2019**, *10* (17), 5036-5040.
13. Nienhaus, L.; Correa-Baena, J.-P.; Wieghold, S.; Einzinger, M.; Lin, T.-A.; Shulenberg, K. E.; Klein, N. D.; Wu, M.; Bulović, V.; Buonassisi, T.; Baldo,

- M. A.; Bawendi, M. G., Triplet-Sensitization by Lead Halide Perovskite Thin Films for Near-Infrared-to-Visible Upconversion. *ACS Energy Letters* **2019**, *4* (4), 888-895.
14. VanOrman, Z. A.; Bieber, A. S.; Wieghold, S.; Nienhaus, L., Green-to-Blue Triplet Fusion Upconversion Sensitized by Anisotropic CdSe Nanoplatelets. *Chemistry of Materials* **2020**.
  15. Jiang, Y.; Wang, C.; Rogers, C. R.; Kodaimati, M. S.; Weiss, E. A., Regio- and diastereoselective intermolecular [2+2] cycloadditions photocatalysed by quantum dots. **2019**, *11* (11), 1034-1040.
  16. Ravetz, B. D.; Pun, A. B.; Churchill, E. M.; Congreve, D. N.; Rovis, T.; Campos, L. M., Photoredox catalysis using infrared light via triplet fusion upconversion. *Nature* **2019**, *565* (7739), 343-346.
  17. Dexter, D. L., A THEORY OF SENSITIZED LUMINESCENCE IN SOLIDS. *Journal of Chemical Physics* **1953**, *21* (5), 836-850.
  18. Garakyaraghi, S.; Mongin, C.; Granger, D. B.; Anthony, J. E.; Castellano, F. N., Delayed Molecular Triplet Generation from Energized Lead Sulfide Quantum Dots. *Journal of Physical Chemistry Letters* **2017**, *8* (7), 1458-1463.
  19. Bender, J. A.; Raulerson, E. K.; Li, X.; Goldzak, T.; Xia, P.; Van Voorhis, T.; Tang, M. L.; Roberts, S. T., Surface States Mediate Triplet Energy Transfer in Nanocrystal-Acene Composite Systems. *Journal of the American Chemical Society* **2018**, *140* (24), 7543-7553.
  20. Papa, C. M.; Garakyaraghi, S.; Granger, D. B.; Anthony, J. E.; Castellano, F. N., TIPS-pentacene triplet exciton generation on PbS quantum dots results from indirect sensitization. *Chemical Science* **2020**, *11* (22), 5690-5696.
  21. Lu, H. P.; Chen, X. H.; Anthony, J. E.; Johnson, J. C.; Beard, M. C., Sensitizing Singlet Fission with Perovskite Nanocrystals. *Journal of the American Chemical Society* **2019**, *141* (12), 4919-4927.
  22. Wang, J.; Ding, T.; Nie, C.; Wang, M.; Zhou, P.; Wu, K., Spin-Controlled Charge-Recombination Pathways across the Inorganic/Organic Interface. *Journal of the American Chemical Society* **2020**, *142* (10), 4723-4731.
  23. Luo, X.; Liang, G.; Han, Y.; Li, Y.; Ding, T.; He, S.; Liu, X.; Wu, K., Triplet Energy Transfer from Perovskite Nanocrystals Mediated by Electron Transfer. *Journal of the American Chemical Society* **2020**.
  24. Kafle, T. R.; Kattel, B.; Yao, P.; Zereshki, P.; Zhao, H.; Chan, W.-L., Effect of the Interfacial Energy Landscape on Photoinduced Charge Generation at the ZnPc/MoS<sub>2</sub> Interface. *Journal of the American Chemical Society* **2019**, *141* (28), 11328-11336.
  25. Wieghold, S.; Nienhaus, L., Precharging Photon Upconversion: Interfacial Interactions in Solution-Processed Perovskite Upconversion Devices. *The Journal of Physical Chemistry Letters* **2020**, *11* (3), 601-607.
  26. Tian, Y.; Li, Y.; Chen, B.; Lai, R.; He, S.; Luo, X.; Han, Y.; Wei, Y.; Wu, K., Sensitized Molecular Triplet and Triplet Excimer Emission in Two-Dimensional Hybrid Perovskites. *The Journal of Physical Chemistry Letters* **2020**, *11* (6), 2247-2255.
  27. Bawendi, M. G.; Carroll, P. J.; Wilson, W. L.; Brus, L. E., LUMINESCENCE PROPERTIES OF CDSE QUANTUM CRYSTALLITES - RESONANCE

- BETWEEN INTERIOR AND SURFACE LOCALIZED STATES. *Journal of Chemical Physics* **1992**, *96* (2), 946-954.
28. Hasselbarth, A.; Eychmuller, A.; Weller, H., DETECTION OF SHALLOW ELECTRON TRAPS IN QUANTUM SIZED CDS BY FLUORESCENCE QUENCHING EXPERIMENTS. *Chemical Physics Letters* **1993**, *203* (2-3), 271-276.
  29. Nagpal, P.; Klimov, V. I., Role of mid-gap states in charge transport and photoconductivity in semiconductor nanocrystal films. *Nature Communications* **2011**, *2*.
  30. Voznyy, O.; Sargent, E. H., Atomistic Model of Fluorescence Intermittency of Colloidal Quantum Dots. *Physical Review Letters* **2014**, *112* (15).
  31. Krause, M. M.; Kambhampati, P., Linking surface chemistry to optical properties of semiconductor nanocrystals. *Physical Chemistry Chemical Physics* **2015**, *17* (29), 18882-18894.
  32. Kambhampati, P., On the kinetics and thermodynamics of excitons at the surface of semiconductor nanocrystals: Are there surface excitons? *Chemical Physics* **2015**, *446*, 92-107.
  33. Boles, M. A.; Ling, D.; Hyeon, T.; Talapin, D. V., The surface science of nanocrystals. *Nature Materials* **2016**, *15* (2), 141-153.
  34. Zhu, H. M.; Lian, T. Q., Wavefunction engineering in quantum confined semiconductor nanoheterostructures for efficient charge separation and solar energy conversion. *Energy & Environmental Science* **2012**, *5* (11), 9406-9418.
  35. Ding, T. N. X.; Olshansky, J. H.; Leone, S. R.; Alivisatos, A. P., Efficiency of Hole Transfer from Photoexcited Quantum Dots to Covalently Linked Molecular Species. *Journal of the American Chemical Society* **2015**, *137* (5), 2021-2029.
  36. Li, A.; Zhu, W.; Li, C.; Wang, T.; Gong, J., Rational design of yolk-shell nanostructures for photocatalysis. *Chemical Society Reviews* **2019**.
  37. Huang, Z.; Xu, Z.; Mahboub, M.; Li, X.; Taylor, J. W.; Harman, W. H.; Lian, T.; Tang, M. L., PbS/CdS Core-Shell Quantum Dots Suppress Charge Transfer and Enhance Triplet Transfer. *Angewandte Chemie-International Edition* **2017**, *56* (52), 16583-16587.
  38. Mahboub, M.; Huang, Z. Y.; Tang, M. L., Efficient Infrared-to-Visible Upconversion with Subsolar Irradiance. *Nano Letters* **2016**, *16* (11), 7169-7175.
  39. Mahboub, M.; Xia, P.; Van Baren, J.; Li, X.; Lui, C. H.; Tang, M. L., Midgap States in PbS Quantum Dots Induced by Cd and Zn Enhance Photon Upconversion. *Acs Energy Letters* **2018**, *3* (4), 767-772.
  40. Kroupa, D. M.; Arias, D. H.; Blackburn, J. L.; Carroll, G. M.; Granger, D. B.; Anthony, J. E.; Beard, M. C.; Johnson, J. C., Control of Energy Flow Dynamics between Tetracene Ligands and PbS Quantum Dots by Size Tuning and Ligand Coverage. *Nano Letters* **2018**, *18* (2), 865-873.
  41. Li, Z.; Shankar, K.; Mor, G. K.; Grimminger, R. A.; Lin, C.-M.; Anthony, J. E.; Grimes, C. A., Functionalized pentacenes for dye-sensitized solar cells. *Journal of Photonics for Energy* **2011**, *1*.
  42. Justo, Y.; Geiregat, P.; Van Hoecke, K.; Vanhaecke, F.; Donega, C. D.; Hens, Z., Optical Properties of PbS/CdS Core/Shell Quantum Dots. *Journal of Physical Chemistry C* **2013**, *117* (39), 20171-20177.

43. Pietryga, J. M.; Werder, D. J.; Williams, D. J.; Casson, J. L.; Schaller, R. D.; Klimov, V. I.; Hollingsworth, J. A., Utilizing the lability of lead selenide to produce heterostructured nanocrystals with bright, stable infrared emission. *Journal of the American Chemical Society* **2008**, *130* (14), 4879-4885.
44. Lambert, K.; De Geyter, B.; Moreels, I.; Hens, Z., PbTeCdTe CoreShell Particles by Cation Exchange, a HR-TEM study. *Chemistry of Materials* **2009**, *21* (5), 778-+.
45. Moreels, I.; Lambert, K.; Smeets, D.; De Muynck, D.; Nollet, T.; Martins, J. C.; Vanhaecke, F.; Vantomme, A.; Delerue, C.; Allan, G.; Hens, Z., Size-Dependent Optical Properties of Colloidal PbS Quantum Dots. *Acs Nano* **2009**, *3* (10), 3023-3030.
46. Klimov, V. I., Spectral and dynamical properties of multilexcitons in semiconductor nanocrystals. In *Annual Review of Physical Chemistry*, 2007; Vol. 58, pp 635-673.
47. Cho, B.; Peters, W. K.; Hill, R. J.; Courtney, T. L.; Jonas, D. M., Bulklike Hot Carrier Dynamics in Lead Sulfide Quantum Dots. *Nano Letters* **2010**, *10* (7), 2498-2505.
48. Yang, Y.; Rodriguez-Cordoba, W.; Lian, T., Ultrafast Charge Separation and Recombination Dynamics in Lead Sulfide Quantum Dot-Methylene Blue Complexes Probed by Electron and Hole Intraband Transitions. *Journal of the American Chemical Society* **2011**, *133* (24), 9246-9249.
49. Bublitz, G. U.; Boxer, S. G., Stark spectroscopy: Applications in chemistry, biology, and materials science. *Annual Review of Physical Chemistry* **1997**, *48*, 213-242.
50. Ardo, S.; Sun, Y.; Castellano, F. N.; Meyer, G. J., Excited-State Electron Transfer from Ruthenium-Polypyridyl Compounds to Anatase TiO<sub>2</sub> Nanocrystallites Evidence for a Stark Effect. *Journal of Physical Chemistry B* **2010**, *114* (45), 14596-14604.
51. Huang, Z.; Xu, Z.; Mahboub, M.; Liang, Z.; Jaimes, P.; Xia, P.; Graham, K. R.; Tang, M. L.; Lian, T., Enhanced Near-Infrared-to-Visible Upconversion by Synthetic Control of PbS Nanocrystal Triplet Photosensitizers. *Journal of the American Chemical Society* **2019**, *141* (25), 9769-9772.
52. Xu, Z.; Huang, Z.; Li, C.; Huang, T.; Evangelista, F. A.; Tang, M. L.; Lian, T., Tuning QD/mediator Interface for Optimal Efficiency of Quantum Dot Sensitized Near Infrared to Visible Photon Upconversion Systems. *ACS Applied Materials & Interfaces* **2020**.
53. Zhu, H.; Song, N.; Lian, T., Controlling Charge Separation and Recombination Rates in CdSe/ZnS Type I Core-Shell Quantum Dots by Shell Thicknesses. *Journal of the American Chemical Society* **2010**, *132* (42), 15038-15045.
54. Gray, V.; Allardice, J. R.; Zhang, Z.; Dowland, S.; Xiao, J.; Petty, A. J.; Anthony, J. E.; Greenham, N. C.; Rao, A., Direct vs Delayed Triplet Energy Transfer from Organic Semiconductors to Quantum Dots and Implications for Luminescent Harvesting of Triplet Excitons. *ACS Nano* **2020**, *14* (4), 4224-4234.
55. Rigsby, E. M.; Lee, K.; Sun, J.; Fishman, D. A.; Tang, M. L., Primary amines enhance triplet energy transfer from both the band edge and trap state from CdSe nanocrystals. *The Journal of Chemical Physics* **2019**, *151* (17), 174701.

56. Hines, M. A.; Scholes, G. D., Colloidal PbS nanocrystals with size-tunable near-infrared emission: Observation of post-synthesis self-narrowing of the particle size distribution. *Advanced Materials* **2003**, *15* (21), 1844-1849.
57. Mongin, C.; Moroz, P.; Zamkov, M.; Castellano, F. N., Thermally activated delayed photoluminescence from pyrenyl-functionalized CdSe quantum dots. *Nature Chemistry* **2018**, *10* (2), 225-230.
58. La Rosa, M.; Denisov, S. A.; Jonusauskas, G.; McClenaghan, N. D.; Credi, A., Designed Long-Lived Emission from CdSe Quantum Dots through Reversible Electronic Energy Transfer with a Surface-Bound Chromophore. *Angewandte Chemie-International Edition* **2018**, *57* (12), 3104-3107.
59. van Wilderen, L. J. G. W.; Lincoln, C. N.; van Thor, J. J., Modelling Multi-Pulse Population Dynamics from Ultrafast Spectroscopy. *PLOS ONE* **2011**, *6* (3), e17373.

### 3.8 Supporting Information

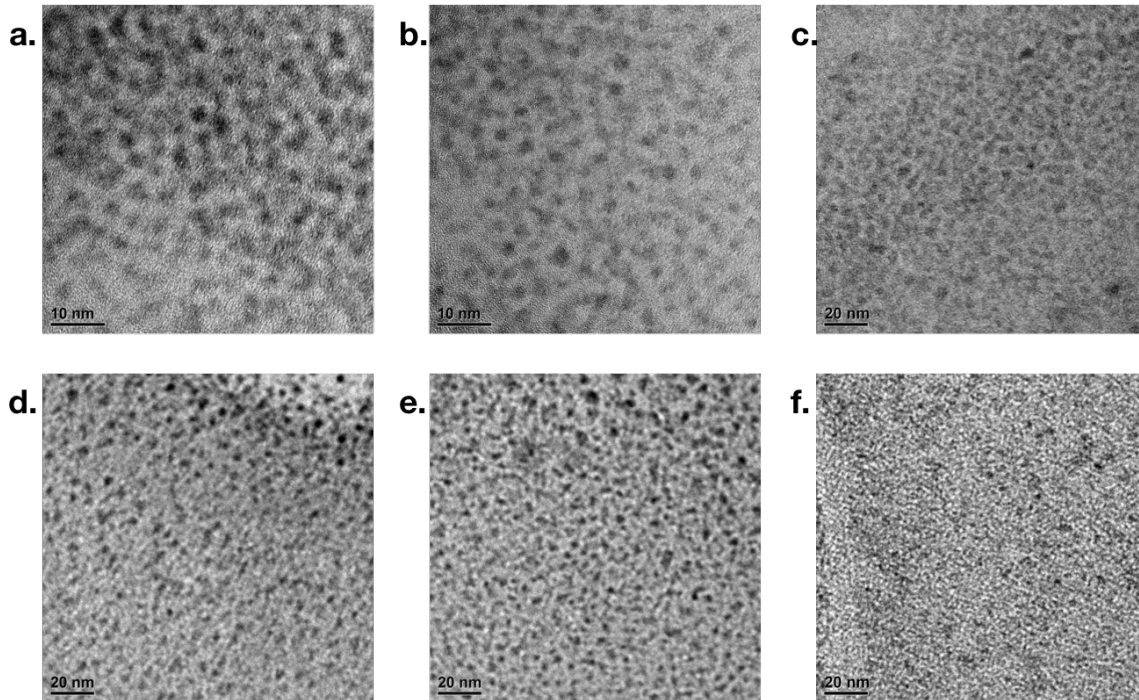


**Figure S3.1** TEM images of PbS parent NCs with average diameters of **(a)**  $3.0 \pm 0.5$  nm, **(b)**  $2.9 \pm 0.5$  nm, **(c)**  $2.6 \pm 0.4$  nm, and PbS-CdS core-shell NCs with average diameters of **(d)**  $3.0 \pm 0.5$  nm, **(e)**  $2.9 \pm 0.5$  nm, and **(f)**  $2.6 \pm 0.4$  nm.

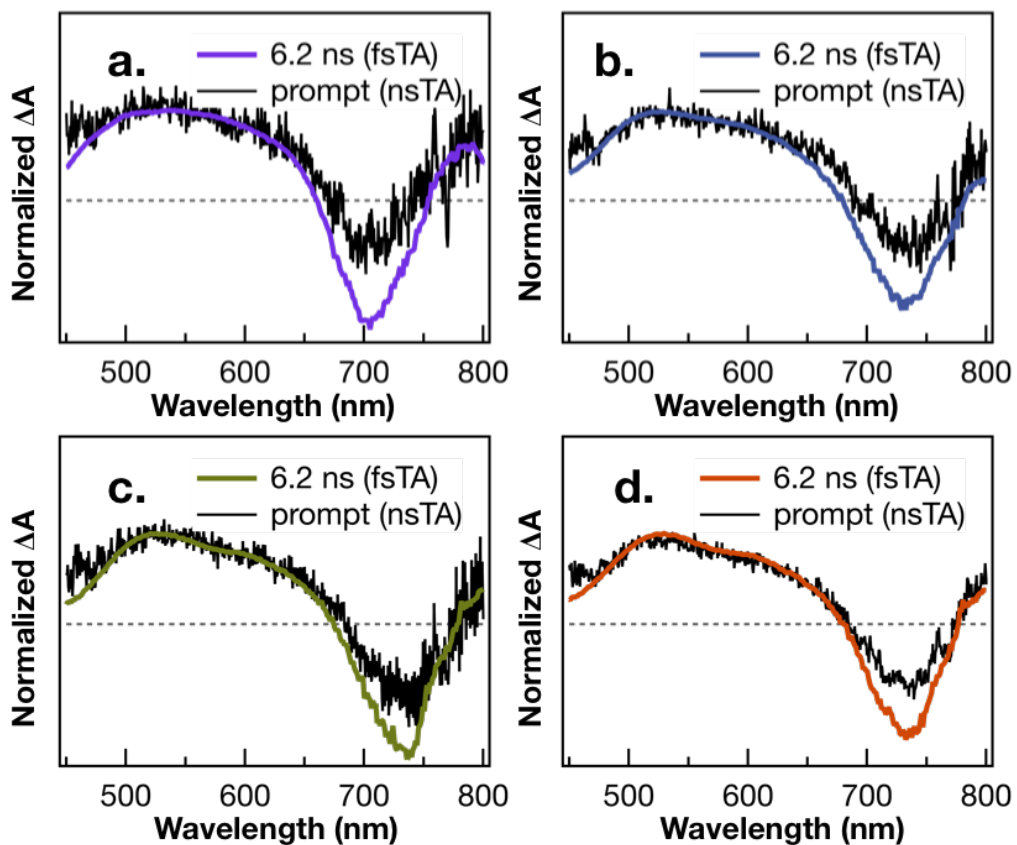


**Figure S3.2** Comparison of normalized, ultrafast (0.15  $\mu\text{J}/\text{pulse}$ , 100 fs fwhm, 744 nm) TA difference spectra (colored) and normalized, nanosecond (1.0 mJ/pulse, 5 ns fwhm, 744 nm) TA difference spectra (black) of PbS-CdS core-shell nanocrystal suspensions in toluene following pulsed laser excitation. The spectra correspond to **(a)** PbS-805, **(b)** PbS-945-CdS, **(c)** PbS-970-CdS, and **(d)** PbS-1000-CdS. Time delays are prompt for the nanosecond TA spectra and 6.2 ns for the ultrafast TA spectra.

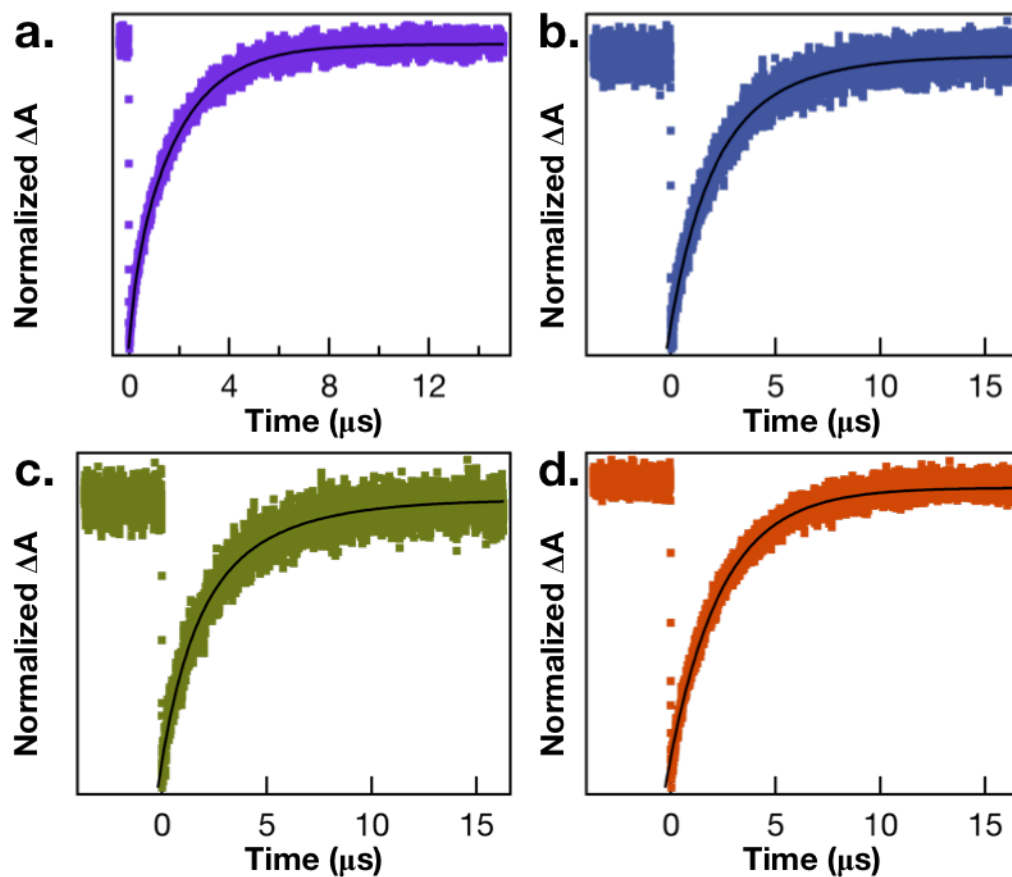


**Figure S3.3** Nanosecond TA kinetics of (a) PbS-805, (b) PbS-945-CdS, (c) PbS-970-CdS, and (d) PbS-1000-CdS in toluene following pulsed excitation at 744 nm (1.0 mJ/pulse, 5 ns fwhm). The decays of the PbS first exciton bleach monitored at 720 nm for each species can be fit by exponential functions (black lines) with a time constant of  $2.42 \pm 0.07 \mu s$ .

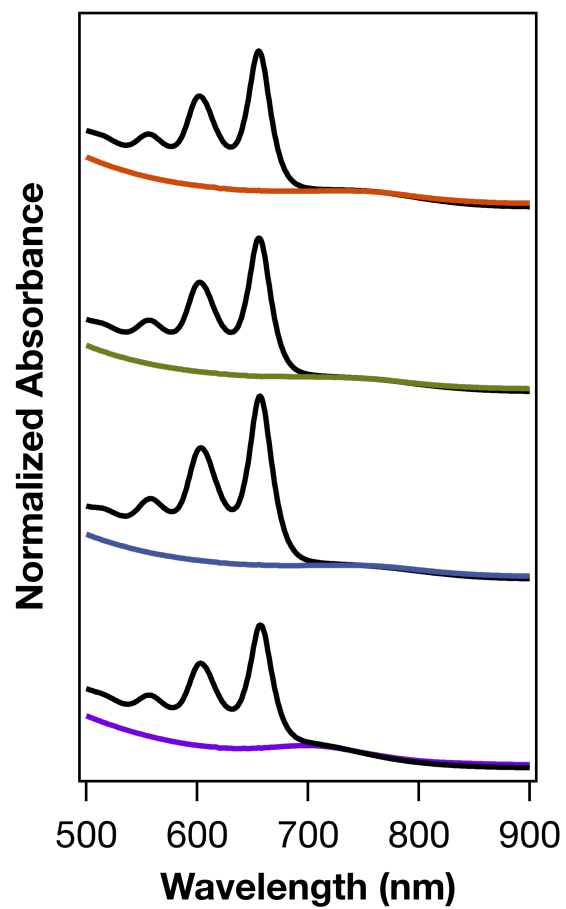


**Figure S3.4** Electronic absorption spectra of PbS-1000-CdS (orange, top), PbS-970-CdS (green), PbS-945-CdS (blue), PbS-805 (violet, bottom), and their corresponding PbS-CdS-TPn hybrid materials (black lines, matching y-axis offset indicates matching NC size).

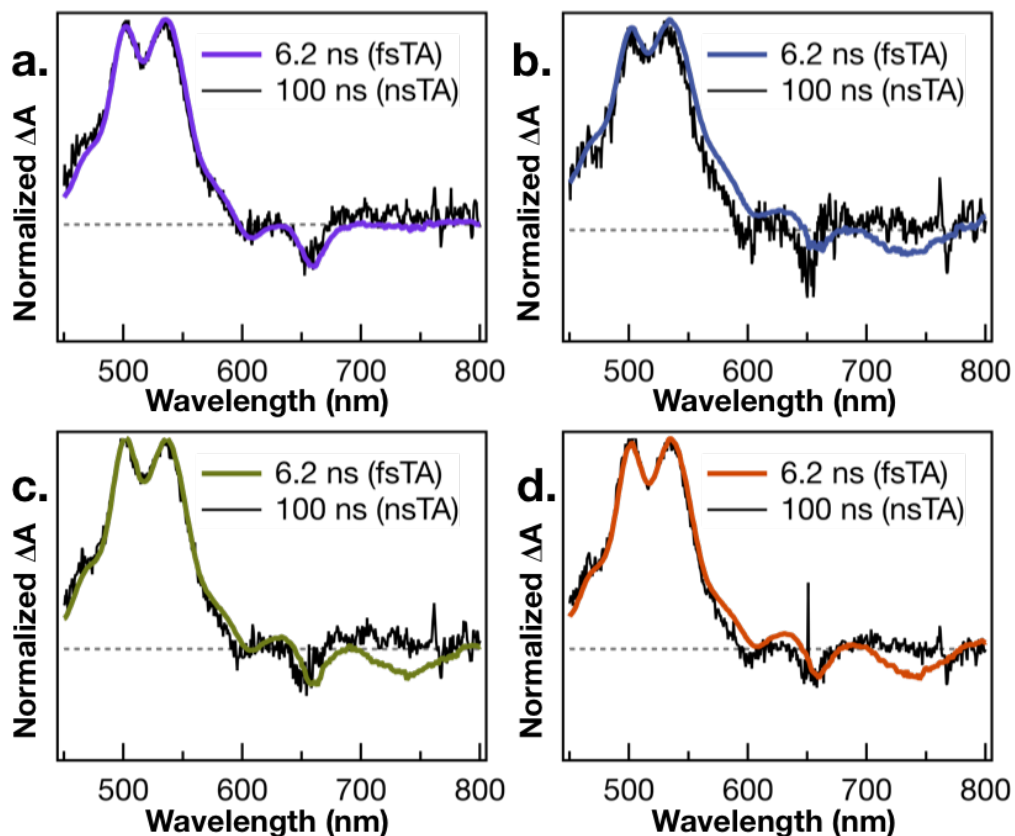


**Figure S3.5** Comparison of normalized, ultrafast (0.15  $\mu\text{J}/\text{pulse}$ , 100 fs fwhm) TA difference spectra (colored) and normalized, nanosecond (1.0 mJ/pulse, 5 ns fwhm) TA difference spectra (black) of PbS-CdS-TPn core-shell hybrid material suspensions in toluene following 744 nm pulsed laser excitation. The spectra correspond to **(a)** PbS-805-TPn, **(b)** PbS-945-CdS-TPn, **(c)** PbS-970-CdS-TPn, and **(d)** PbS-1000-CdS-TPn. Time delays are 6.2 ns for the ultrafast TA spectra and 100 ns for the nanosecond TA spectra.

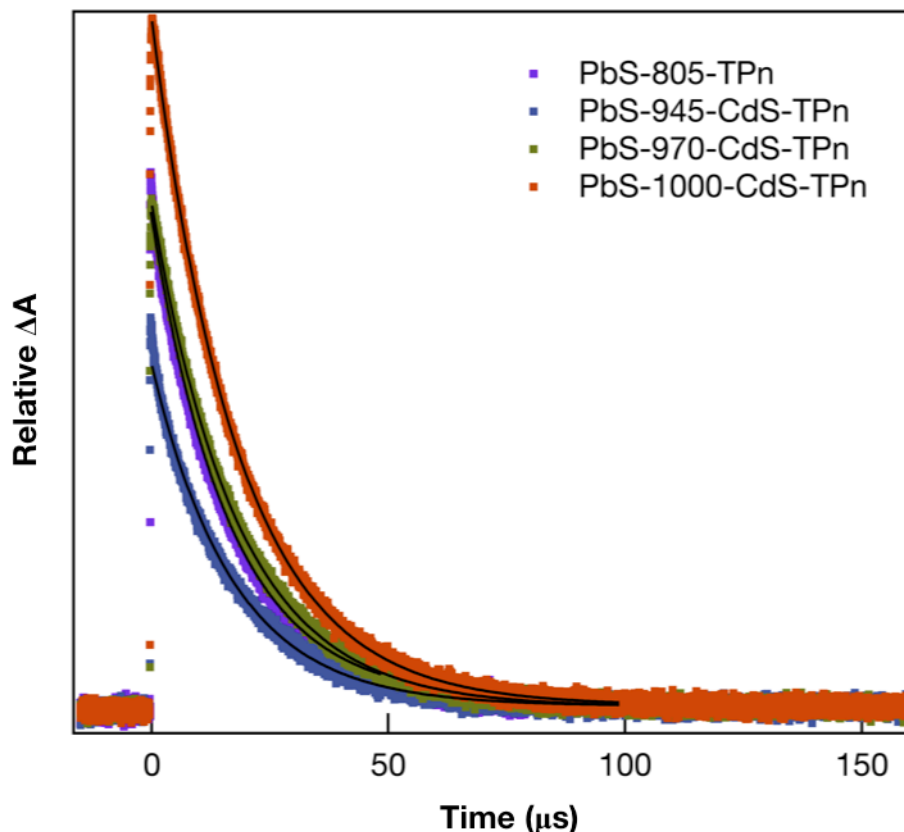


**Figure S3.6** Nanosecond TA kinetics of PbS-CdS-TPn core-shell and PbS-805-TPn nanocrystal-molecule hybrid materials suspended in toluene following pulsed excitation at 744 nm (1.0 mJ/pulse, 5 ns fwhm). The decays of the <sup>3</sup>TPn feature observed at 534 nm are fit by monoexponential functions (black lines) with time constants given in Table S3.1.

**Table S3.1** Decay constants obtained from fitting monoexponential functions to TA kinetics of PbS-CdS-TPn core-shell nanocrystal-molecule hybrid materials suspended in toluene following pulsed excitation at 744 nm (1.0 mJ/pulse, 5 ns fwhm). Kinetic traces ( $\lambda_{\text{probe}} = 534 \text{ nm}$ ) are displayed in Fig. S3.6.

	$\tau$ ( $\mu\text{s}$ )
<b>PbS-805-TPn</b>	$16.3 \pm 0.3$
<b>PbS-945-CdS-TPn</b>	$17.1 \pm 0.4$
<b>PbS-970-CdS-TPn</b>	$18.1 \pm 0.2$
<b>PbS-1000-CdS-TPn</b>	$18.3 \pm 0.2$

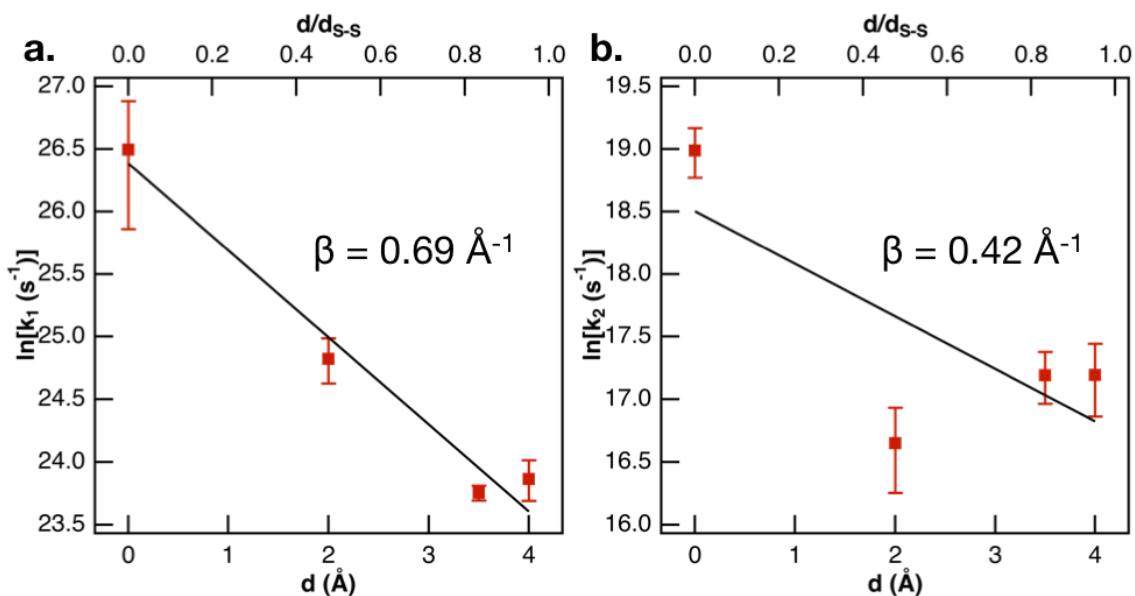


**Figure S3.7** Logarithm of extracted rate constants for **(a)** hole trapping in the PbS cores,  $k_1$ , and **(b)** the formation of  $^3\text{TPn}$ ,  $k_2$ , plotted as a function of CdS shell thickness. As noted in the text,  $k_2$  values were normalized by the number of TPn molecules on the surface. Error bars represent the standard error calculated from three independent measurements.

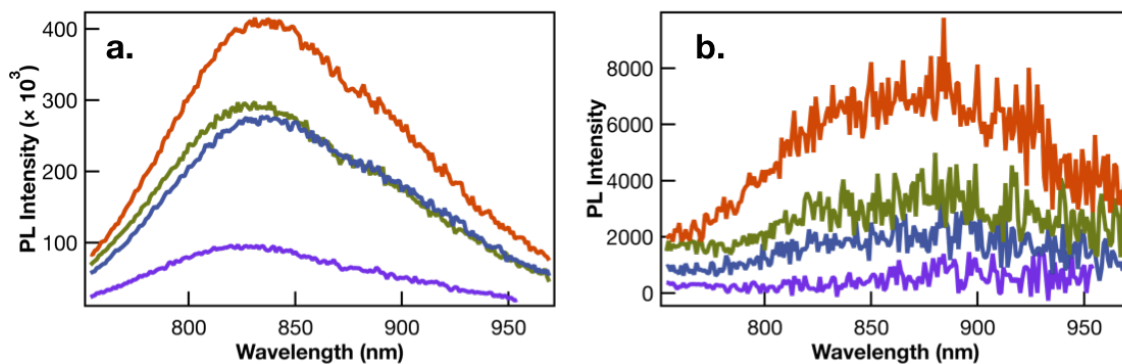


**Figure S3.8** Absorbance-matched emission spectra for **(a)** PbS-CdS NCs and **(b)** PbS-CdS-TPn materials suspended in toluene after 744 nm excitation. Quenching efficiencies range from 98% for PbS-1000-CdS-TPn (orange traces) to >99% for PbS-805-TPn (purple traces).

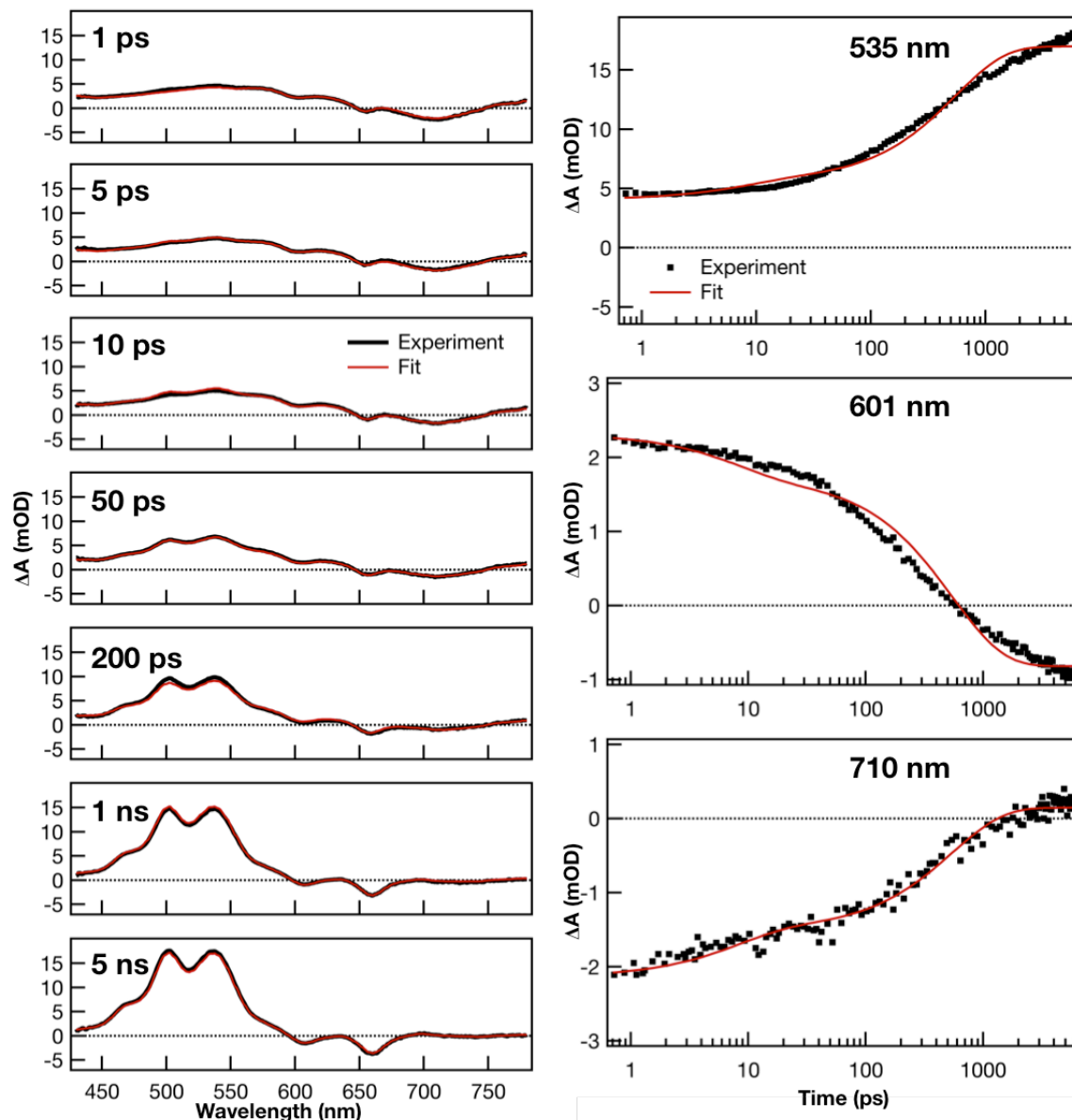


**Figure S3.9** Experimental PbS-805-TPn ultrafast TA spectra (black) probed in the visible region of the electromagnetic spectrum compared to the fit modeled by linear decomposition (red). Three DADS were necessary to reproduce the changes in the spectra. Time constants for first-order interconversion between the DADS were found to be 4.0 ps and 0.36 ns as described in the main text. This sample was absorbance matched at excitation to the PbS-CdS-TPn materials.

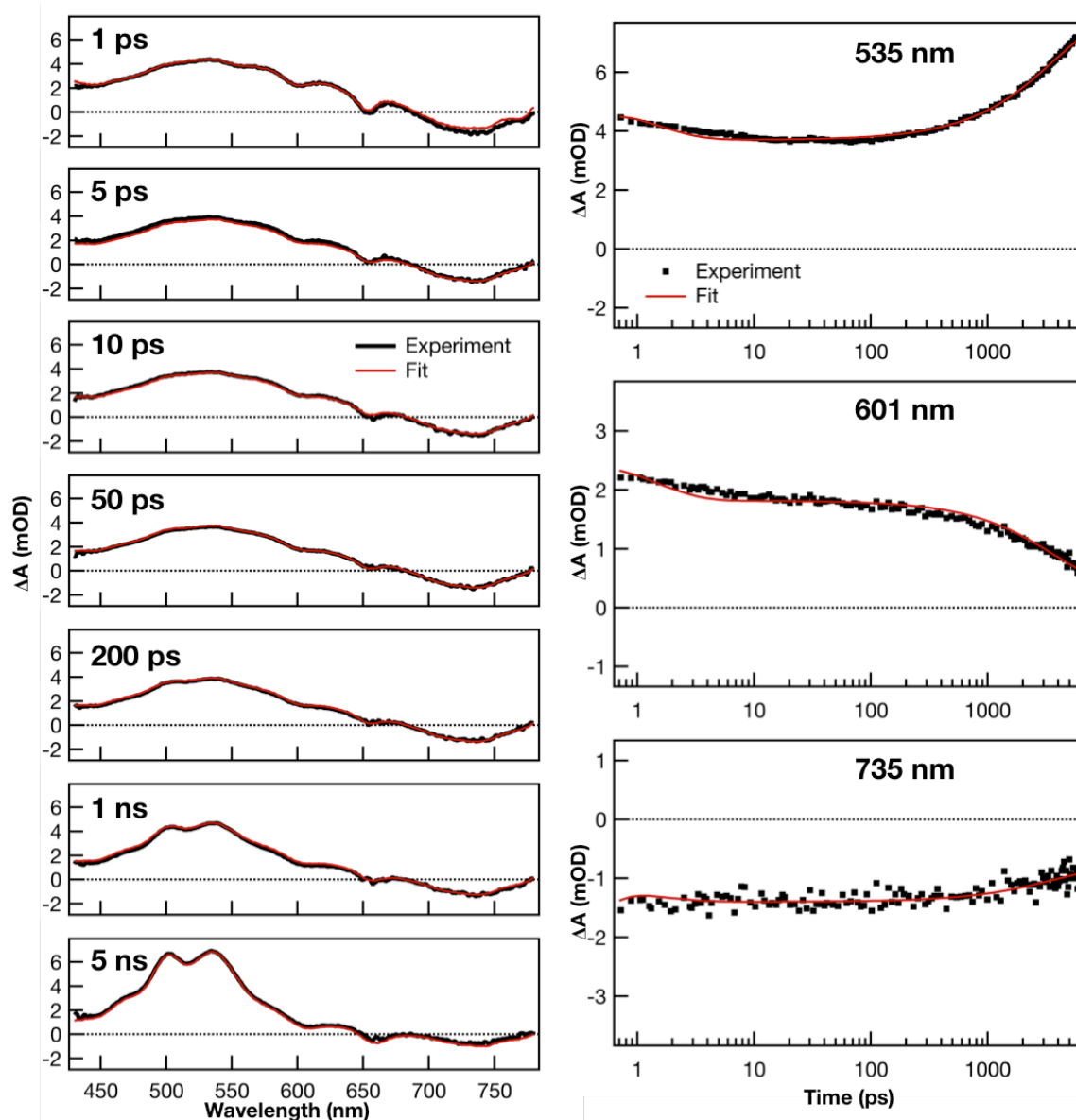


**Figure S3.10** Experimental PbS-945-CdS-TPn ultrafast TA spectra (black) probed in the visible region of the electromagnetic spectrum compared to the fit modeled by linear decomposition (red). Three DADS were necessary to reproduce the changes in the spectra. Time constants for first-order interconversion between the DADS were found to be 17 ps and 3.1 ns as described in the main text.

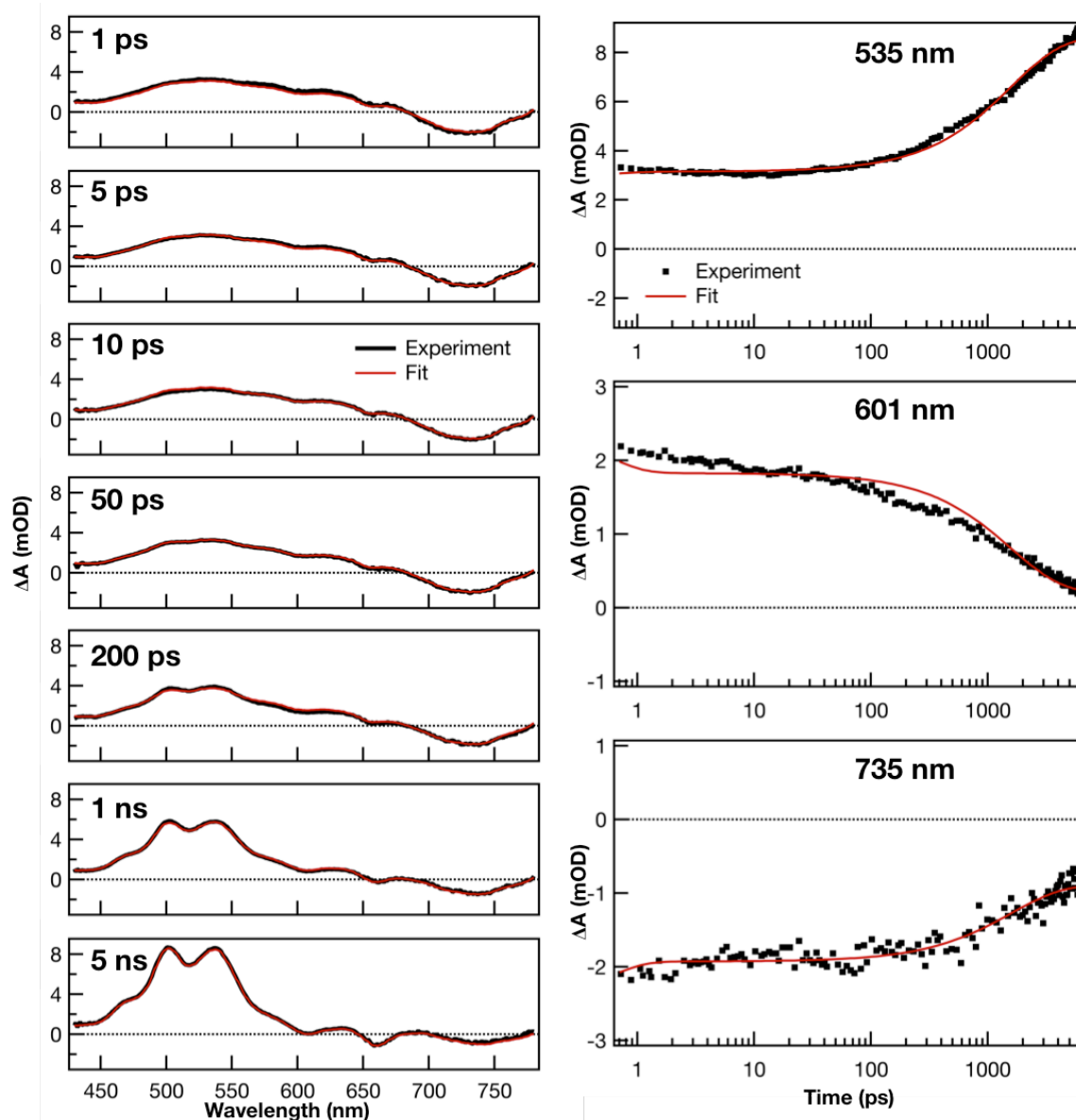


**Figure S3.11** Experimental PbS-970-CdS-TPn ultrafast TA spectra (black) probed in the visible region of the electromagnetic spectrum compared to the fit modeled by linear decomposition (red). Three DADS were necessary to reproduce the changes in the spectra. Time constants for first-order interconversion between the DADS were found to be 48 ps and 2.2 ns as described in the main text.

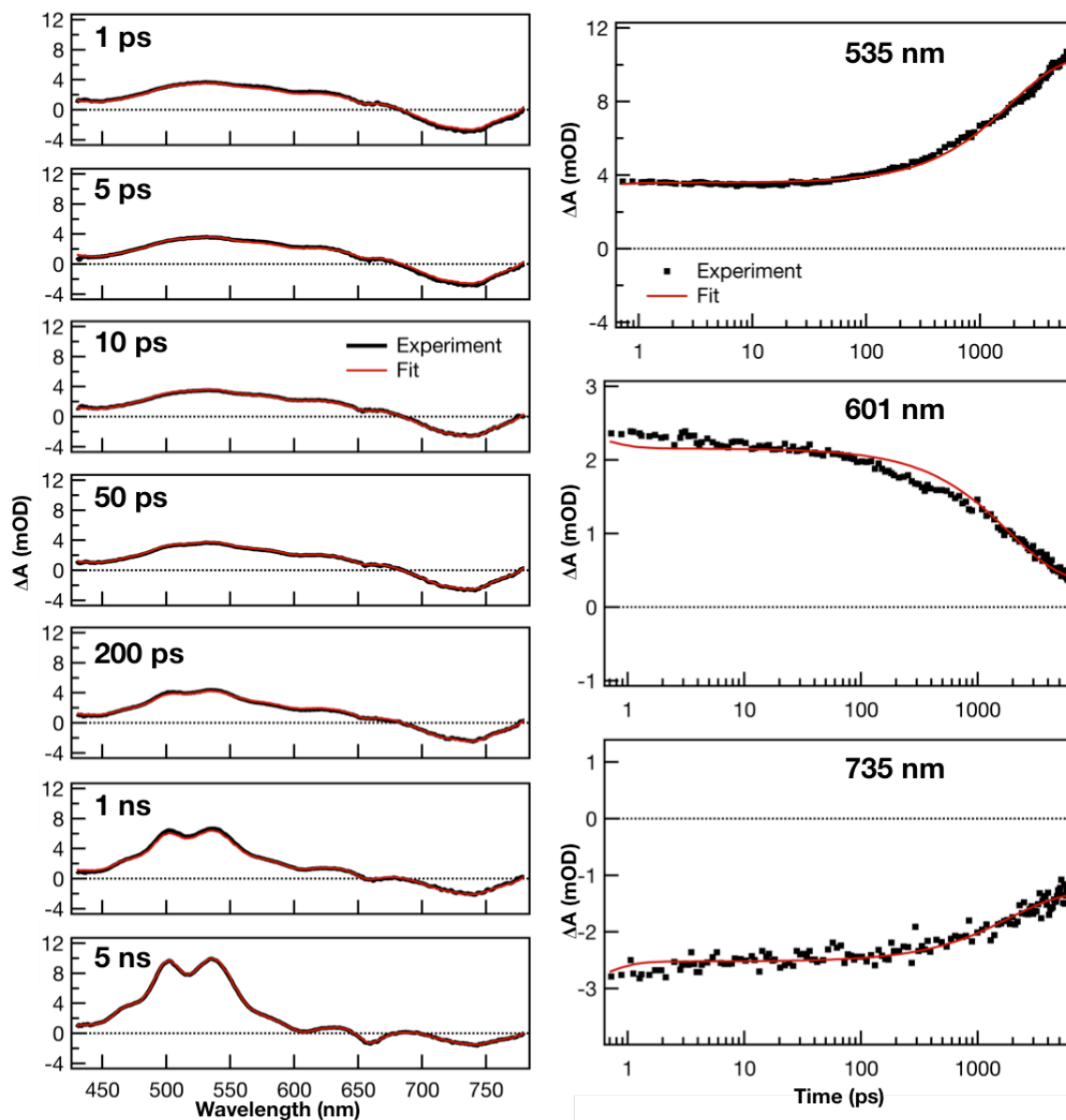


**Figure S3.12** Experimental PbS-1000-CdS-TPn ultrafast TA spectra (black) probed in the visible region of the electromagnetic spectrum compared to the fit modeled by linear decomposition (red). Three DADS were necessary to reproduce the changes in the spectra. Time constants for first-order interconversion between the DADS were found to be 44 ps and 2.5 ns as described in the main text.

## CHAPTER 4: Förster Resonance Energy Transfer from Colloidal Perovskite Nanoplatelets

### 4.1 Abstract

Since 2014, synthetic methods have been developed to obtain colloidally stable metal halide perovskite nanomaterials as nanocrystals or nanoplatelets. Due to their strong quantum confinement effects, perovskite nanoplatelets have extremely desirable optical properties for utilization as photosensitizers. In this study, a scheme was devised to associate molecular chromophore surfactants with the nanoplatelet surface in order to interrogate the nature of energy transfer across the nanoplatelet-molecule interface. The molecule selected was a functionalized derivative of 4-(1-piperidinylnaphthalene-1,8-dicarboximide (PNI). The functionalized PNI surfactant was successfully synthesized and appended to the nanoplatelet surface in an unexpectedly wide range of surface loadings. Photophysical investigation suggests that the PNI surfactants are maintained in close proximity to the nanoplatelet surface. Time-resolved photoluminescence experiments provide the strongest evidence to date of dipolar Förster resonance energy transfer (FRET) from colloidal perovskite nanomaterials to molecules.

### 4.2 Introduction

In the last half-decade, new syntheses have been reported for colloidal perovskite nanocrystals and nanoplatelets. The nanocrystal work has mostly focused on cubic nanocrystals. These nanocrystals typically have side lengths greater than 4 nm.<sup>1,2</sup> The long chain surfactants used in the synthesis serve dual purposes, controlling the nanocrystal size and imparting colloidal stability to the nanocrystal. Hot-injection nanocrystal syntheses report photoluminescence (PL) quantum yields (QY) in the range

of 50–90%. Furthermore, their PL maximum can easily be tuned across the entire visible range of the electromagnetic spectrum. As an example of facile tuning of the emission, CsPbX<sub>3</sub> nanocrystals can even be post-synthetically tuned *via* simple anion exchange reactions.<sup>3</sup> At greater than 4 nm, the nanocrystals show signs of quantum confinement, but they are weak,<sup>4</sup> and as a result, the nanocrystals display absorption and PL properties that are more characteristic of the bulk semiconductor.

Metal halide perovskite nanoplatelets, which are quantum confined in one dimension, can be described using the formula L<sub>2</sub>BX<sub>4</sub>, where L represents a long chain alkyl ammonium cation that both inhibits the growth of the nanoplatelet in one dimension during synthesis, being too large to fit inside the unit cell and gives the nanoplatelet colloidal stability in solution.<sup>5</sup> As the nanoplatelets are only a few atoms thick in the confined dimension, the degree of quantum confinement is significantly greater than any in an equivalent nanocrystal, cubic or quasi-spherical. This stronger confinement regime begets desirable absorption and PL homogeneity, remarkably narrow absorption and PL spectral features, small Stokes shifts, and thickness-dependent absorption and PL energies which can blue-shift from those of the bulk material by approximately 0.6 eV.<sup>6</sup>

Recall from Chapter 1 that photoinduced energy transfer proceeds by two principal pathways. One is Förster resonance energy transfer, or FRET, which requires strong spectral overlap of donor emission and acceptor absorption.<sup>7</sup> FRET usually proceeds from a donor in a singlet excited state and generates a singlet excited state on the acceptor. The other mechanism is Dexter energy transfer. It proceeds by a simultaneous, concerted exchange of two electrons that depends on the wavefunction overlap between donor and acceptor.<sup>8</sup> The implication of the correlated electron transfer

mechanism is that Dexter-like processes can proceed from donor triplet excited states and successfully generate a triplet excited state on the acceptor – triplet-triplet energy transfer (TTET). The project in this Chapter was undertaken when it was realized that metal halide perovskite nanoplatelets had the potential be utilized in any number of singlet or triplet excited state photophysical processes.

### 4.3 Experimental Section

#### 4.3.1 Abbreviations & Materials

In order to more easily communicate regarding the composition of the nanoplatelets, we use the following abbreviations throughout for different chemical species. Lead = Pb, bromide = Br, butylammonium = BA, hexylammonium = HA, octylammonium = OA, *N*-(ethyl-2-ammonium)-4-(1-piperidinylnaphthalene-1,8-dicarboximide = PNI.

The following chemicals and all solvents were purchased from commercial vendors and used without further purification.

**Inorganic salts.** lead (II) bromide ( $\text{PbBr}_2$ ) (Alfa Aesar, 99.999%), sodium chloride ( $\text{NaCl}$ ) (BDH,  $\geq 99\%$ ), sodium sulfate ( $\text{Na}_2\text{SO}_4$ ) (BDH, anhydrous,  $\geq 99\%$ ), magnesium sulfate ( $\text{MgSO}_4$ ) (BDH, anhydrous,  $\geq 98\%$ ), sodium hydroxide ( $\text{NaOH}$ ) (MilliporeSigma, 99-100%).

**Other chemicals.** hydrobromic acid ( $\text{HBr}$ ) (BDH, 48%), 1-butylamine (Alfa Aesar, 99%), hexylamine (MilliporeSigma, 99%), 1-octylamine (Alfa Aesar, 99%), ethylenediamine (Alfa Aesar, 99%), piperidine (MilliporeSigma, 99%), di-*tert*-butyl dicarbonate ( $\text{Boc}_2\text{O}$ ) (MilliporeSigma, 99%), 4-nitronaphthalene-1,8-dicarboxyanhydride (MilliporeSigma, 95%).

#### 4.3.2 Synthetic Methods

**Alkyl ammonium bromide precursor salt preparation.** The optically inert alkyl ammonium bromide precursor salts were prepared using adaptations of literature procedures.<sup>5</sup> A general synthetic approach is given here. The alkyl amine species (42 mmol) were added to a single-neck round bottom flask containing ethanol (50 mL). This flask was placed into a room temperature water bath. A slight excess of hydrobromic acid (45 mmol) was then added dropwise to the solution while stirring. The reaction proceeded for 2 hours under ambient conditions and at room temperature. The solvent was removed by rotary evaporation, leaving behind the salt as a solid. The salts were washed several times with diethyl ether (at least 3 washes for all salts and butylammonium bromide was washed until it no longer had an orange color). The precursor salts were collected as a white powder in all three cases.

***tert*-butyl-2-aminoethylcarbamate.** The synthesis of this compound was adapted from a literature procedure.<sup>9</sup> A solution of Boc<sub>2</sub>O (1.44 g, 6.6 mmol) in 10 mL anhydrous THF was added drop wise to 10 mL of 3 M ethylenediamine in THF at 0°C. After the reaction proceeded for 30 min at 0°C, the reaction mixture was removed from the ice bath and allowed to react overnight as the reaction temperature returned to room temperature. The THF was removed by rotary evaporation and the remaining oil was dissolved in 20 mL CH<sub>2</sub>Cl<sub>2</sub>. This mixture was washed with water three times followed by two washes of the aqueous layer with additional CH<sub>2</sub>Cl<sub>2</sub>. The recombined CH<sub>2</sub>Cl<sub>2</sub> solution was washed twice with NaCl brine and dried over Na<sub>2</sub>SO<sub>4</sub> for 2 h before being rotary evaporated to a cloudy oily liquid. The title compound was obtained in 41% yield and used without further purification. <sup>1</sup>H NMR (CDCl<sub>3</sub>): δ 4.89 (s, 1H), 3.21 (s, broad), 3.15 (m, 2H), 2.78

(t, 2H), 1.30 (s, 9H). Selected FT-IR (ATR): 3500-3000  $\text{cm}^{-1}$  (aliphatic primary amine N-H stretches), 3000-2750  $\text{cm}^{-1}$  (aliphatic C-H stretches), 1683  $\text{cm}^{-1}$  (primary amide C=O stretch).

***N*-(*tert*-butyl-2-aminoethylcarbamate)-4-nitronaphthalene-1,8-dicarboximide.** This compound and the following were prepared in a manner similar to a previously published method for a closely related molecule.<sup>10</sup> *tert*-butyl *N*-(2-aminoethyl)-carbamate (429 mg, 2.68 mmol) and 4-nitronaphthalene-1,8-dicarboxyanhydride (652 mg, 2.68 mmol) were refluxed in absolute ethanol for 48 h. The solution was then cooled to 4°C overnight and some solid formed in the reaction flask. Further precipitation was induced by the addition of 0°C petroleum ether. The yellow crystals were collected by vacuum filtration on a glass frit and rinsed with 0°C petroleum ether and ethanol. The title compound was obtained in 71% yield and used without further purification. <sup>1</sup>H NMR ( $\text{CDCl}_3$ ):  $\delta$  8.84 (d, 1H), 8.74 (d, 1H), 8.70 (d, 1H), 8.40 (d, 1H), 7.98 (dd, 1H), 4.84 (m, 1H), 4.36 (t, 2H), 3.55 (m, 2H), 1.29 (s, 9H). Selected FT-IR (ATR): 3500-3000  $\text{cm}^{-1}$  (aliphatic primary amine N-H stretches), 3111  $\text{cm}^{-1}$  (naphthalene C-H), 3000-2750  $\text{cm}^{-1}$  (aliphatic C-H stretches), 1703  $\text{cm}^{-1}$  (imide C=O stretch), 1687  $\text{cm}^{-1}$  (primary amide C=O stretch), 1662  $\text{cm}^{-1}$  (imide C=O stretch), 1514  $\text{cm}^{-1}$  (nitro N-O stretch).

***N*-(*tert*-butyl-2-aminoethylcarbamate)-4-(1-piperidinyl)naphthalene-1,8-dicarboximide (PN1enBoc).** A refluxing solution of *N*-(*tert*-butyl *N'*-(2-aminoethyl)-carbamate)-4-nitronaphthalene-1,8-dicarboximide (729 mg, 1.89 mmol) in 17 mL anhydrous DMF darkened immediately upon the addition of piperidine (928  $\mu\text{L}$ , 9.40 mmol). The solution was refluxed for 2 h and subsequently cooled to room temperature.

The cooled reaction mixture was diluted with 100 mL CH<sub>2</sub>Cl<sub>2</sub> and washed three times with water and twice with NaCl brine before being dried over MgSO<sub>4</sub>. The CH<sub>2</sub>Cl<sub>2</sub> was removed by rotary evaporation and the solid was redissolved in pre-dried CH<sub>2</sub>Cl<sub>2</sub>. This was added drop wise to 0°C petroleum ether. The yellow-orange precipitate was collected by vacuum filtration on a glass frit and washed with 0°C petroleum ether. The title compound was obtained in 73% yield and used without further purification. <sup>1</sup>H NMR (CDCl<sub>3</sub>): δ 8.57 (dd, 1H), 8.49 (d, 1H), 8.40 (d, 1H), 7.67 (dd, 1H), 7.17 (dd, 1H), 5.02 (m, 1H), 4.34 (t, 2H), 3.51 (m, 2H), 3.23 (t, 4H), 1.89 (m, 4H), 1.72 (m, 2H), 1.30 (s, 9H). Selected FT-IR (ATR): 3500-3000 cm<sup>-1</sup> (aliphatic primary amine N-H stretches), 3111 cm<sup>-1</sup> (naphthalene C-H), 3000-2750 cm<sup>-1</sup> (aliphatic C-H stretches), 1693 cm<sup>-1</sup> (imide C=O stretch), 1687 cm<sup>-1</sup> (primary amide C=O stretch), 1646 cm<sup>-1</sup> (imide C=O stretch).

***N*-(ethyl-2-ammonium)-4-(1-piperidinylnaphthalene-1,8-dicarboximide bromide (PNIHBr).** PNIenBoc (127 mg, 0.3 mmol) was dissolved in 30 mL THF to make a 0.01 M solution. To this, an HBr solution (10.2 mL) was added, resulting in an acid concentration of roughly 3 M. The reaction was allowed to proceed for 30 min at room temperature, after which time the characteristic PNIenBoc fluorescence was quenched as monitored by UV lamp (365 nm). The THF and some water were removed by rotary evaporation, and the resulting viscous orange liquid was added to 30 mL CH<sub>2</sub>Cl<sub>2</sub> and 15 mL water, yielding aqueous and organic layers. The aqueous layer was neutralized by addition of excess NaOH. The crude product was extracted into the CH<sub>2</sub>Cl<sub>2</sub>, which was then washed twice with water followed by two backwashes of the wash water with additional CH<sub>2</sub>Cl<sub>2</sub>. The recombined CH<sub>2</sub>Cl<sub>2</sub> solution was washed twice

with NaCl brine and dried over Na<sub>2</sub>SO<sub>4</sub> overnight. The CH<sub>2</sub>Cl<sub>2</sub> was removed by rotary evaporation. The resulting dark orange residue was dissolved in 25 mL ethanol. At this point, HBr (28 μL) was added and the reaction proceeded at room temperature for 1 h. After removing the ethanol by rotary evaporation, the pale orange solid was precipitated by adding diethyl ether and collected by vacuum filtration on a glass frit. It was rinsed several times with diethyl ether, affording the title compound in 91% yield, which was used without further purification. <sup>1</sup>H NMR (*d*<sub>6</sub>-DMSO): δ 8.47 (d, 1H), 8.42 (d, 1H), 8.38 (d, 1H), 7.81 (dd, 1H), 7.73 (m, 3H), 7.31 (d, 1H), 4.27 (t, 2H), 3.19 (t, 4H), 3.10 (m, 2H), 1.80 (m, 4H), 1.64 (m, 2H). Selected FT-IR (ATR): 3500-3000 cm<sup>-1</sup> (aliphatic primary amine N-H stretches), 3111 cm<sup>-1</sup> (naphthalene C-H), 3000-2750 cm<sup>-1</sup> (aliphatic C-H stretches), 1705 cm<sup>-1</sup> (imide C=O stretch), 1658 cm<sup>-1</sup> (imide C=O stretch).

**Nanoplatelet synthesis.** Nanoplatelets were synthesized using a nonsolvent crystallization method.<sup>5, 11</sup> All syntheses were performed under ambient conditions. Stock precursor solutions were prepared by dissolving the respective salts in DMF at concentrations of 0.1 M. The precursor solutions were then mixed in proper ratios to obtain the desired nanoplatelets. Most generally, nanoplatelets require a stoichiometric ratio of (2 moles of surfactant salt precursor) : (1 mole of PbBr<sub>2</sub>). For all syntheses, the final mixed precursor solution was rapidly injected into toluene undergoing vigorous stirring at room temperature. The nanoplatelets form immediately and can be taken for characterization without additional steps. After determining a 50/50 OA and BA mix to be the best surfactant composition for the control nanoplatelet species, as discussed later in the text, the relative proportions of PNI to OA and BA were systematically varied to target specific surface loadings of PNI surfactants on the nanoplatelet surface. In these

cases, I have used a 50/50 mixture of OABr and BABr as the (non-PNIHBr) surfactant precursor solution. In this work, 10  $\mu\text{L}$  of precursor DMF solution were added to either 1, 4 or 20 mL of toluene to obtain desired optical densities (OD) in the resulting toluene solutions.

**Post-synthetic modification.** Nanoplatelets could be isolated from the original synthetic solution by centrifugation. These nanoplatelets could not be precipitated by a polar solvent - in the manner typical of many nanomaterials - as the salt precursors are soluble in many polar solvents, leading to the destruction of the nanoplatelets. Most of the solution phase data presented herein used nanoplatelets as-synthesized in toluene. However, in certain cases the nanoplatelets were centrifuged and redispersed in an effort to confirm the presence of PNI surfactants near the surface of the nanoplatelets as opposed to merely coexisting in solution.

#### *4.3.3 Characterization and Spectroscopy*

**Molecular Characterization.**  $^1\text{H}$  NMR spectra were recorded on a Varian Inova (400 MHz) spectrometer. All chemical shifts were referenced to residual solvent signals previously referenced to TMS. Attenuated total reflectance (ATR) Fourier-transform infrared (FTIR) spectroscopy was conducted on solid powders using a Bruker Alpha Platinum ATR FTIR spectrometer.

**Nanomaterials Characterization.** Transmission electron microscopy (TEM) experiments were carried out using an FEI Talos F200X G2 scanning TEM (ThermoFisher Scientific). Images were acquired at an accelerating voltage of 200 kV. Samples were prepared by evaporation of dilute nanoplatelet suspensions in toluene that had been dropped onto an ultrathin carbon film on a lacey carbon support film on a 400

mesh Cu TEM grid. Powder X-ray diffraction (XRD) patterns were acquired using a Rigaku SmartLab X-ray diffractometer. Dynamic Light Scattering (DLS) was performed using a DynaPro Nanostar instrument from Wyatt Technology. All measurements were recorded at 25°C using 663 nm incident laser light. Scatter was collected at 90°. Each experiment contained an average of 50 acquisitions, and each acquisition had a 5 second duration. The hydrodynamic radii were calculated by using the Stokes-Einstein equation in Dynamics 7 software from Wyatt Technology.

**Spectroscopic Methods.** Absorption spectra were measured with a Shimadzu UV-3600 dual beam UV-Vis-NIR spectrophotometer. Steady-state photoluminescence spectra were obtained with an Edinburgh Instruments FLS 980 fluorimeter using a 450 W Xe arc lamp as the excitation source. Time-correlated single photon counting (TCSPC) experiments for PNIenBoc, PNIHBr, and the characteristic PNI fluorescence from the 100% PNI-ligated nanoplatelets, (PNI)<sub>2</sub>PbBr<sub>4</sub>, were performed on an Edinburgh Instruments Mini-Tau spectrometer, with a 405 nm diode laser (56.5 ps fwhm) as the excitation source. A band-pass filter centered at 500 nm with a 45 nm width was used to select the emission. TCSPC experiments for all nanoplatelet species were performed on a Lifespec-II picosecond lifetime spectrometer from Edinburgh Instruments equipped with a high-speed photodiode detector. The emission was collected at 420 nm (slit width 1 nm). The Lifespec-II measurements were excited at 400 nm (120 fs fwhm, 4 MHz repetition rate) by a Coherent Chameleon Ultra II tunable Ti:Sapphire laser passing through a second harmonic generator and pulse picker. All photoluminescence experiments used optically dilute solutions (OD 0.1-0.2) prepared in spectroscopic grade solvents. The recorded molecular fluorescence decays were fit using Edinburgh

Instruments T900 software, while the nanoplatelet photoluminescence decays were fit with Igor Pro 7 software from WaveMetrics. Please refer to subsection 4.8.1 for additional detail on the fitting of nanoplatelet photoluminescence decays.

## 4.4 Results and Discussion

### 4.4.1 Synthesis and Characterization of Colloidal Perovskite Nanoplatelets

The specific perovskite nanoplatelets from this study can be described using the formula  $L_2PbBr_4$ , where L is a stand-in for various alkyl ammonium surfactants. Refer to the Experimental Section for clarity on nanoplatelet-related abbreviations that will be used throughout. In the earliest stages of this study, the surfactant species L consisted of neat BA, HA, or OA as well as 50/50 mixtures of any two alkyl ammonium salts. The goal in exploring different optically inert surfactant combinations in the synthesis of the nanoplatelets was to determine which surfactants imparted the best colloidal stability to the system. The as-synthesized electronic absorption spectra for the six species of nanoplatelets made during this phase of the work are shown in Figure 4.1a. In the minutes immediately following synthesis, most of the nanoplatelets show similar optical properties. The most noteworthy difference is a slight bathochromic shift in the peak of the first exciton absorption band for the nanoplatelets where L consists entirely of BA. As BA is the shortest chain of the surfactants tested here, this shift could be due to some kind of aggregation in solution. Upon aging the nanoplatelet solutions for 24 h (Figure 4.1b), the optical properties change drastically. All species show some loss in absorbance relative to the as-synthesized solutions. In comparing the neatly-capped nanoplatelet species, OA and HA (Figure 4.1, red and green traces) were roughly equivalent while BA (blue) saw the most extensive degradation – as inferred from the Beer-Lambert Law – of

any species, neat or mixed surfactants. This trend suggests longer alkyl chains provide greater colloidal stability. The mixed-surfactant species (black, gray, purple) were uniformly more stable than the neat-surfactant species, implying that surfactant length heterogeneity imparts greater stability as well. One final point on the alkyl ammonium surfactants is that the OA/BA (black) species being most stable seems to suggest the importance of attaining a greater degree of chain length heterogeneity when stabilizing these nanoplatelets in solution.

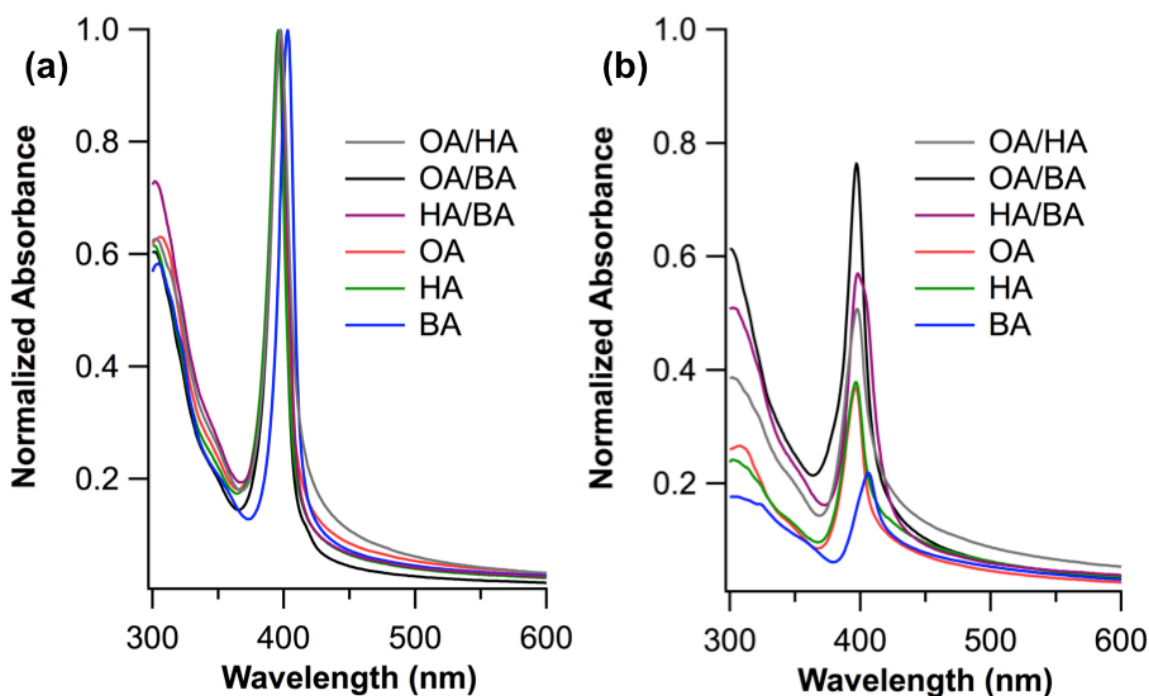


**Figure 4.1** Ground state electronic absorption spectra for  $L_2PbBr_4$  perovskite nanoplatelets synthesized with six different types of surfactant (a) immediately after synthesis and (b) after 24 h in solution.

The steady state photoluminescence spectrum for the (OA)(BA) $PbBr_4$  nanoplatelets is presented in Figure 4.2. The emission profile displays a narrow peak with a small Stokes shift (ca.  $300\text{ cm}^{-1}$ ) from the first exciton absorbance maximum to the emission maximum. There is also a broad tail of weak emission at longer wavelengths, in agreement with the literature.<sup>5</sup> Transmission electron microscopy (TEM) images of the

as-synthesized nanoplatelets (Figure S4.1) show roughly square nanomaterials that are 100's of nanometers long in the two unconfined dimensions (Figure S4.1a). Fast-Fourier transform of the TEM images (Figure S4.1b, inset) calculates an interatomic distance of 0.28 nm, in close agreement to the reported Br-Pb-Br linear distance of  $\sim 0.6$  nm.<sup>11, 12</sup> The powder X-ray diffraction (XRD) of the nanoplatelets drop-casted on a Si wafer shows a number of peaks (Figure S4.2), potentially indicative of unexpectedly low symmetry. However, detailed analysis shows the peaks are a result of three discrete inter-nanoplatelet distances and peaks at increasingly higher angles as a result of their periodicity in accordance with Bragg's law. The three inter-nanoplatelet d-spacings calculated from Bragg's law come out to 1.37 nm, 1.76 nm, and 2.09 nm. Accounting for the 0.56 nm thickness of the nanoplatelets, these d-spacings imply that the alkyl ammonium cations are occupying spaces of 0.81 nm, 1.20 nm, or 1.53 nm along the dimension between nanoplatelets. Considering the lengths of BA ( $\sim 0.5$  nm) and OA (1.0 nm), these values are consistent with the coexistence of  $(\text{BA})_2\text{PbBr}_4$ ,  $(\text{OA})(\text{BA})\text{PbBr}_4$ , and  $(\text{OA})_2\text{PbBr}_4$  nanoplatelet species, with similar amounts of alkyl chain interdigitation among all three. These findings are in strong agreement with the literature.<sup>5</sup>

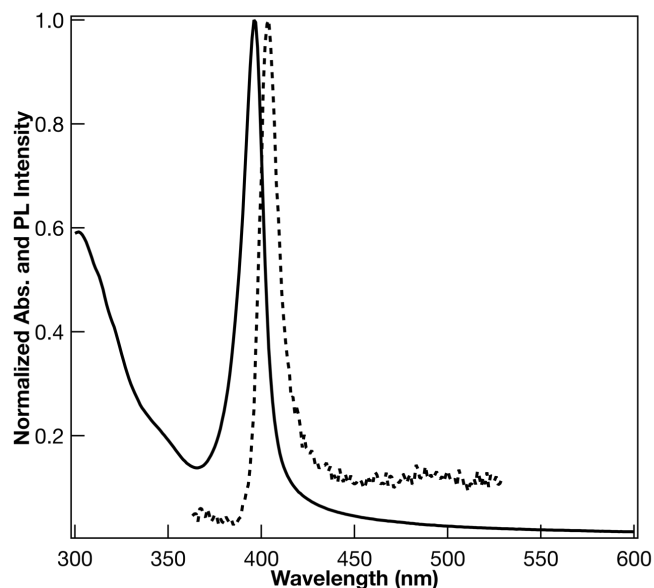
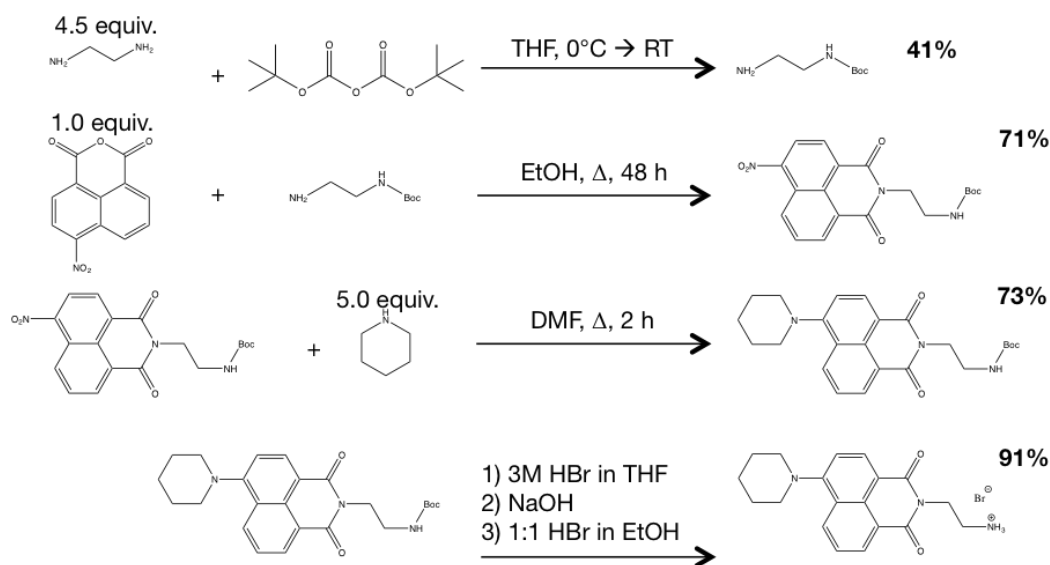


**Figure 4.2** The absorbance (solid) and steady state emission (dashed) spectra of (OA)(BA)PbBr<sub>4</sub> nanoplatelets in toluene. Emission spectrum was recorded at 298 K using 320 nm excitation.

#### 4.4.2 Synthesis of PNI Surfactants

One goal of the study was to devise a method for decorating the nanoplatelet surface with molecular chromophores. For this purpose, an alkyl ammonium derivative of 4-piperidinylnaphthaleneimide (PNI) was chosen as the chromophore. PNI was selected



**Scheme 4.1** Synthetic scheme for PNIHBr.

for a combination of factors including the solubility of the molecule in toluene, the spectral overlap of PNI absorption and undecorated nanoplatelet photoluminescence, and the synthetic plausibility of a PNI-alkyl-ammonium derivative. The PNI surfactant was made by combining a number of established synthetic protocols (Scheme 4.1).<sup>9, 10</sup> It is possible to Boc-protect only one of the two primary amines on ethylenediamine by reacting di-*tert*-butyl dicarbonate with a large stoichiometric excess of ethylenediamine at low temperatures. Reaction of 4-nitronaphthalene-1,8-dicarboxyanhydride with the mono-protected ethylenediamine in refluxing ethanol gives the corresponding imide while preserving the nitro group on the naphthalene. Replacement of the naphthalene nitro group by reacting with excess piperidine in refluxing DMF yields PNIenBoc. De-protection of the primary amine by treatment with dilute hydrobromic acid gives the alkyl amine derivative of PNI, which is isolated as the ammonium bromide salt, PNIHBr. The absorption and emission spectra of the parent PNIenBoc molecule (Figure 4.3) are reminiscent of related PNI compounds, with spectral characteristics common to many charge transfer excited states,<sup>10, 13, 14</sup> namely: broad, featureless emission and a relatively large Stokes shift. Comparison of the spectral features in Figure 4.3 gives an idea of the degree of spectral overlap between the nanoplatelet emission and the PNI chromophore absorption. The fluorescence lifetime decay constants for PNIenBoc and PNIHBr in toluene were determined to be 8.2 ns and 7.2 ns, respectively (Figure S4.3).

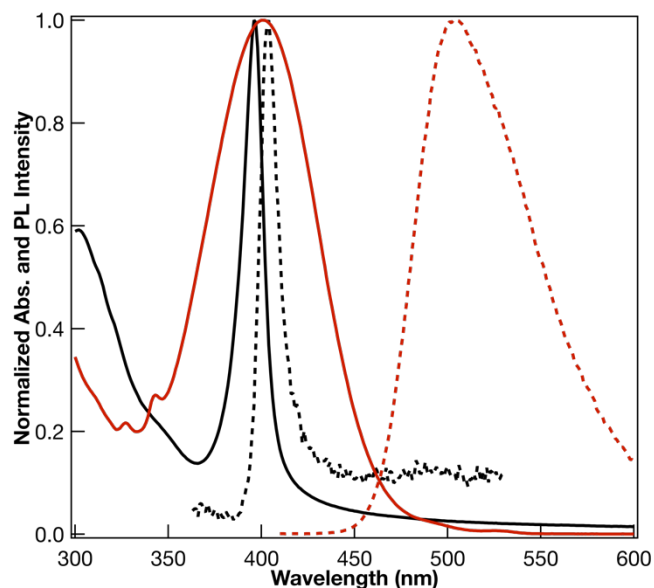


**Figure 4.3** The absorbance (solid) and fluorescence (dashed) spectra of (red) PNIEtBoc in toluene overlaid on the (OA)(BA)PbBr<sub>4</sub> nanoplatelet spectra from Figure 4.2 (black). PNIEtBoc emission spectrum was recorded at 298 K using 405 nm excitation.

#### 4.4.3 Self-Assembly of Colloidal Perovskite Nanoplatelets with PNI Surfactants

With the PNIHBr surfactant isolated, the synthesis of lead bromide perovskite nanoplatelets with PNI surfactants near the surface in place of various percentages of the mixed OA and BA colloidal stabilizing surfactants was undertaken. Initial results suggested the nanoplatelets remained soluble in toluene even when the OA and BA had been entirely replaced by PNI. There is literature precedent for solubilizing lead bromide perovskite nanomaterials with bulky ligands in which CH<sub>3</sub>NH<sub>3</sub>PbBr<sub>3</sub> nanocrystals were solubilized by branched, Si-containing ligands.<sup>15</sup> To understand this phenomenon, 100% PNI-stabilized nanoplatelets, (PNI)<sub>2</sub>PbBr<sub>4</sub>, were imaged by TEM (Figure S4.4). The TEM images show little change from the (OA)(BA)PbBr<sub>4</sub> nanoplatelets (Figure S4.1), with rounded square nanoplatelets 100's of nanometers long in two dimensions. On the contrary, the XRD patterns obtained for (PNI)<sub>2</sub>PbBr<sub>4</sub> were amorphous regardless of evaporation conditions (Figure S4.5). This suggests the PNI surfactants prevent the

nanoplatelets from stacking when evaporating on a Si substrate, and the mechanistic reasons for the lack of periodic order upon evaporation are unclear at this time. While the TEM images are indicative that the soluble species in toluene solution remain nanoplatelets, there is another possibility. If the soluble species are not nanoplatelets, but are exhibiting micellar behavior in solution, they might potentially form structures superficially similar to nanoplatelets upon evaporation of the toluene. A plausible species that would not be a nanoplatelet is the tetrabromoplumbate(II) anion associated with two PNI-ethyl ammonium surfactants. Furthermore, if the remnant structures upon toluene evaporation are liquid crystalline, as expected for cation-templated tetrabromoplumbate(II), that would rationalize the absence of Bragg diffraction peaks in the powder XRD data.

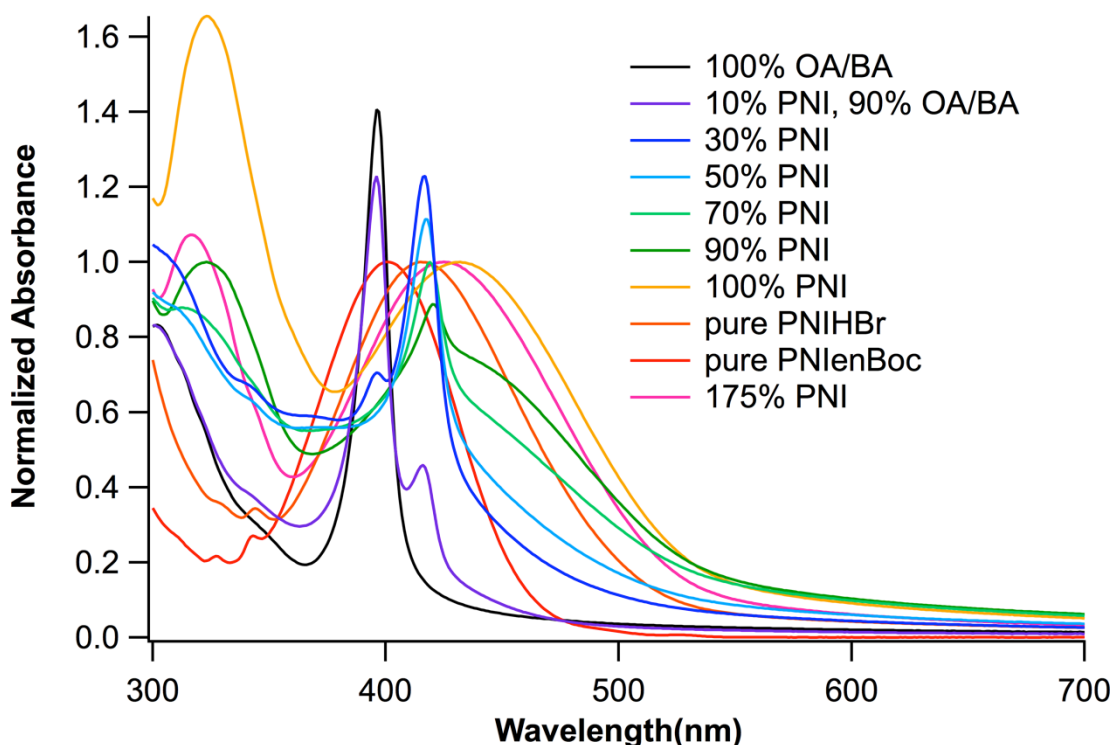


**Figure 4.4** Electronic absorption spectra of  $L_2PbBr_4$  nanoplatelets with (multi-color, see legend) and without (black) various PNI surfactant loadings, PNIenBoc (red), and free PNIHBr (orange) in toluene. The 175% PNI loading corresponds to an excess of the PNI surfactant precursor in the nanoplatelet synthesis (see text).

The PNI-ligated nanoplatelets were soluble in toluene at loadings up to and including complete replacement of the OA/BA mix by exclusively PNI (Figure 4.4). At the initial introduction of 10% PNIHBr to the nanoplatelet precursor solution (i.e. 10% of the surfactant salt in the DMF precursor solution is PNIHBr with 45% OABr and 45% BABr as the other surfactant salts – see the Experimental Section for further detail), a new peak appears in the absorption spectrum at 416 nm (Figure 4.4, purple trace). The new feature corresponds to no features in the absorption spectra of undecorated nanoplatelets (black), free PNI molecules (red), or the PNI surfactant precursor salt (orange). This new feature grows as the precursor PNI loading, and therefore – theoretically – the surface PNI loading, is increased up to 30% (dark blue), but it persists at all loadings up to 90% (dark green). In the nanoplatelets where no OA or BA are present in the system (yellow), there are two prominent peaks in the absorption spectra at 322 nm and 432 nm. The 432 nm feature resembles the absorption peak associated with the lowest energy singlet transition in most PNI species, but displays a significant bathochromic shift from either the free PNI molecule or the PNIHBr salt in toluene. The feature at 322 nm does not correspond to any feature in the PNI spectra and seems to require the presence of nanoplatelets. The feature at 322 nm may also correspond to the absorption characteristic of the tetrabromoplumbate(II) anionic unit, which has been templated by the PNI surfactants. It follows that this electronic absorption feature would only appear at PNI loadings of 90-100%. When a 75% excess of PNIHBr was used in the synthesis of the nanoplatelets (pink), the resulting absorption spectrum closely resembles a linear combination of the 100% PNI nanoplatelets and PNIHBr in toluene (Figure S4.6).

As a coarse measure of whether the increased precursor PNI concentration was simply leading to increased free PNI in the final toluene solution, the nanoplatelets were collected by centrifugation and re-dispersed in toluene. After confirming the absorption spectra of the nanoplatelets had not changed post-centrifugation, the supernatants were examined *via* their absorption spectra (Figure S4.7). The relative lack of change in concentration of PNI in the supernatant from 30% to 90% suggests that the increased PNI in the precursor solution was likely consumed by the nanoplatelet self-assembly process in some manner, preferably associating with the surface in place of the now-removed OA/BA mix. Furthermore, the concentration of PNI in the supernatant of the 100% PNI nanoplatelets was reduced from that of 30-90%, suggesting that the 100% PNI synthesis condition is even more conducive to appending PNI to the nanoplatelet surface. Additionally, the nanoplatelets synthesized with excess PNIHBr had a greater concentration of PNI in the supernatant than any other nanoplatelet species and centrifugation of a toluene solution of PNIHBr gave an even greater concentration still of PNI in the supernatant. These results are consistent with the PNI surfactant being stoichiometrically consumed by the nanoplatelet self-assembly. Dynamic light scattering (DLS) experiments clearly indicate 100% PNI nanoplatelets have a larger hydrodynamic radius than OA/BA mix nanoplatelets (Figure S4.8). This data also suggests the larger PNI surfactants are at the surface of the 100% PNI nanoplatelets in place of the OA and BA surfactants on the surface of the unadorned nanoplatelets. This DLS data could also be rationalized by the formation of micelles as proposed above.

#### 4.4.4 Photoluminescence Quenching by PNI Surfactants

The nanoplatelets display steady state emission spectra with characteristics of PNI fluorescence, centered around 500 nm, and nanoplatelet photoluminescence, centered around either 403 nm or 420 nm, until the PNI loadings surpass 50% (Figure 4.5). At PNI surfactant loadings of greater than 50%, the emission spectrum is dominated by characteristic PNI fluorescence. With the favorable spectral overlap and evidence of close proximity from structural characterization, it follows that the quenching of the nanoplatelet photoluminescence could be due to dipolar Förster resonance energy transfer (FRET).<sup>7</sup> In order to more quantitatively assign FRET as the quenching mechanism for the perovskite nanoplatelet excited state, the characteristic nanoplatelet photoluminescence decay was monitored by time-correlated single photon counting (TCSPC) at 420 nm (Figure 4.6).

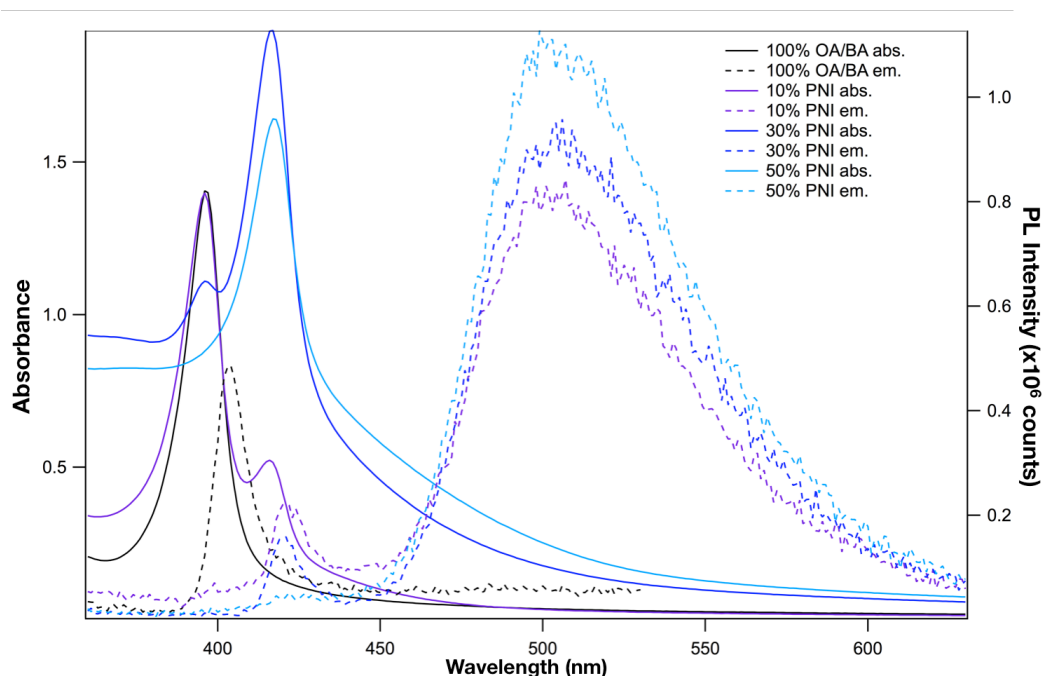


**Figure 4.5** Electronic absorption (solid) and emission (dashed) spectra of (OA)(BA)PbBr<sub>4</sub> nanoplatelets (black) as well as nanoplatelet species with 10% (purple), 30% (dark blue), and 50% (light blue) of their OA and BA surfactants replaced by PNI surfactants. Emission spectra were recorded at 298 K using 320 nm excitation.

Analysis of the TCSPC data is complicated somewhat by the intrusion of a PNI fluorescence lifetime component in systems with high PNI loadings. The reasons for the intrusion are twofold. First, the extra PNI loading provides more PNI molecules that can be excited by FRET and directly by the excitation laser. Second, the high-loading systems have more highly quenched nanoplatelet photoluminescence, leading to longer collection times in order to reach sufficient stop counts (refer to subsection 1.3.3 for more on stop counts). For greater detail on the fitting procedures used to assign decay lifetimes, please refer to subsection 4.8.1. In brief, all nanoplatelet photoluminescence decays except for the 100% PNI-ligated nanoplatelets,  $(\text{PNI})_2\text{PbBr}_4$ , were fit with stretched exponential decay curves after de-convolution of the instrument response function (IRF). The IRF-deconvoluted data for  $(\text{PNI})_2\text{PbBr}_4$  can be fit by a monoexponential decay curve

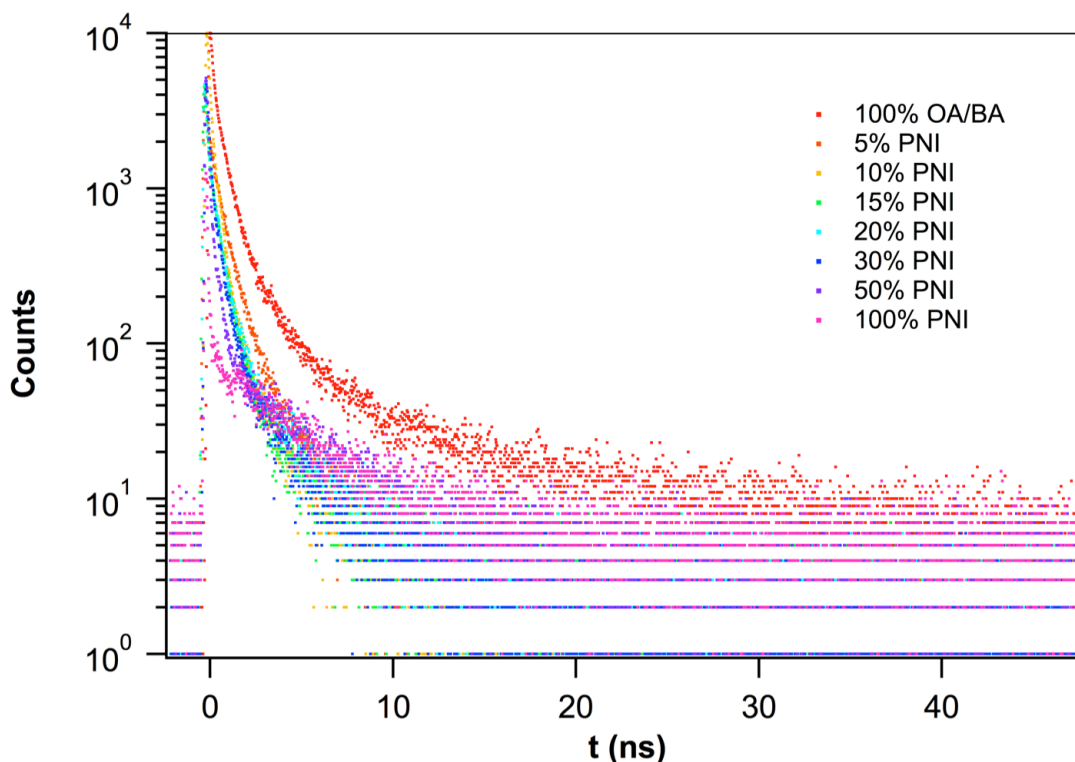


**Figure 4.6** TCSPC PL intensity decays of  $(\text{OA})(\text{BA})\text{PbBr}_4$  nanoplatelets without (red) and with various PNI surfactant loadings (many colors, see legend) illustrating dynamic quenching likely from FRET. Decays were recorded at 420 nm with a 1 nm slit width and were excited at 400 nm with a 4 MHz repetition rate.

with a decay constant of 4.5 ns. The raw (PNI)<sub>2</sub>PbBr<sub>4</sub> data can also be fit with a biexponential decay curve, yielding decay constants of 4.2 ns and 91 ps. The 4.2-4.5 ns decay constant matches the order of magnitude (6.7 ns) of the decay constant for the fluorescence from PNI surfactants appended to nanoplatelets, as determined in a separate measurement (Figure S4.9). Taken in concert, this data implies that the 91 ps component is the IRF while the ns component is likely high-energy fluorescence from the PNI surfactants. Lastly, the amplitude of the ns component was great enough in the 50% PNI-ligated system that a modeled PNI fluorescence component could be de-convoluted from the TCSPC data after the de-convolution of the IRF.

**Table 4.1** TCSPC Fitting Parameters and Energy Transfer Rate Constants.

%PNI	$\tau$ (ps)	$\beta^a$	$\langle\tau\rangle$ (ps) <sup>b</sup>	$k_{\text{FRET}}$ ( $10^9 \text{ s}^{-1}$ ) <sup>c</sup>
0	741	0.81	832	--
5	637	0.91	666	0.30
10	437	0.90	460	0.97
15	442	0.93	457	0.99
20	433	0.91	453	1.01
30	320	0.92	333	1.80
50	163	0.91	171	4.65
100	n.d.	n.d.	< 91	> 9.79

*a* Stretched exponential fitting parameter, see subsection 4.8.1 for more detail. *b* Average lifetime.<sup>16</sup> *c* Calculated from the expression:  $k_{\text{FRET}} = 1/\langle\tau\rangle - 1/\langle\tau\rangle_0$ .<sup>17</sup>

The results of the decay fitting are given in Table 4.1. The average photoluminescence lifetime of the nanoplatelets decreases as the percentage of PNI surfactants appended to the surface increases. Across all eight data points, the rate constant of lifetime quenching (as measured by  $k_{\text{FRET}}$ ) is an approximately linear function of the percentage of PNI surfactants in the system. The two most significant outliers are

the nanoplatelets with 20% and 30% PNI loadings. This could be due to an inhomogeneous distribution of PNI surfactants on the nanoplatelet surfaces, leading to a smaller than expected change in the mean exciton diffusion length required to encounter an acceptor surfactant before radiative recombination. However, a more likely possibility can be understood qualitatively by revisiting Figure 4.5. The 20% PNI system is where the relatively long-lived PNI component begins to appear in the data to a significant degree. One can visualize this by noting the inversion of the 15% PNI decay (green markers) and 20% PNI decay (light blue). At high photon counts, 15% PNI decay markers are in later time bins (i.e. to the right of 20% PNI), as expected. However, at low photon counts, 15% PNI decay markers are now in earlier time bins (to the left). The relatively longer-lived PNI fluorescence decay will artificially lengthen the time assigned by the stretched exponential fitting. The final experiment to confidently assign FRET would be to selectively excite the nanoplatelets and monitor the characteristic fluorescence of the PNI surfactants. Unfortunately, as Figure 4.3 shows, the absorption spectrum of the PNI surfactant completely overlaps that of the nanoplatelets, making nanoplatelet-selective excitation impossible. Furthermore, the PNI surfactants are so emissive that the influence of nanoplatelet absorption on an excitation spectrum of PNI surfactant fluorescence is undetectable. While an unassigned energy transfer process was reported between different sizes of CsPbBr<sub>3</sub> perovskite nanocrystals,<sup>18</sup> to the best of our knowledge, these findings represent the first observation of FRET from colloidal perovskite nanomaterials to molecules. There is precedent for FRET from nanomaterials to molecules from a study involving CdSe nanocrystals and a squaraine-based dye.<sup>19</sup>

## 4.5 Conclusions

We have identified a general scheme for associating molecular chromophores to the surface of  $L_2PbX_4$  nanoplatelets to broaden the study of the interaction between quantum-confined semiconducting nanomaterials and molecular chromophores. We synthesized a molecular chromophore targeted specifically for this purpose and were able to synthesize the nanoplatelets with a surprisingly wide range of chromophore loading percentages. Study of the photoluminescence of these nanoplatelets and the characteristic fluorescence of the PNI surfactants is highly suggestive of FRET from the perovskite nanoplatelets to the PNI surfactant molecules. If FRET were indeed operative, the findings demonstrated herein would represent the first observation of FRET from any colloidal perovskite nanomaterial to a molecule. At minimum, this novel nanoplatelet-PNI hybrid system should provide an effective test bed for the chemistry necessary to associate molecular chromophores with low-temperature, self-assembled colloidal perovskite nanomaterials.

## 4.6 Acknowledgments

We acknowledge support for this work from the Organic Materials Chemistry program in the Air Force Office of Scientific Research (FA9550-18-1-0331). Transmission electron microscopy and powder X-ray diffraction were performed at the Analytical Instrumentation Facility (AIF) at North Carolina State University, which is supported by the State of North Carolina and the National Science Foundation (Award Number ECCS-1542015). The AIF is a member of the North Carolina Research Triangle Nanotechnology Network (RTNN), a site in the National Nanotechnology Coordinated Infrastructure (NNCI).

## 4.7 References

1. Nedelcu, G.; Protesescu, L.; Yakunin, S.; Bodnarchuk, M. I.; Grotevent, M. J.; Kovalenko, M. V., Fast Anion-Exchange in Highly Luminescent Nanocrystals of Cesium Lead Halide Perovskites ( $\text{CsPbX}_3$ , X = Cl, Br, I). *Nano Letters* **2015**, *15* (8), 5635-5640.
2. Protesescu, L.; Yakunin, S.; Bodnarchuk, M. I.; Krieg, F.; Caputo, R.; Hendon, C. H.; Yang, R. X.; Walsh, A.; Kovalenko, M. V., Nanocrystals of Cesium Lead Halide Perovskites ( $\text{CsPbX}_3$ , X = Cl, Br, and I): Novel Optoelectronic Materials Showing Bright Emission with Wide Color Gamut. *Nano Letters* **2015**, *15* (6), 3692-3696.
3. Akkerman, Q. A.; D'Innocenzo, V.; Accornero, S.; Scarpellini, A.; Petrozza, A.; Prato, M.; Manna, L., Tuning the Optical Properties of Cesium Lead Halide Perovskite Nanocrystals by Anion Exchange Reactions. *Journal of the American Chemical Society* **2015**, *137* (32), 10276-10281.
4. Luo, X.; Lai, R. C.; Li, Y. L.; Han, Y. Y.; Liang, G. J.; Liu, X.; Ding, T.; Wang, J. H.; Wu, K. F., Triplet Energy Transfer from  $\text{CsPbBr}_3$  Nanocrystals Enabled by Quantum Confinement. *Journal of the American Chemical Society* **2019**, *141* (10), 4186-4190.
5. Weidman, M. C.; Seitz, M.; Stranks, S. D.; Tisdale, W. A., Highly Tunable Colloidal Perovskite Nanoplatelets through Variable Cation, Metal, and Halide Composition. *ACS Nano* **2016**, *10* (8), 7830-7839.
6. Weidman, M. C.; Goodman, A. J.; Tisdale, W. A., Colloidal Halide Perovskite Nanoplatelets: An Exciting New Class of Semiconductor Nanomaterials. *Chemistry of Materials* **2017**, *29* (12), 5019-5030.
7. Lakowicz, J. R., *Principles of Fluorescence Spectroscopy*. 3rd ed.; Springer: New York, 2006.
8. Dexter, D. L., A Theory of Sensitized Luminescence in Solids. *Journal of Chemical Physics* **1953**, *21* (5), 836-850.
9. Xu, P.; Zhang, T.; Wang, W.; Zou, X.; Zhang, X.; Fu, Y., Synthesis of PNA Monomers and Dimers by Ugi Four-Component Reaction. *Synthesis* **2003**, *2003* (08), 1171-1176.
10. Tyson, D. S.; Luman, C. R.; Zhou, X.; Castellano, F. N., New Ru(II) Chromophores with Extended Excited-State Lifetimes. *Inorganic Chemistry* **2001**, *40* (16), 4063-4071.
11. Pathak, S.; Sakai, N.; Wisnivesky Rocca Rivarola, F.; Stranks, S. D.; Liu, J.; Eperon, G. E.; Ducati, C.; Wojciechowski, K.; Griffiths, J. T.; Haghighirad, A. A.; Pellaroque, A.; Friend, R. H.; Snaith, H. J., Perovskite Crystals for Tunable White Light Emission. *Chemistry of Materials* **2015**, *27* (23), 8066-8075.
12. Tyagi, P.; Arveson, S. M.; Tisdale, W. A., Colloidal Organohalide Perovskite Nanoplatelets Exhibiting Quantum Confinement. *The Journal of Physical Chemistry Letters* **2015**, *6* (10), 1911-1916.
13. Greenfield, S. R.; Svec, W. A.; Gosztola, D.; Wasielewski, M. R., Multistep Photochemical Charge Separation in Rod-like Molecules Based on Aromatic Imides and Diimides. *Journal of the American Chemical Society* **1996**, *118* (28), 6767-6777.

14. de Silva, A. P.; Gunaratne, H. Q. N.; Habib-Jiwan, J.-L.; McCoy, C. P.; Rice, T. E.; Soumillion, J.-P., New Fluorescent Model Compounds for the Study of Photoinduced Electron Transfer: The Influence of a Molecular Electric Field in the Excited State. *Angewandte Chemie International Edition in English* **1995**, *34* (16), 1728-1731.
15. Luo, B.; Pu, Y.-C.; Lindley, S. A.; Yang, Y.; Lu, L.; Li, Y.; Li, X.; Zhang, J. Z., Organolead Halide Perovskite Nanocrystals: Branched Capping Ligands Control Crystal Size and Stability. *Angewandte Chemie International Edition* **2016**, *55* (31), 8864-8868.
16. Anderson, A. Y.; Barnes, P. R. F.; Durrant, J. R.; O'Regan, B. C., Quantifying Regeneration in Dye-Sensitized Solar Cells. *The Journal of Physical Chemistry C* **2011**, *115* (5), 2439-2447.
17. Bakalova, R.; Ohba, H.; Zhelev, Z.; Ishikawa, M.; Baba, Y., Quantum dots as photosensitizers? **2004**, *22* (11), 1360-1361.
18. de Weerd, C.; Gomez, L.; Zhang, H.; Buma, W. J.; Nedelcu, G.; Kovalenko, M. V.; Gregorkiewicz, T., Energy Transfer between Inorganic Perovskite Nanocrystals. *The Journal of Physical Chemistry C* **2016**, *120* (24), 13310-13315.
19. Hoffman, J. B.; Choi, H.; Kamat, P. V., Size-Dependent Energy Transfer Pathways in CdSe Quantum Dot–Squaraine Light-Harvesting Assemblies: Förster versus Dexter. *The Journal of Physical Chemistry C* **2014**, *118* (32), 18453-18461.
20. Förster, T., Zwischenmolekulare Energiewanderung und Fluoreszenz. *Annalen der Physik* **1948**, *437* (1-2), 55-75.
21. van Driel, A. F.; Nikolaev, I. S.; Vergeer, P.; Lodahl, P.; Vanmaekelbergh, D.; Vos, W. L., Statistical analysis of time-resolved emission from ensembles of semiconductor quantum dots: Interpretation of exponential decay models. *Physical Review B* **2007**, *75* (3), 035329.
22. Dutta, P.; Beaulac, R., Photoluminescence Quenching of Colloidal CdSe and CdTe Quantum Dots by Nitroxide Free Radicals. *Chemistry of Materials* **2016**, *28* (4), 1076-1084.

## 4.8 Supporting Information

### 4.8.1 Details on Fitting Nanoplatelet Photoluminescence Decays

Perovskite nanoplatelets emit from a distribution of excited states.<sup>17</sup> As such, all nanoplatelet photoluminescence decays, except for the 100% PNI-ligated nanoplatelets, (PNI)<sub>2</sub>PbBr<sub>4</sub>, were fit with stretched exponential decay curves. Stretched exponential equations have been used to model the fluorescence decay of disordered systems for over 70 years.<sup>20</sup> The kinetic data obtained from nanoplatelet TCSPC experiments were fit using the following equation:<sup>17, 20</sup>

$$I(t) = I_0 e^{-(t/\tau)^\beta} \quad (\text{Eq. 8})$$

Where  $I$  and  $\tau$  are the photoluminescence intensity and the stretched exponential decay constant, respectively, corresponding to the radiative lifetime of the nanoplatelet photoluminescence, and  $\beta$  is the stretching exponent. While the fitting parameters  $\tau$  and  $\beta$  are not considered physically meaningful for quantifying the emission lifetime from quantum-confined semiconductor nanomaterials,<sup>21</sup> they make it mathematically tractable to compute average lifetime values,  $\langle\tau\rangle$ . These values can be taken as meaningful quantifiers for ensemble average lifetimes as long as no assumptions are made regarding the physical nature of the underlying distribution of decay rate constants.<sup>22</sup> The average lifetimes were calculated from the following equation using  $\tau$  and  $\beta$  values obtained from fitting.<sup>16, 22</sup>

$$\langle\tau\rangle = \frac{\tau}{\beta} \cdot \Gamma\left(\frac{1}{\beta}\right) \quad (\text{Eq. 9})$$

Where  $\Gamma(n)$  is the mathematical gamma function. The nanoplatelets range from 100s of nm to 1  $\mu\text{m}$  in the two unconfined dimensions.<sup>5</sup> As a result of this size, colloidal solutions of the nanoplatelets are highly scattering in the visible region of the

electromagnetic spectrum. Additionally, much of the steady state nanoplatelet photoluminescence is quenched as soon as any PNI ligands are introduced to the surface (*vide supra*). Due to this combination of factors, the instrument response function (IRF) makes up a significant portion of the TCSPC data. Failure to de-convolute the IRF from the decay data before modeling the kinetics with a stretched exponential will result in the calculation of shorter average lifetime constants than are actually supported by the data, although trends between samples will be approximately conserved. As such, the IRF was measured on the Lifespec-II picosecond lifetime spectrometer and de-convoluted from the TCSPC data in F900 software from Edinburgh Instruments before the data was exported for further analysis in Igor Pro 7 software from WaveMetrics. The IRF-de-convoluted data for  $(\text{PNI})_2\text{PbBr}_4$  can be fit by a monoexponential decay curve with a decay constant of 4.5 ns. The raw  $(\text{PNI})_2\text{PbBr}_4$  data can also be modeled by a biexponential decay curve, yielding decay constants of 4.2 ns and 91 ps. The 4.2-4.5 ns decay constant matches the order of magnitude (6.7 ns) of the decay constant for the fluorescence from PNI ligands appended to nanoplatelets, as determined in a separate measurement (Figure S4.9). Taken in concert, this data implies that the 91 ps component is the IRF, while the ns component is likely “hot” (vibrationally excited) fluorescence from the PNI ligands that passed through the monochromator. As a final note, the amplitude of the ns component was great enough in the 50% PNI-ligated system that a PNI fluorescence component could be modeled as a monoexponential decay function, which was de-convoluted from the decay data after the de-convolution of the IRF and before the fitting with a stretched exponential curve.

#### 4.8.2 Supplemental Figures

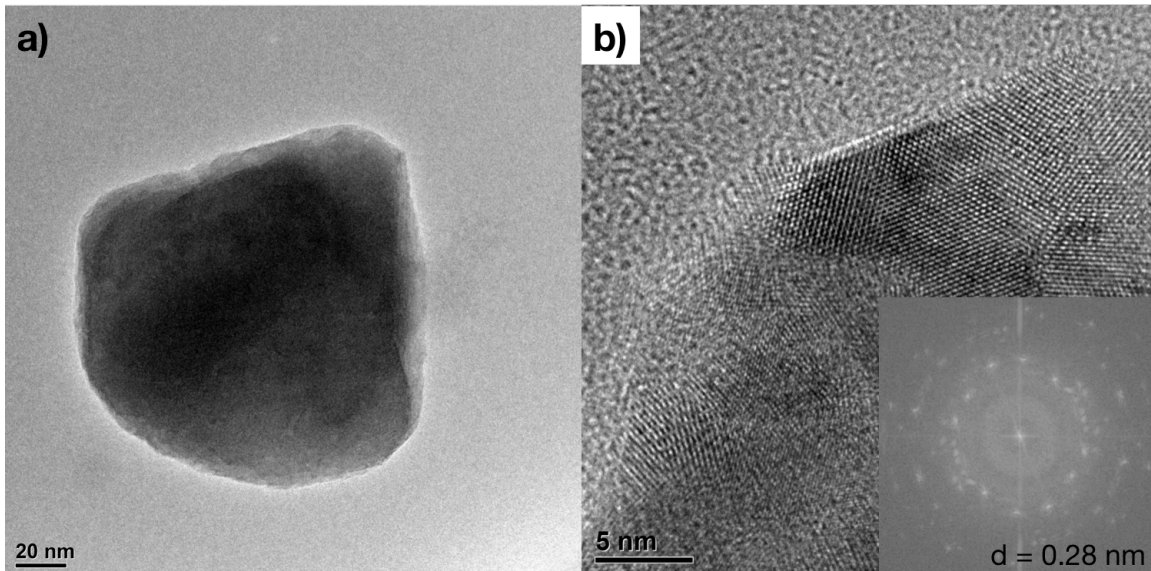


**Figure S4.1** TEM images of (OA)(BA)PbBr<sub>4</sub> nanoplatelets and (b, inset) FFT of the lattice planes imaged in (b).

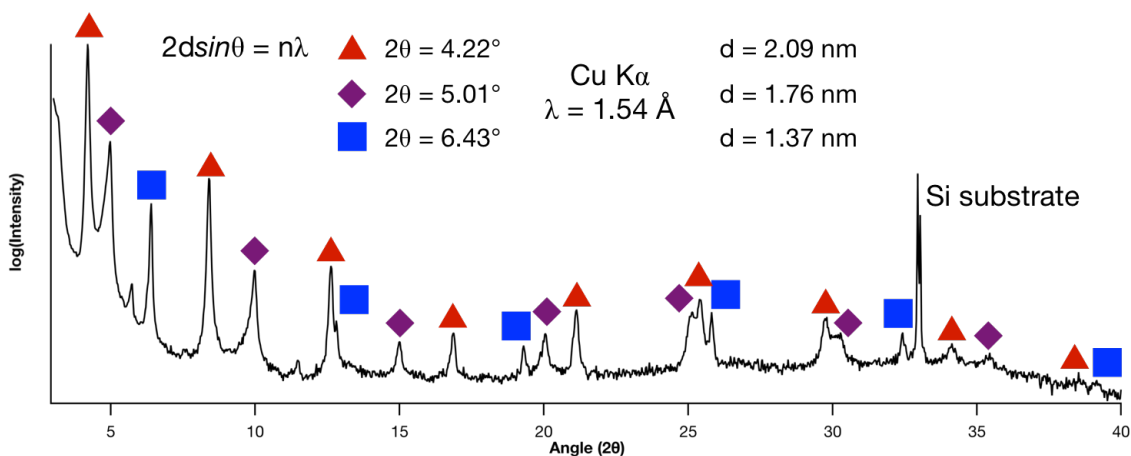


**Figure S4.2** XRD pattern for (OA)(BA)PbBr<sub>4</sub> nanoplatelets where the precise surfactant composition, OA, BA, or a mixture of both, results in changes to the nanoplatelet superlattice stacking distance.

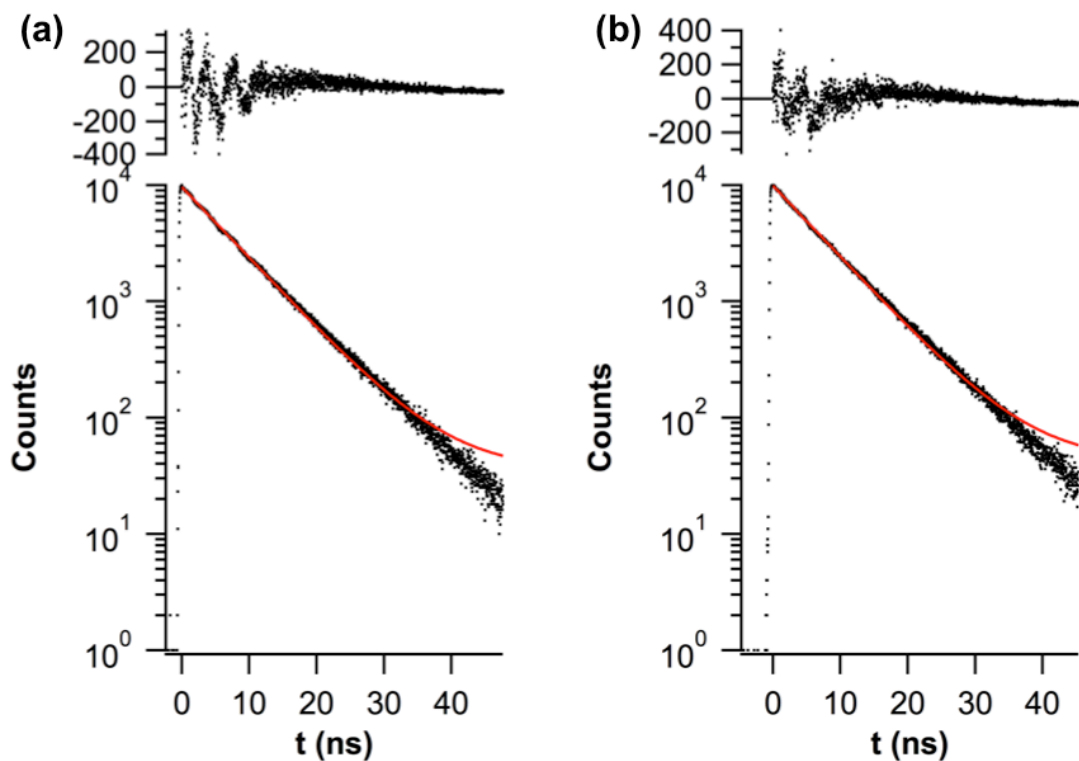


**Figure S4.3** TCSPC fluorescence intensity decays of (a) PNInBoc and (b) PNIHBr in toluene. The red traces are monoexponential decay curves fit to the TCSPC data with the residuals displayed above. Samples were excited by a 405 nm diode laser (56.5 ps fwhm) set to a 100 kHz repetition rate. A band-pass filter centered at 500 nm with a 45 nm width was used to select the emission.

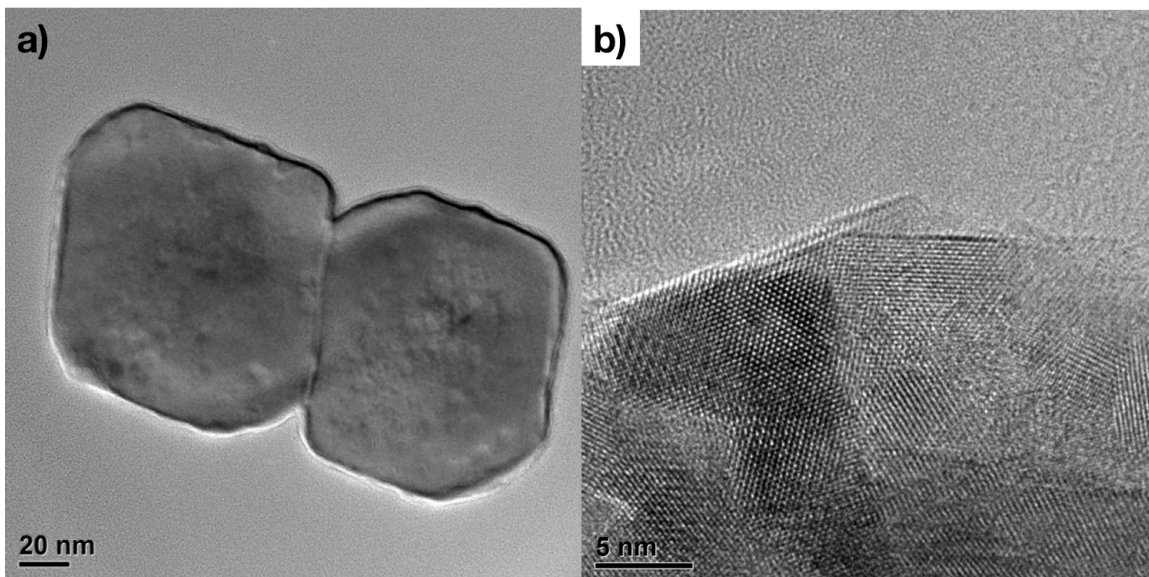


**Figure S4.4** TEM images of (PNI)PbBr<sub>4</sub> nanoplatelets.

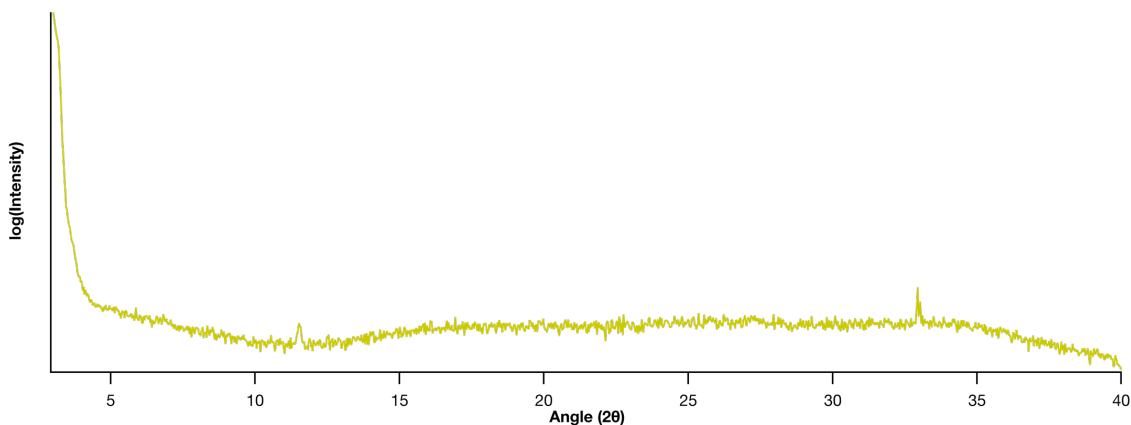


**Figure S4.5** XRD pattern for (PNI)PbBr<sub>4</sub> nanoplatelets where only the reflections due to the Si substrate at  $2\theta = 32.95^\circ$  and  $33.03^\circ$  and an unassigned reflection at  $11.50^\circ$  are visible. The reflection at  $2\theta = 11.50^\circ$  also appears for (OA)(BA)PbBr<sub>4</sub> nanoplatelets (Figure S4.2).

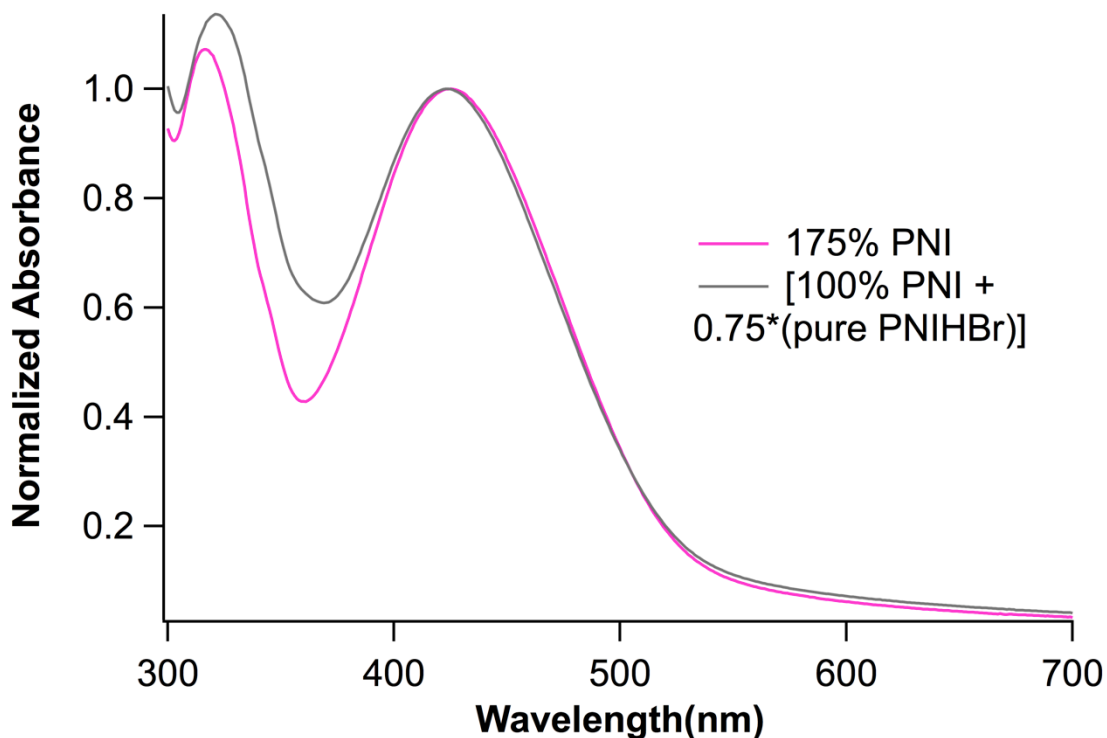


**Figure S4.6** The electronic absorption spectrum (pink) of lead bromide perovskite nanoplatelets synthesized with a 75% excess of the PNIHBr ligand salt precursor compared to a linear combination (gray) of the absorption spectrum of 100% PNI-ligated nanoplatelets and 0.75 times the absorption spectrum of the PNIHBr salt in toluene.

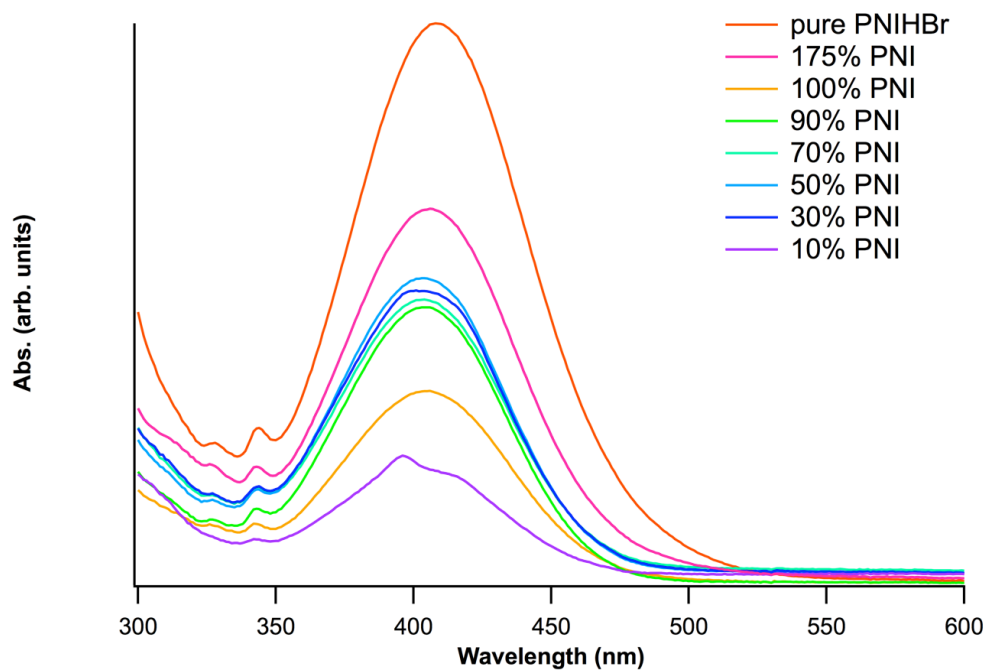


**Figure S4.7** The electronic absorption spectra (multi-color, see legend) of supernatants after centrifugation of various perovskite-PNI hybrid species.

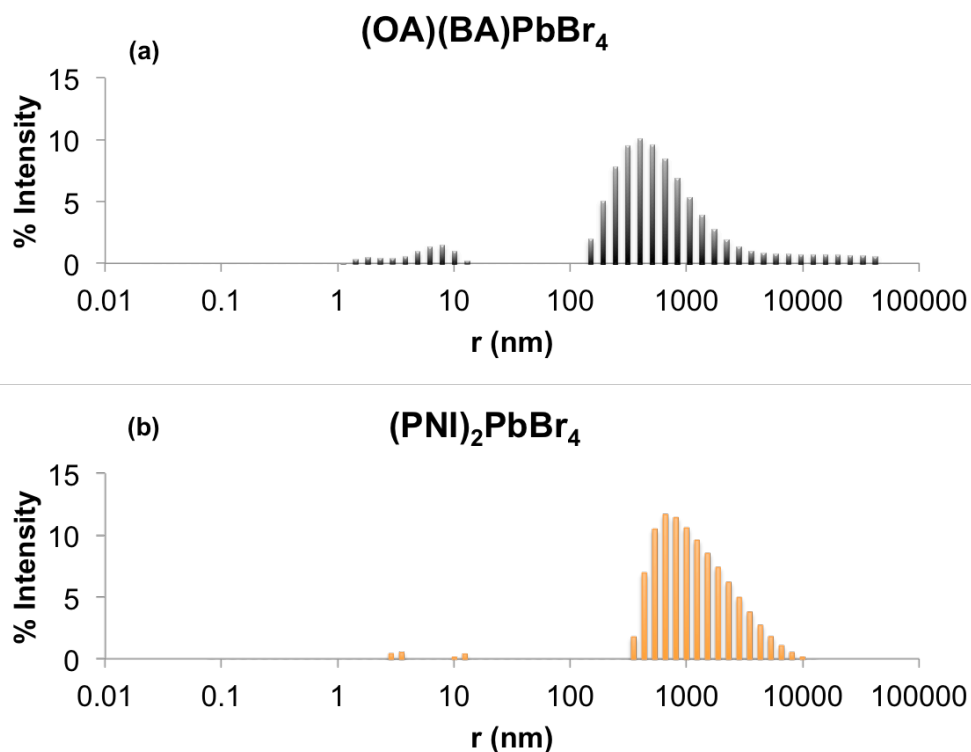


**Figure S4.8** Hydrodynamic radii distributions for (OA)(BA)PbBr<sub>4</sub> nanoplatelets (a) and (PNI)<sub>2</sub>PbBr<sub>4</sub> nanoplatelets (b) in toluene as determined by DLS.

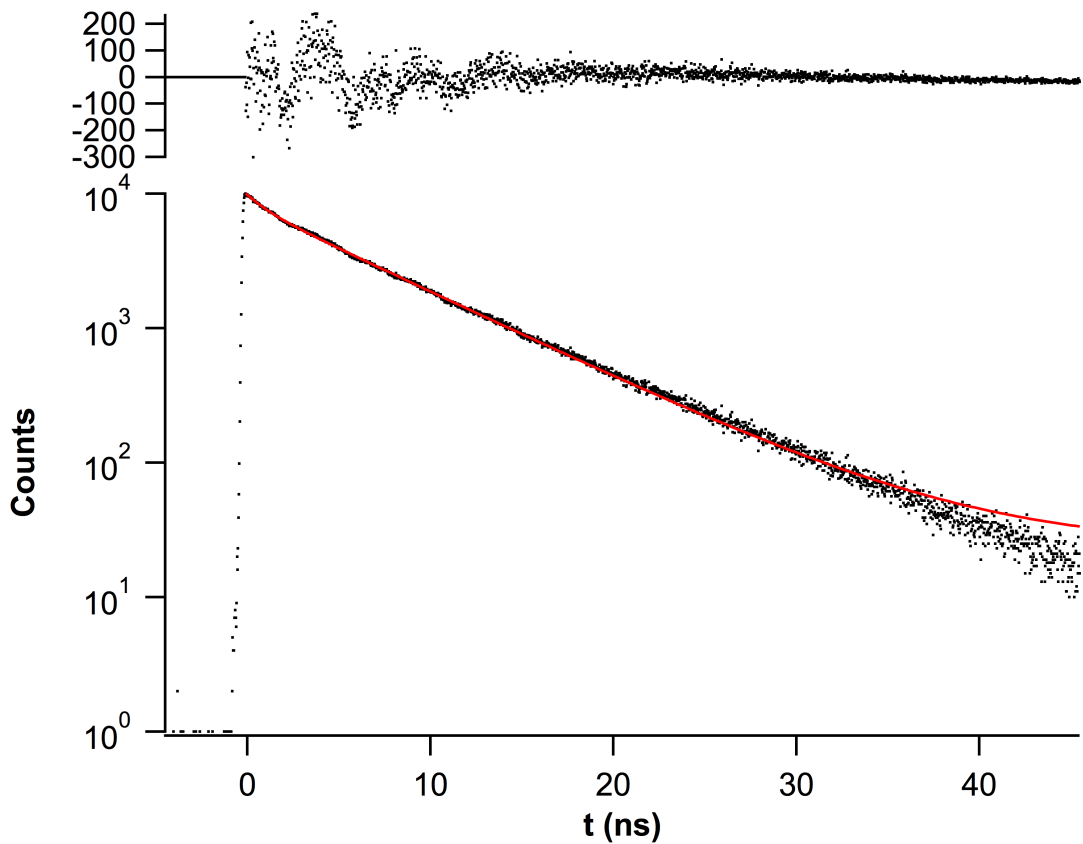


**Figure S4.9** TCSPC fluorescence intensity decay from PNI surfactants associated with  $(\text{PNI})_2\text{PbBr}_4$  nanoplatelets in toluene. The red trace is a monoexponential decay curve fit to the TCSPC data with the residuals displayed above. Sample was excited by a 405 nm diode laser (56.5 ps fwhm) set to a 100 kHz repetition rate. A band-pass filter centered at 500 nm with a 45 nm width was used to select the emission.